Investigation of Piezoelectric Flaps for Load Alleviation Using CFD

Heinz, Joachim Christian

Publication date:
2009

Document Version
Publisher's PDF, also known as Version of record

Investigation of Piezoelectric Flaps for Load Alleviation Using CFD

Risø-R-Report

Joachim Christian Heinz
Risø-R-1702(EN)
2009

Risø DTU
National Laboratory for Sustainable Energy

Author: Joachim Christian Heinz
Title: Investigation of Piezoelectric Flaps for Load Alleviation Using CFD
Division: Wind Energy Division

Risø-R-1702(EN)
2009

Published o www.risoe.dtu.dk in March 2010

Abstract (max. 2000 char.):

Cost efficient wind power generation demands for large wind turbines with a long lifetime. These demands place high interests on sophisticated load control techniques such as deformable trailing edge flaps.
In this work a previously tested prototype airfoil was investigated by using the 2D incompressible RANS solver EllipSys2D. The prototype was built with a Risø-B1-18 airfoil where piezoelectric actuators THUNDER TH-6R were attached at the trailing edge to realize a movable flap. The results of the simulation were compared to measurements of the previous wind tunnel test and comprehensive steady state computations were conducted to gain information about the general airfoil properties.
The model was subsequently used to investigate aero-servo-elastic effects on the 2D airfoil section exposed to a fluctuating inflow. It is explained how a fluctuating inflow was simulated with EllipSys2D and how the CFD solver was coupled with a 3 DOF structural model and with two different control algorithms. Control 1 used the measured AOA in front of the LE as input, Control 2 used the pressure difference between suction and pressure side as input. The model showed a substantial load reduction potential for the present prototype airfoil. For a wind step from 10 m/s to 10.5 m/s the standard deviation of the structural deflection normal to the rotor plane could be reduced with up to 98 % (Control 1) and 96 % (Control 2). A 4 s turbulent inflow with TI=2.2 % could be reduced with up to 81 % (Control 1) and 82 % (Control 2). For a 12 s inflow with TI=2.4 % the standard deviation could be reduced with up to 68 % (Control 1) and 67 % (Control 2). The influence of possible time lags inside the control loop on the reduction potential of the prototype was also investigated. For a 12 s inflow with a tripled turbulence intensity of TI=7.7 % the prototype airfoil could still reach a reduction of up to 54 %. For an extended flap range of -6 to +6 degrees the reduction could be returned to 66 %.

ISSN 0106-2840
ISBN 978-87-550-3767-0

Contract no.:

Group's own reg. no.:
(Føniks PSP-element)

Sponsorship:

Cover :

Pages: 75
Tables:
References:

Information Service Department
Risø National Laboratory for Sustainable Energy
Technical University of Denmark
P.O.Box 49
DK-4000 Roskilde
Denmark
Telephone +45 46774005
bibl@risoe.dtu.dk
Fax +45 46774013
www.risoe.dtu.dk

Investigation of Piezoelectric Flaps for Load Alleviation Using CFD

Joachim Christian Heinz
M.Sc. Thesis

Risø National Laboratory, Roskilde, Denmark
2009

Contents

Nomenclature

Roman symbols

c_x,c_x,c_θ	Damping coefficients of the structural model [Ns/m]
c	Total chord length of the airfoil (including attached flap) [m]
d_1	Distance from pitot tube measurement to LE [m]
d_2	Distance from LE to pressure taps [m]
$\mathrm{d}C_l/\mathrm{d}\beta$	efficiency of the flap [1/rad]
k	Reduced frequency ($k = \omega c/(2U)$) [-]
k_x,k_x,k_θ	spring stiffnesses of the structural model [N/m]
l	Distance from LE to CG [m]
m	Mass of airfoil section [kg]
u_{inlet}	x-component of inlet velocity in EllipSys2D (CFD coordinates) [-]
v_{inlet}	y-component of inlet velocity in EllipSys2D (CFD coordinates) [-]
r	Radial blade position of investigated airfoil section [m]
r_x	Translatoric motion in x of moving mesh in EllipSys2D (CFD coordinates) [-]
r_y	Translatoric motion in y of moving mesh in EllipSys2D (CFD coordinates) [-]
t	Time (used in structural model) [s]
t^*	Non-dim. time (used in aerodynamic model) [-]
t_{delay}	Time delay inside the control [s]
x_{struct}	Structural deflection in x (structural coordinates) [m]
x^*_{struct}	Non-dim. structural deflection in x (structural coordinates) [-]
y_{struct}	Structural deflection in y (structural coordinates) [m]
y^*_{struct}	Non-dim. structural deflection in y (structural coordinates) [-]
A_α	Gain parameter of Control 1 [-]
A_α	Gain parameter of Control 2 [ř/Pa]
C_n	Normal force coeff. (in x of structural coordinates) [-]
C_t	Tangential force coeff. (in y of structural coordinates) [-]
F_x	Tangential force in x (structural coordinates) [N]
F_y	Normal force in y (structural coordinates) [N]
F_θ	Moment around RC [Nm]
$F^*_{x,CFD}$	Non-dim. force in x (CFD coordinates) [-]
$F^*_{y,CFD}$	Non-dim. force in y (CFD coordinates) [-]
$F^*_{\theta,CFD}$	Non-dim. moment around RC [-]
I_{CG}	Moment of inertia around CG [kg m^2]
U_∞	Free-stream velocity [m/s]
U^*_∞	Non-dim. free-stream velocity [-]
V_a	Axial wind velocity [m/s]
V^*_a	Non-dim. axial wind velocity [-]
V_{rot}	Rotational velocity of blade at r [m]
V^*_{rot}	Non-dim. rotational velocity of blade at r [-]

Greek symbols

α	Angle of attack after structural motion is added
α_m	Mean angle of attack during pitching motion
α_{presc}	Angle of attack before structural motion is added
β	Flap deflection angle
β_{max}	Maximum deflection angle of the THUNDER TH-6R actuator
β_{min}	Minimum deflection angle of the THUNDER TH-6R actuator
η	Normal direction of grid coordinates
ζ	Rotational angle between coordinate system 4 and 5
θ_{geom}	Pitch angle of the blade
θ_{struct}	Structural deflection around RC
κ	Phase shift between prescribed pitching and flapping motion
φ	Rotational angle of moving mesh in EllipSys2D (rotation around RC)
ξ	Tangential direction of grid coordinates
ϕ	Flow angle after structural motion is added
ϕ_{presc}	Flow angle before structural motion is added
ξ	Rotational angle between coordinate system 4 and 5

Abbreviations

2 D	2-Dimensional
AOA	Angle of attack
CFD	Computational Fluid Dynamics
CG	Center of gravity of airfoil section
DOF	Degree of freedom
DTEG	Deformable trailing edge geometry
LE	Leading edge
RC	Rotational center of airfoil section and of moving mesh

1 Introduction

During normal operation, wind turbine blades are constantly subjected to fluctuating inflow conditions. This is due to the unsteady nature of the wind, the influence of the tower, wind shear effects and operation in a yawed position. The fluctuations in the inflow cause constantly changing loads on the blades which can in turn cause fatigue damage. Reducing the fatigue loads on the blades can lead to lighter blades and reduce the loads on other components such as bearings, drive train and tower. As a consequence the lifetime and the size of the wind turbines can be increased which makes wind energy potentially cheaper and even more competitive to other energy sources.

Recent work has shown that for Mega-Watt size wind turbines individual pitching can alleviate load increments from yaw-errors, wind shear, gusts, and turbulence considerably [1]. Compared to a collective pitch, where all blades are pitched equally, it is shown that with individual pitching the fatigue loads at the hub can be reduced with 28%. However, pitching a blade means that large masses have to be moved and the actuation speed is limited. Especially the pitching mechanisms of large turbines are thus limited in its ability to react on quick changes in the incoming wind field.

In recent years research put a focus on more sophisticated load control techniques. A good overview of the presently investigated concepts is given in [2]. It is reported that the concept of a deformable trailing edge geometry (DTEG) represents an effective and suitable technique to alleviate the fluctuating loads on large wind turbines. A change of the trailing edge geometry by using a small flap or a tab can be accomplished much quicker than turning a whole blade during pitching and this increases the ability to react on quick changes of the encountered wind field. Additionally, DTEG devices can be actuated individually over the radial blade position and they can thus much better accommodate to the respective wind situations seen by the blade.
One concept to change the aerodynamic forces of a wind turbine blade with a DTEG is by using a Gurney flap like device, also called a microtab. Wind tunnel tests by Yen Nakafuji et al. [3] and CFD computations by Chow and van Dam [4] demonstrate a significant potential for load alleviation. Van Dam found that microtabs could increase the lift coefficient C_l in the linear range of the lift curve by 50% while the increase in drag was modest.
Previous work at Risø National Laboratory, Denmark, showed a high potential of load alleviation by using a deformable flap at the trailing edge. With a 2 D aero-servo-elastic model Buhl et al. [5] showed that the standard deviation of the normal force on a 2 D airfoil section, suspended with springs and dampers, could be reduced with up to 95% if the airfoil experiences a sudden wind step from 10 m/s to 12 m/s. When the airfoil was exposed to a turbulent wind field with 10% turbulence intensity the normal force could be reduced with up to 81%. Andersen [6] found in a 3 D aero-servo-elastic model of a Vestas V66 turbine, that for a wind field with 10% turbulence intensity the equivalent flapwise blade root moment can be reduced with 60%. In these computations effects like time lag, signal noise and maximum power consumption of the flap were included. The models in [5] and [6] both calculate the aerodynamic loads with a very time efficient unsteady potential flow solver developed by Gaunaa [7]. The solver uses thin airfoil theory where the airfoil is represented only by its camberline which can deflect in the trailing edge region in order to simulate the flapping motion.

As the theory showed huge potentials of load alleviation, it was decided to build a prototype airfoil and test its properties in a wind tunnel. A Risø-B1-18 airfoil was equipped with piezoelectric THUNDER TH-6R actuators in order to realize the deformable trailing edge. Piezoelectric elements deform gradually and thus maintain a smooth transition

between airfoil and flap which then corresponds to the suggested flap shape of Troldborg [8]. Tests with the airfoil for a step change in the flap angle from $\beta = -3\,^\circ$ to $\beta = 1.8\,^\circ$ showed that the obtainable ΔC_l lied between 0.1 and 0.13 in the linear part of the lift curve. Counteracting a sinusoidal pitching motion of $f = 1.63Hz$ and a varying AOA of $-3.6\,^\circ \leq \alpha \leq= 5.4\,^\circ$ with a phase shifted sinusoidal flapping motion of $-3\,^\circ \leq \beta \leq 1.8\,^\circ$ reduced the lift amplitude with approximately 80%.

These results place a high interest on using piezoelectric actuators as deformable trailing edge flaps. Therefore, the Risø-B1-18 airfoil equipped with THUNDER TH-6R actuators is investigated closer in this work.
A detailed model of the prototype airfoil shape is used as input for CFD calculations using the 2 D incompressible Reynolds averaged solver EllipSys2D. The possibility of EllipSys2D to simulate a prescribed pitching and flapping motion was used to compare the wind tunnel measurements with CFD calculations. These comparisons (see Chapter 5) give a better understanding of the prototype airfoil properties and the wind tunnel measurements. In Chapter 6 crucial steady state properties of the airfoil were calculated, which can then be used inside other simulation models, such as the dynamic stall model of Andersen [9].
Afterwards, a 3 DOF structural model and two suitable control algorithm are coupled with EllipSys2D. In Chapter 7 it is explained how existing routines of EllipSys2D are used in order to connect the structural model with the solver and how the simulation of a fluctuating inflow is realized. In Chapter 8 two different control strategies are presented and their respective control algorithms are implemented. Thus it is possible to investigate the aero-servo-elastic behaviour of the prototype airfoil (or of any other airfoil) using a Navier-Stokes flow solver, which takes viscous effects inside the flow field into account. The new aero-servo-elastic model is finally used in Chapter 9 to investigate the load reduction potential of the prototype airfoil exposed to a wind step and a fluctuating inflow.

2 EllipSys2D

The CFD flow solver used in this work is EllipSys2D developed by Michelsen [10], [11] and Sørensen [12]. This code solves the incompressible Reynolds averaged Navier-Stokes equations (RANS) using primitive variables (u, v and p) in curvilinear coordinates through a multiblock finite volume discretization approach. For incompressible flow an additional equation is needed for the pressure, and the standard practice is to derive a pressure equation (Poisson equation) by combining the continuity equation with the momentum equation. The momentum and pressure equations are then used in a predictor-corrector fashion (PISO algorithm) to determine the pressure and velocities of the new time step. The third order accurate QUICK scheme is used to project the convective velocities to the cell faces. Information about the PISO algorithm and the QUICK scheme can be found in [13].The overall EllipSys2D computations are proven to be second order accurate both in time and in space.
The $k - \omega\ SST$ (Shear Stress Transport) turbulence model by Menter [14] was used in this work. The model has been proven to give very promissing results for 2D airfoil flows [15]. The model is constructed as a blend of the original $k - \omega$ model by Wilcox in the near wall region and the $k - \epsilon$ model in the outer region. The two latter models are described in e.g. [13].
The simulations in this work are carried out under the assumption of a fully turbulent flow. Fully turbulent simulations are considered to provide reasonable results, especially if comparisons with measurements of wind tunnels with fairly high turbulence levels are carried out.
The grid generation is accomplished with HypGrid2D developed by Sørensen [16]. The

grid generator is using a hyperbolic mesh generation procedure, based on an equation of orthogonality and an equation for the cell face area. The generated grid can be seperated in several blocks of prescribed size in order to allow parallel (multiblock) computations.

2.1 Moving the Grid / Inlet Velocity

In order to simulate a motion of the airfoil, EllipSys2D provides a routine to move the grid. This routine accounts for the additional fluxes, which arise when the cell vertices are moved. As indicated in Figure 1, the translatoric motions r_x and r_y as well as a rotation φ are feasible.
In Chapter 5 the variable φ is used to describe a prescribed harmonic pitching motion of the airfoil in order to compare the results of wind tunnel measurements with CFD computations. In Chapter 7, where the CFD solver is coupled with a 3 DOF structural model, the variables r_x, r_y and φ will be used to describe arbitrary structural motions of the airfoil.
Besides changing the rotational angle φ of the moving mesh, the angle between airfoil and inflow can also be adjusted with the two inlet velocities u_{inlet} and v_{inlet} at the domain boundaries. How the several variables are finally used to describe a fluctuating inflow is explained in Section 7.2.2.

2.1.1 Comment on the force output:

It is important to note, that the calculated aerodynamic forces ${F_{x,CFD}}^*$ and ${F_{y,CFD}}^*$ are always given in the direction of the fixed CFD coordinate system. A rotation in φ does not change the direction of the forces.

2.1.2 Comment on the translatoric motion:

At each time step the translatoric *positions* of the moving mesh can be defined by the variables r_x and r_y while the respective translatoric *velocities* can not be given directly as input. Instead EllipSys derives the translatoric *velocities* and thus the additional fluxes through the cell vertices from the given positions by a first order difference approximation.

2.2 Morphing the grid

To accomplish the flap motion, two meshed airfoils are used as input - one with the maximum and one with the minimum flap angle. As indicated in Figure 2 the actual grid is then generated by a linear interpolation between the grid points of these two meshes. Grid points which are located far away from the movable flap have the same positions for both flap positions and thus do not feel the morphing procedure.
With this morphing technique the respective grid points move on a straight line from the maximum to the minimum flap configuration. This does not exactly correspond to the real motion, where the points move on an arc around the flap hinge point. However, for small changes in the flap angle β the introduced error is negligible. In this work only small changes in β are investigated and the linear interpolation technique is considered to be adequate.
In previous work such as [8] the flap was only moved with a prescribed harmonic motion. In Chapter 8 this will be changed and an implemented control algorithm will control the flap motion.

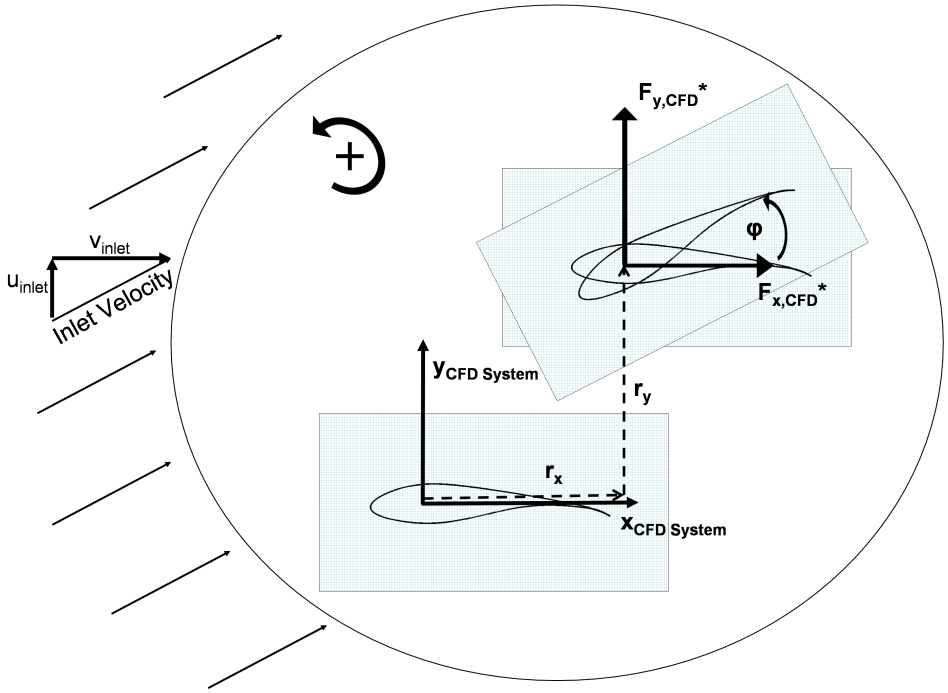

Figure 1. Translatoric motion and rotation of the movable mesh / Definition of inlet velocity at the domain boundary

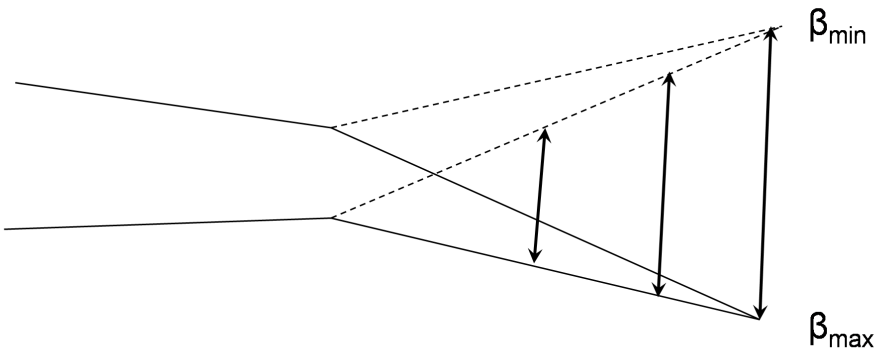

Figure 2. Linear interpolation between the 2 airfoils

3 Generation of Airfoil Shape

In this work the behaviour of the Risø B1-18 airfoil equipped with a THUNDER TH-6R piezoelectric actuator will be investigated. The baseline airfoil of the prototype, which was used in the VELUX wind tunnel tests, has a chord length of 0.6 m. At the rear part of its pressure side, the piezoelectric actuators (see Figure 3) were attached with an overlap of about 1 cm. Before the flaps were attached, some material had been milled away from the pressure side of the airfoil in order to ensure a smooth transition between the two

components. The resulting airfoil had a total chord length of about $c = 0.66$ m. A picture of the prototype is shown in Figure 4.

Figure 3. The Thunder TH-6R actuator from Face International Cooperation

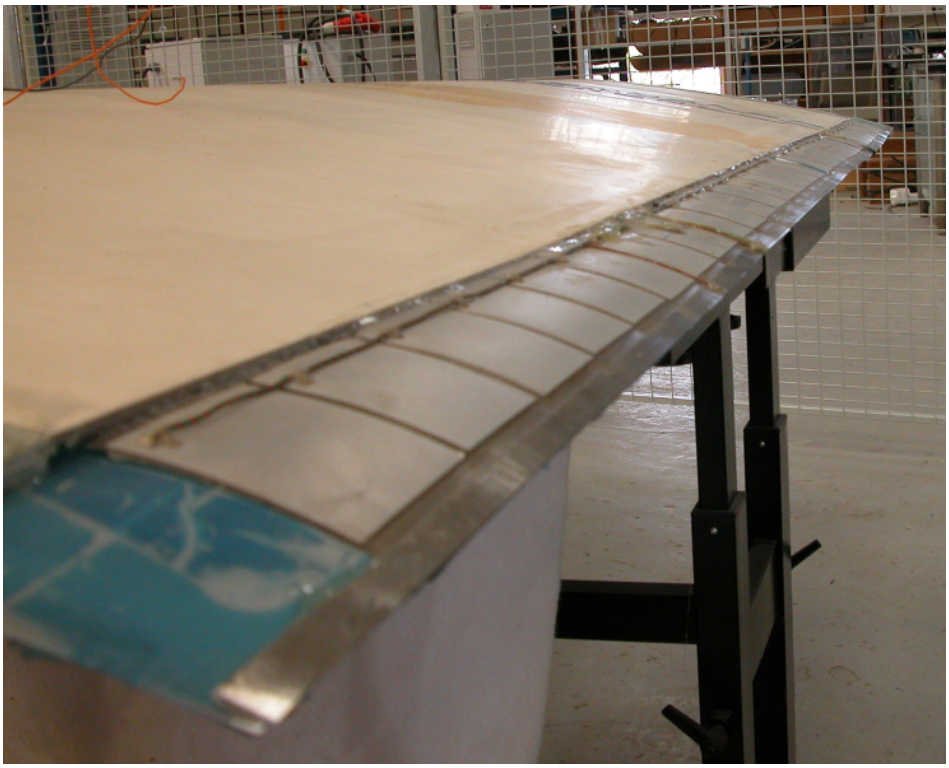

Figure 4. Picture of prototype

3.1 Method

The 2 D airfoil geometry is generated with Matlab. The intention is to generate a quite detailed airfoil geometry in order to conduct simulations very close to the real case. The coordinates for the prototype airfoil can not be obtained by simply measuring the airfoil, as no sufficiently exact measuring methods have been available. Therefore it is decided to use the exactly known geometries of the single components and put them virtually together. To attach the flap at the correct position and with the correct angle to the airfoil,

several coordinate systems are defined on the baseline airfoil (see Figure 5). In the following the position and orientation of the coordinate systems are listed. As the airfoil has a blunt trailing edge, it is necessary to distinguish between the "'central TE point"', which is defined as the intersection between camber line and airfoil contour, and the "lower TE point", which is located at the lower edge of the blunt trailing edge.

- System 1: origin at LE, x-axis tangential to chord line
- System 2: origin at central TE point, x-axis tangential to chord line
- System 3: origin at lower TE point, x-axis tangential to chord line
- System 4: origin at lower TE point, x-axis tangential to pressure side

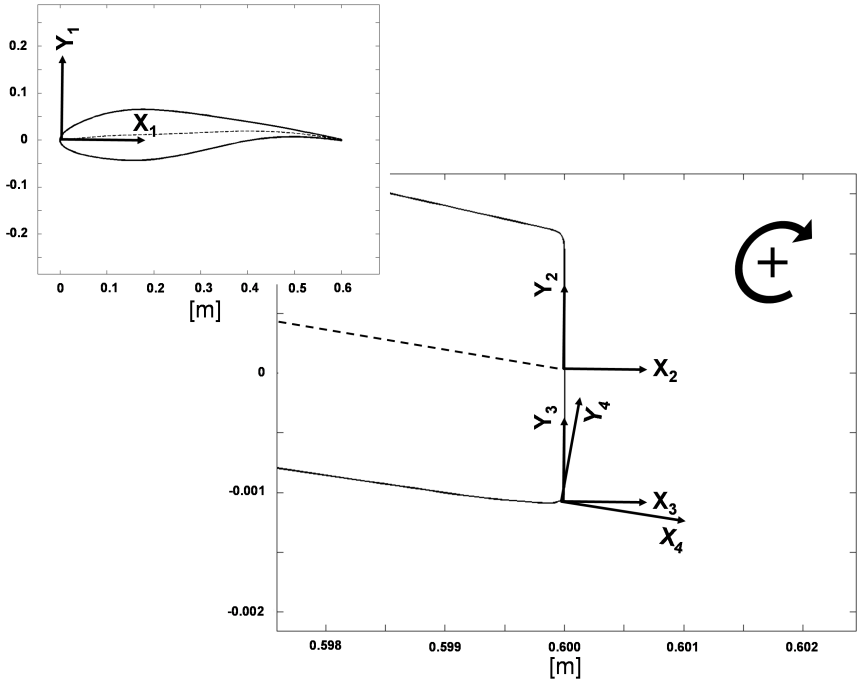

Figure 5. Coordinate Systems on the baseline airfoil

The geometry of the piezoelectric actuator is described in a separate coordinate system, i.e. coordinate system 5 (see Figure 6). The origin of coordinate system 5 is moved 1 cm inside of the actuator. This is due to the overlap between airfoil and actuator. Attaching the actuator to the baseline airfoil means that the origin of coordinate system 5 and the origin of coordinate system 4 coincide. To ensure a smooth transition between actuator and baseline airfoil, the x-axis of system 4 (which is tangentially aligned with the pressure side of the airfoil) has to be tangentially aligned with the actuator surface. This results in a certain rotation angle ζ between coordinate system 4 and 5.

Assuming that the camberline of the flap has the shape of a circular arc, two measures are enough to determine its geometry. It is the footprint size and the dome height shown in Figure 6. The deformation shape of the piezoelectric actuator depends on the applied voltage. To determine the deformation shape for a certain voltage, the respective footprint size and dome height of the actuator are derived out of the THUNDER TH-6R data sheet. Given the geometry of the flap camberline, simple geometrical formulas are used to calculate the rotation ζ between coordinate system 4 and 5 which ensures a smooth transition between actuator and baseline airfoil.

Finally the predefined flap contour is built around the flap camberline which is then attached to the contour of the baseline airfoil.

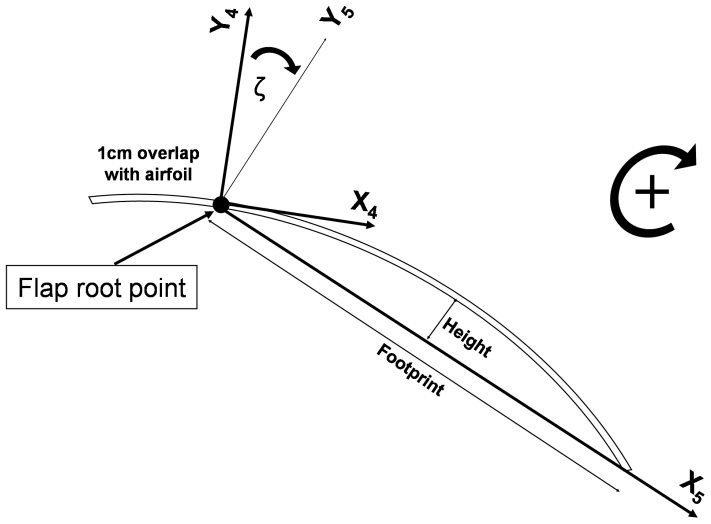

Figure 6. Coordinate System on the Piezoelectric Actuator

3.2 Definition of the Flap Deflection Angle β

Throughout this work, the flap deflection is described with the flap deflection angle β. It is thus important to note how this angle is defined. The reference line is the line between the flap root point and the very tip of the flap at an applied voltage of 0 V. In Figure 7 this reference line corresponds to the x-axis of coordinate system 5 for a rotation angle of ζ_{0V}, where ζ_{0V} is the angle for an applied voltage of 0 V. According to previous work the flap angle is defined positive for a clockwise rotation. Flapping downwards corresponds to an increase in β, flapping upwards corresponds to a decrease in β. In terms of the above introduced rotation angle ζ the flapping angle β can be calculated with

$$\beta = \zeta - \zeta_{0V} \tag{1}$$

It should be mentioned here that applying a positive voltage to the piezoelectric actuator will bend the flap upwards towards negative flapping angles. Applying a negative voltage will bend the actuator downwards towards positive flapping angles.

3.3 Maximum Deflection Angles of the Prototype

The generated airfoil for 0 V is shown in Figure 8. Figure 9 shows the rear part of the airfoil in a bigger scale. Additionally the deflection shapes for +750 V and -450 V are illustrated. These are the maximum voltages which could be applied to the tested prototype and thus, the respective deflection shapes represent the maximum flap angles β_{min} and β_{max}.
With equation (1) the maximum flap deflection angles of the generated airfoil can be calculated. The calculated angles $\beta_{min} = -5.3\,^\circ$ and $\beta_{max} = 2.2\,^\circ$ correspond exactly to the maximum deflection angles measured on the real prototype, when a voltage of +750 V and -450 V was applied. Thus, the above explained method of the airfoil generation results

in the correct flap angles β. As β is generated via ζ and thus via the voltage-dependent footprint and dome height of the piezoelectric actuator, it can also be concluded that the whole shape of the flap is captured accurately.

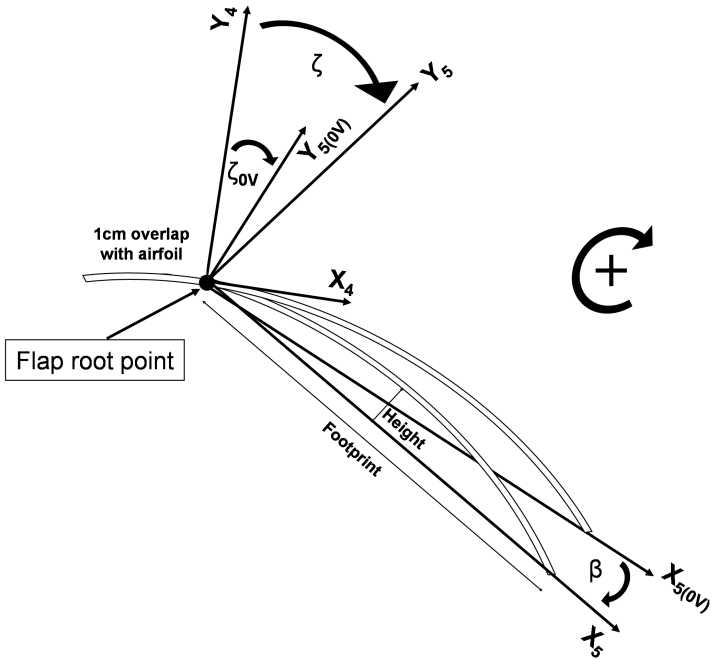

Figure 7. Definition of the flap deflection angle β

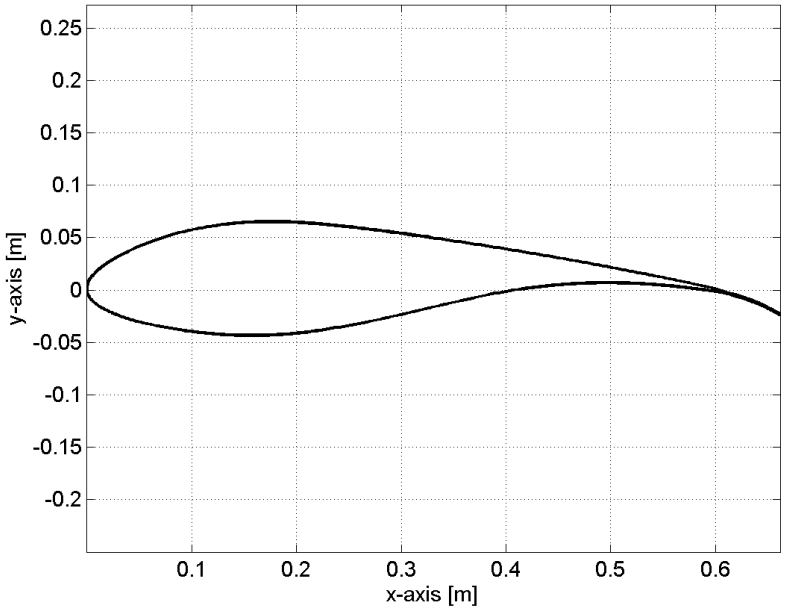

Figure 8. Airfoil with attached flap

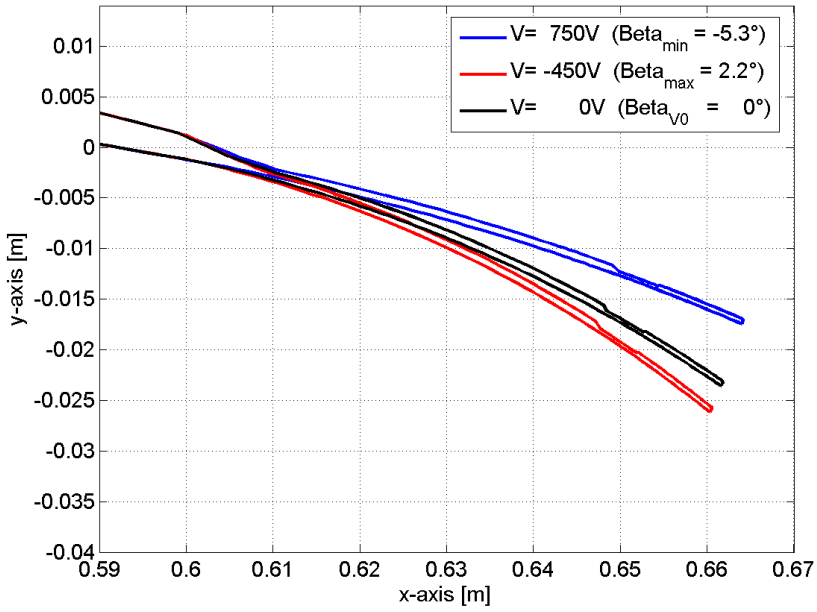

Figure 9. Maximum deflection shapes of the flap

4 Grid Study

4.1 Steady State Computations

The grid around the airfoil is generated with HypGrid2D [16]. Although the tip of the trailing edge flap is quite sharp an O-mesh was generated around the geometry. Close to the leading edge and close to other areas where high pressure gradients are expected, the cell size in tangential direction (ξ) is reduced in order to increase the accuracy of the computations. Especially at the thin trailing edge flap, the cell size has to be chosen quite small in order to catch the detailed geometry of the piezoelectric flap.
Before starting with thorough computations, it is crucial to check if the generated grid is capable of resolving the flow sufficiently and thus a grid independence study is carried out. In the work of Troldborg [8] some indication were given about how the grid should be generated. The domain height was set to $h_{Tot} = 20 \cdot c$ and the height of the cells situated closest to the airfoil surface was set to $h_{\eta=1,2} = 10^{-6} \cdot c$. This corresponds to a maximum y^+ value of around 0.2 which is considered to be sufficient to resolve the boundary layer properly. Troldborg thus used a grid of 256 cells into the tangential direction ξ and 128 cells into the normal direction η which met the needs of his airfoil geometry.
However, the model of the present prototype has a more complex flap geometry. In order to resolve these geometrical details, more cells are needed at the rear part of the airfoil and a new grid study has to be carried out.

The first grid study is done with steady state computations and include angles of attack between $-8\,^\circ$ and $20\,^\circ$. The test is conducted with two different airfoil configurations which represent the maximum flap deflections used in the upcoming chapters. For these maximum flapping angles of $\beta_{max} = 2.2\,^\circ$ and $\beta_{min} = -5.3\,^\circ$ the highest velocity gradients are expected. If the chosen grid can resolve these flows properly, it is believed that the grid is also adequate for all intermediate deflection shapes. Three different grids are

investigated. The first grid has a resolution of $256(\xi) \cdot 128(\eta)$ cells, for the other two grids the number of cells in the ξ direction is gradually increased. The number of cells into the normal direction η is kept unchanged.

- Grid 1: 256 (ξ) · 128 (η)
- Grid 2: 384 (ξ) · 128 (η)
- Grid 3: 512 (ξ) · 128 (η)

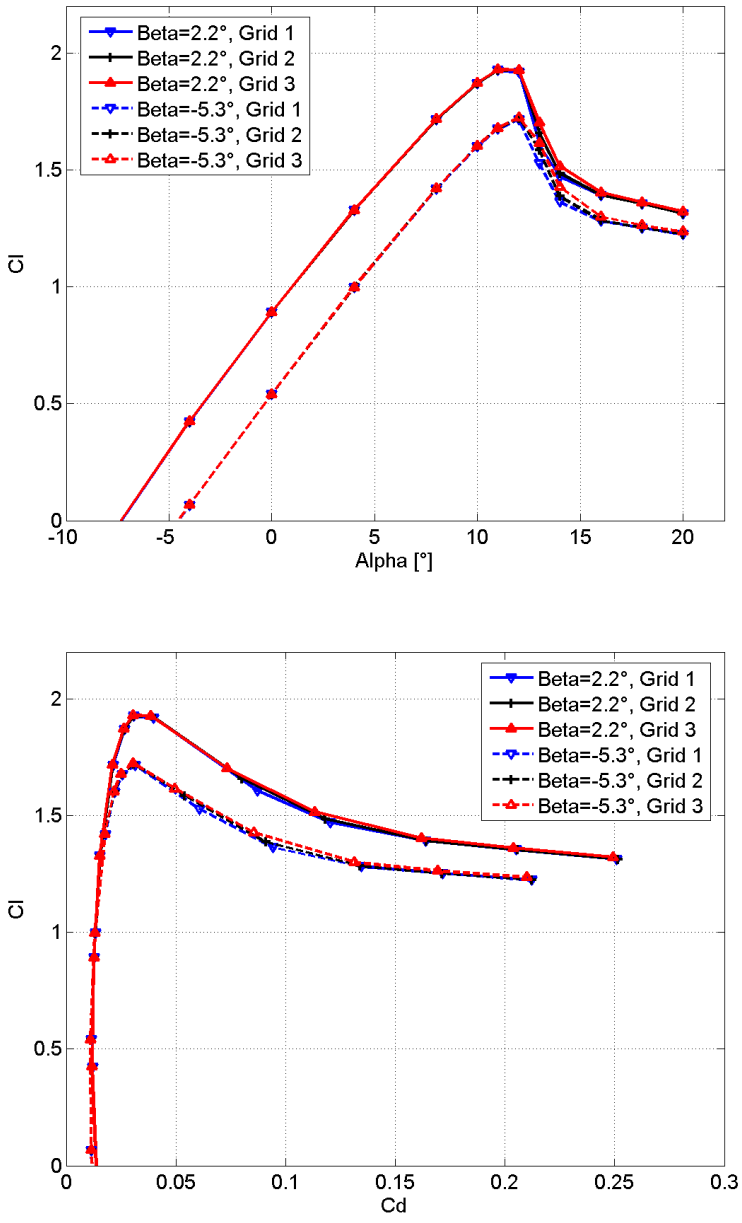

Figure 10. Polars for different grid sizes

In Figure 10 the results for the steady flow computations are shown. For both tested deflection shapes, the results for the three grids are quite similar. Especially in the attached flow region the computations do not reveal any significant deviations. Even in the stall

region the results correspond sufficiently, although the finer grid gives slightly higher lift coefficients. But these deviations are negligible, considering the fact that the computations in the stall region already include some uncertainties. Thus it is not necessary to use grid 2 or grid 3, which require much more computational time.

4.2 Unsteady Computations

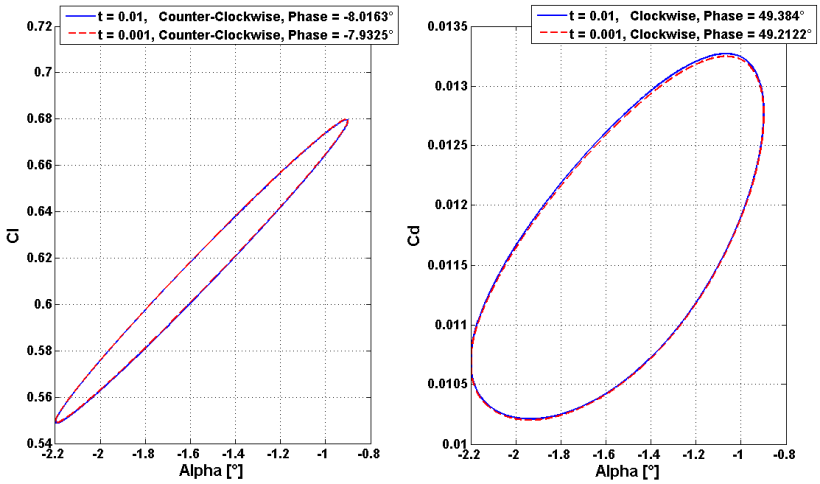

Figure 11. Time step investigation for pitch motion around $\alpha_m = -1.55\,°$, Reduced pitching frequency k=0.084 (1.62Hz), Constant flap angle $\beta = 0\,°$

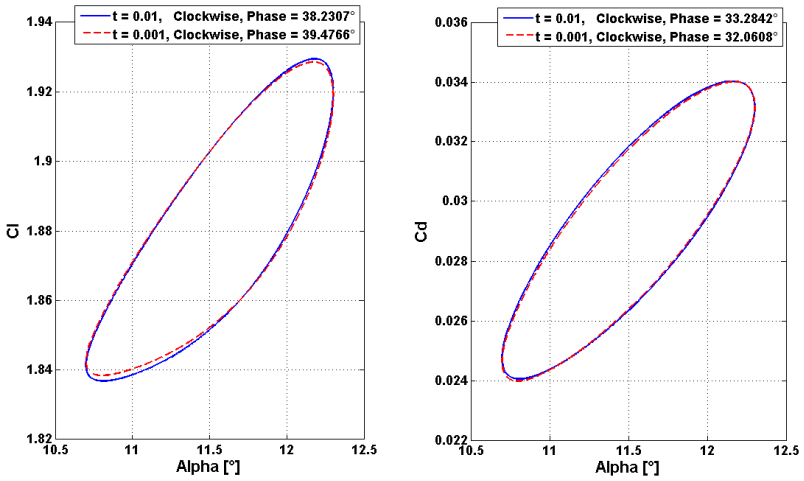

Figure 12. Time step investigation for pitch motion around $\alpha_m = 11.5\,°$, Reduced pitching frequency k=0.084 (1.62Hz), Constant flap angle $\beta = 0\,°$

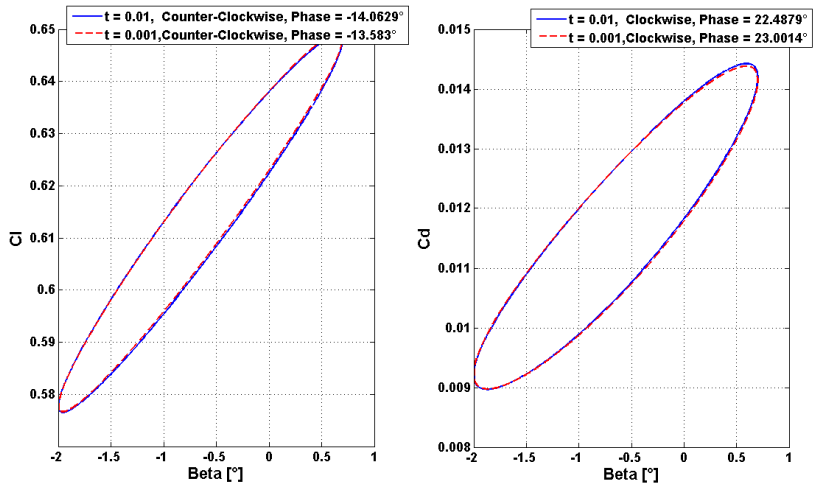

Figure 13. Time step investigation for flap motion of $-2\,° \leq \beta \leq 0.7\,°$, Reduced flapping frequency k=0.518 (10Hz), Constant AOA at $\alpha = -1.3\,°$

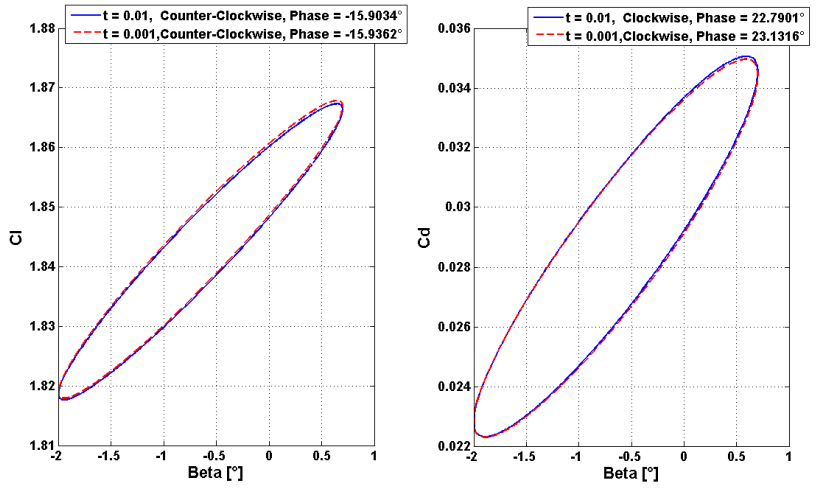

Figure 14. Time step investigation for flap motion of $-2\,° \leq \beta \leq 0.7\,°$, Reduced flapping frequency k=0.518 (10Hz), Constant AOA at $\alpha = 11.1\,°$

In [8] the unsteady simulations of a prescribed pitching and flapping motion were carried out with a non-dimensionalized time step of $\Delta t^* = 0.01$. A suitable time step which allows to resolve the flow around the airfoil appropriately is depending on the relation between fluid velocity and chosen cell size, which is commonly represented by the CFL number. To investigate if the time step of $\Delta t^* = 0.01$ is suitable for the present grid and the computations of the present work, the calculations with the most extreme angles of attack and the highest flapping frequencies are carried out with both a time step size of $\Delta t^* = 0.01$ and a time step size of $\Delta t^* = 0.001$. The results are shown in Figure 11 to Figure 14. It can be easily seen, that a smaller time step does not change the results significantly and thus a time step of $\Delta t^* = 0.01$ is considered to be sufficient for the computations.

5 Simulations and Measurements

In this chapter the results of the VELUX wind tunnel test [17] are compared with CFD calculations.
In Section 5.1 flow measurements with a fixed pitch and flap angle are compared with simulations. These comparisons will be used to confirm the correct generation of the airfoil geometry and its deflection shapes. In Sections 5.2 to 5.4 the simulations should then give a better understanding of the results of the dynamic wind tunnel measurements during an oscillating pitch and flap movement.

Detailed information about the wind tunnel test and its results can be found in [17]. The airfoil prototype had a span of 1900 mm and was tested at a Reynolds number of $Re = 1.66 \cdot 10^6$, which corresponds to an inflow velocity of $U_\infty = 40$ m/s. The airfoil was equipped with 64 pressure tabs in order to determine the lift forces and the pressure drag. For low AOA the total drag coefficient c_d, i.e. the sum of skin friction drag and pressure drag, was determined via a wake rake behind the airfoil which is detecting the pressure drop behind the airfoil. For high AOA with separated flow areas over the airfoil the wake rake measurements could not be used anymore and c_d was only determined via the pressure tabs.
Several corrections to the measured raw data had to be carried out. In [18] it is mentioned that the main correction for an open wind tunnel has to be done due to the effect of streamline curvature. The effect of downwash was considered in the corrections as well, although end plates were attached on both sides of the profile in order to establish a 2D flow and thus minimize this effect. Both effects have an influence on the AOA originally adjusted in the wind tunnel. The comparative CFD calculations of the following sections use the corrected AOA as input.
During the wind tunnel test, the deformations of the flaps were monitored with four strain gauges. The strains on the upper and lower surface of the flaps were transformed into a corresponding flapping angle β (see Chapter 3 for the definition of β). It was intented to track the current deflection shape of the flaps and to detect possible changes in the deflection shape due to the aerodynamic loading.
As mentioned in Chapter 3, the maximum deflections of the prototype are reached for $\beta_{min} = 2.2\,^\circ$ and $\beta_{max} = -5.3\,^\circ$. This is true for the static case. However, these maximum deflection angles could not be reached while the flaps were actuated with a certain frequency which was due to the limited power of the connected amplifier. The higher the flapping frequency was chosen, the lower was the range of β.

5.1 Fixed AOA / Fixed flap angle

The first comparison is done for the steady case, with a fixed pitch and flap angle. For a constant flap deflection angle of $\beta = 0\,^\circ$ (0 V applied on the piezoelectric flaps) several runs with different pitch angles are conducted. The resulting polars are shown in Figure 15. The airfoil used first is the one generated in Chapter 3 and is denoted as the airfoil with an *exactly mounted flap*. It can be seen that the calculations with the *exactly mounted flap* give higher lift coefficients than measured. In the linear region the curve is shifted to higher lift coefficients, with a ΔC_l of about 0.25. The constant curve shift indicates that the airfoil tested in the wind tunnel is less cambered than the generated airfoil of the simulation which means that the very tip of the prototype flap has to be higher up than assumed in the model. The reason for this could be that during the wind tunnel test the piezoelectric flap is bended upwards due to aerodynamic forces. But the strain gauge measurements do not indicate such a deformation, the measured flap angle remains at $\beta = 0\,^\circ$.

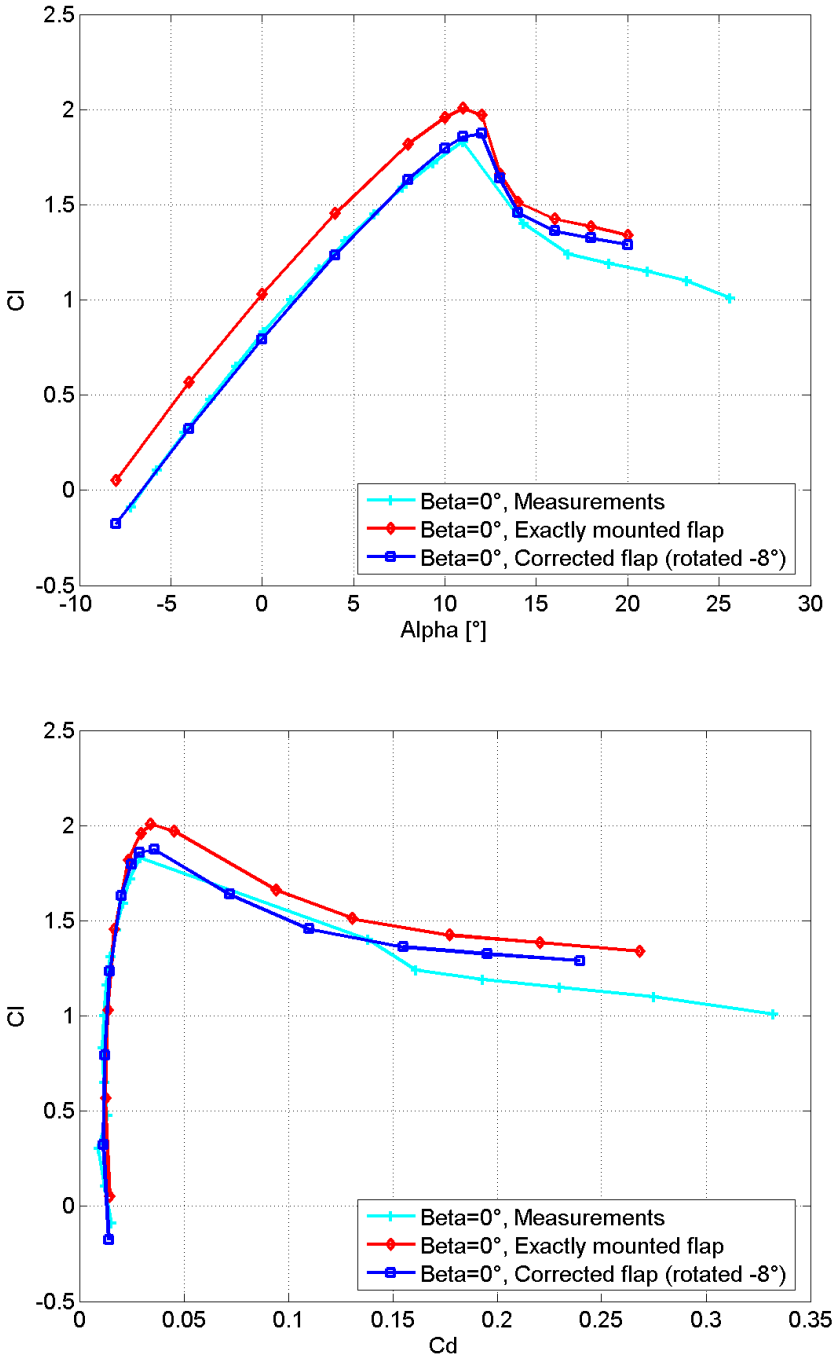

Figure 15. Polars for $\beta = 0\,^\circ$

The following assumptions were done to fit the measured with the calculated lift data.

1. One part of the deviations in the flap position could be explained by the fact, that it is very difficult to mount the flap exactly tangential to the pressure side of the airfoil. The flap position could easily vary within $2\,^\circ$ to $3\,^\circ$ and thus influence the measurements of the wind tunnel tests. These little deviations in the 0 Volt flap position can hardly be identified by observing the prototype, but they are definitely within the realm of possibility (see Figure 4).

2. Although the strain gauge measurements do not indicate a deformation due to aerodynamic forces, it is assumed that the piezoelectric elements do deform in the wind tunnel. Touching the flaps of the prototype with the bare hand gives the impression that the actuators are quite easily deformable. But they do not deform in the middle of the piezoelectric elements where the strain gauges are attached. They deform at the root of the flap where no ceramic layer is present and the bending moments are highest. The fact that the flap deforms at the flap root point explains why the strain gauge measurements could not indicate the deformation, although it was existent.

Both assumed deformations can be taken into account by rotating the flap around its root point. Hence, the flap is gradually rotated upwards until the modeled lift curve is fitting the measured lift curve. It is intented to fit the two curves at $C_l = 0$, because there no wind tunnel corrections have to be applied to the measurements, which makes the measurements at $C_l = 0$ the most reliable. The two lift curves fit best after a rotation of $-8\,^\circ$. The shape of the rotated or *corrected flap* can be seen in Figure 16.
After the correction of the flap position the lift curves do agree very well (see Figure 15). Even for high angles of attack and towards stall, when the corrections to the measured data are vital, the curves are still very close to each other.

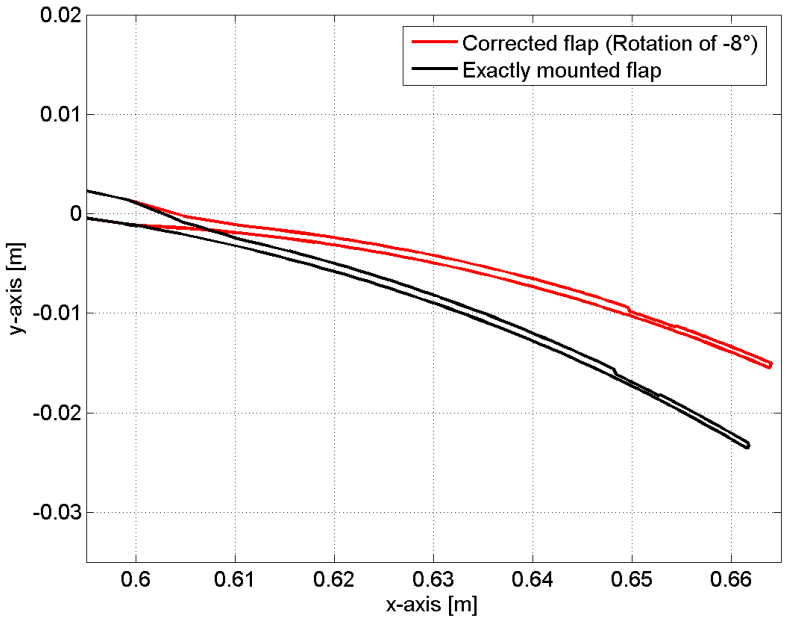

Figure 16. Flap position of the exact mounted flap and the corrected flap for $\beta = 0\,^\circ$

The corrected airfoil is now used for further steady flow comparisons in order to check if its flap deflection shapes for several flap angles correspond to those of the prototype. In Figure 17 the computed and the simulated polars for $\beta = -2\,^\circ$ and $\beta = 1\,^\circ$ are shown. Generally a good correspondence between measurements and simulation is found. Especially in the attached flow region the computed lift curve for $\beta = 1\,^\circ$ lies nearly exactly over the measured one. The calculated lift curve for $\beta = -2\,^\circ$ is also close to the measured curve. But due to its somewhat "bellied" shape in the normally linear region of the lift curve, there are some deviations between $\alpha = -4\,^\circ$ and $\alpha = 6\,^\circ$. In this region, the computed curve for $\beta = -2\,^\circ$ reaches lower lift coefficients and thus promises a higher lift reduction potential.

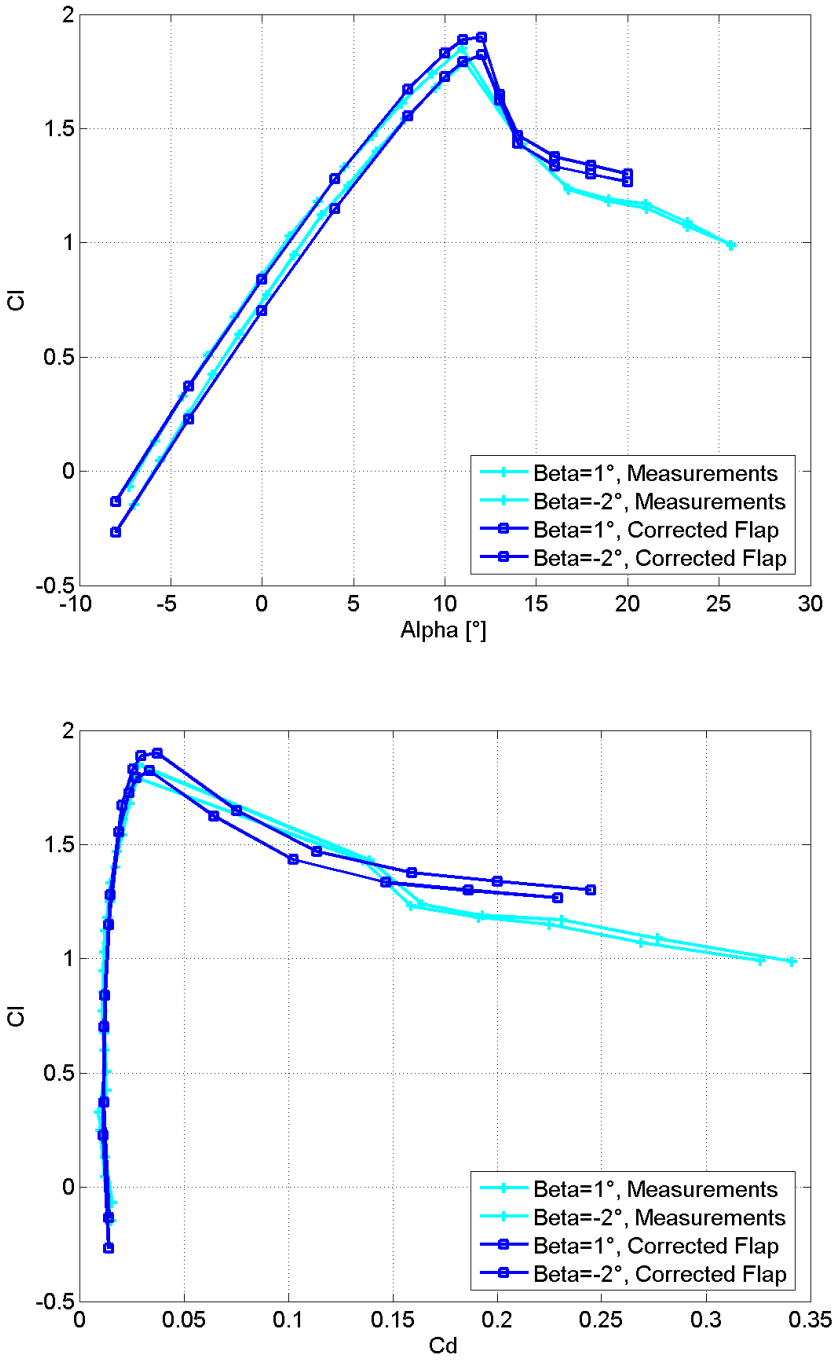

Figure 17. Polars for $\beta = 1\,^\circ$ and $\beta = -2\,^\circ$

The reason for these deviations could lie in inaccuracies during the wind tunnel measurements. Additionally the simulations are carried out by assuming a fully turbulent flow around the airfoil. This should be a good approximation because the turbulence intensity of the wind tunnel inflow was fairly high and the surface of the tested prototype with its pressure tabs and attached flap was considered to be fairly rough. Thus the flow around the tested airfoil was expected to be predominantly turbulent. However, the shape of the measured lift curve at $\beta = -2\,^\circ$ shows characteristics of an airfoil with laminar flow re-

gions. These characteristics are represented by an increased lift value at low AOA where large regions of laminar flow result in higher lift. With an increasing AOA the transition point moves gradually towards the LE and more parts of the flow become turbulent. The lift curve returns to the values of a fully turbulent flow.
However, as mentioned before, the flow around the tested airfoil was expected to be fairly turbulent which means that the deviations would then stem from something else. Another indication for that would be that the deviations between measurements and simulations are not that distinct for the higher flap deflection angles of $\beta = 0\,^\circ$ (Figure 15) and $\beta = 1\,^\circ$. In former comparisons between CFD simulations and measurements from the VELUX good correspondance could be found using fully turbulent modeling ([8]). It was thus not considered to use transition modeling in the simulations carried out in this work.

5.2 Harmonic motion of AOA / Fixed flap angle

The prototype airfoil is now tested under a harmonic pitching motion while the flapping angle remains constant at $\beta = 0\,^\circ$. The center of the pitching rotation was placed on the chord line, 0.24 m behind the leading edge. The pitching frequency was chosen to be 1.62 Hz which corresponds to a reduced frequency of $k = 0.084$. The comparisons to the simulations for four different mean angles of attack are shown in Figures 18 to 21. Additionally the results of potential flow computations using the dynamic stall model by Andersen [9] are shown. The results of the potential flow model are mainly used to confirm the loop direction of the computed lift and drag loops, they are not part of the general comparison between simulations and measurements. For the potential flow simulations of this section the computed polars of Figure 15 for the corrected flap at $\beta = 0\,^\circ$ are used as input.

The lift loops generally fit well in size and shape. The lift loops for $\alpha_m = -1.55\,^\circ$ and $\alpha_m = -4.3\,^\circ$ reach slightly lower values whereas the computed lift loops for $\alpha_m = 7.65\,^\circ$ and $\alpha_m = 11.5\,^\circ$ reach slightly higher values compared to the measurements. These deviations can be explained with the differences in the static lift curves, which are also shown in the graphs.
The lift loops of the CFD computations at $\alpha_m = -1.55\,^\circ$, $\alpha_m = 4.3\,^\circ$ and $\alpha_m = 7.65\,^\circ$ turn counter-clockwise. The exact phase shift is given in the respective graphs where a negative phase angle indicates that the lift lags behind the pitching motion and the lift loop turns counter-clockwise. For $\alpha_m = 11.5\,^\circ$ the direction of the computed lift loop becomes clockwise and more opened. This phenomena at high AOA is also discovered in [8] and can be explained by dynamic stall effects, which cause the flow to not reach its equilibrium state immediately. During pitching towards higher AOA, the separation point moves with a certain delay. Compared to the equilibrium state, the separation point is situated further downstream on the airfoil. This means that larger parts of the flow are still attached, which then results in a higher lift force. During pitching towards smaller AOA, the delayed movement of the separation point results in less parts of the flow being attached than in equilibrium. This results in a lower lift force. The measurements do not show this phenomena. Instead, all lift loops turn clockwise.

All computed drag loops rotate in a clockwise direction. Compared to the measured loops, the range between the maximum and minimum value of C_d is quite high and the loops describe a big open loop. However the mean values of the loops are similar.
The loops of the measured C_d values are mostly very narrow and skewed. The recorded lines have several intersections which makes it impossible to determine a distinct loop direction. For further investigations of the drag loops, the drag would have to be measured in a more accurate way.

As the loop directions of the lift loops as well as the shapes of the drag loops show

significant differences between CFD simulations and measurements, it was decided to use potential flow results for a final assessment of the results. As seen in the respective figures the potential flow calculations confirm the results of the CFD - computations. The lift loops for $\alpha_m = -1.55\,^\circ$ and $\alpha_m = -4.3\,^\circ$ turn counter-clockwise and the shape of the drag loops is as open as in the CFD computations. In future wind tunnel tests special efforts have to be undertaken to figure out if and why the loops show a different behaviour in the test stand.

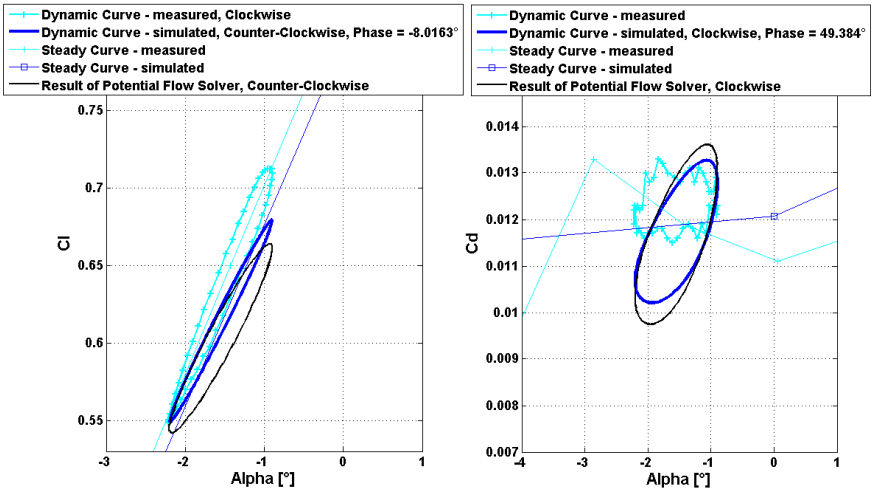

Figure 18. Pitching around $\alpha_m = -1.55\,^\circ$*, Pitching frequency* $f = 1.62Hz$ *(*$k = 0.084$*), Flap angle* $\beta = 0\,^\circ$

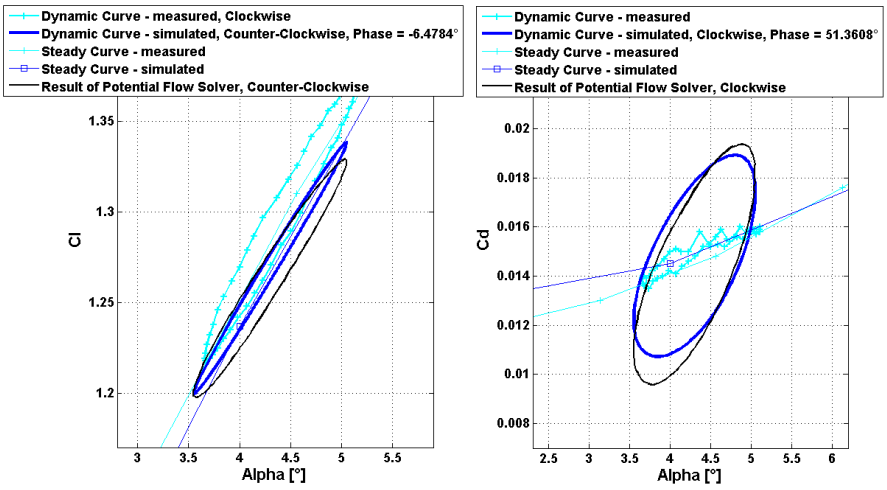

Figure 19. Pitching around $\alpha_m = 4.3\,^\circ$*, Pitching frequency* $f = 1.62Hz$ *(*$k = 0.084$*), Flap angle* $\beta = 0\,^\circ$

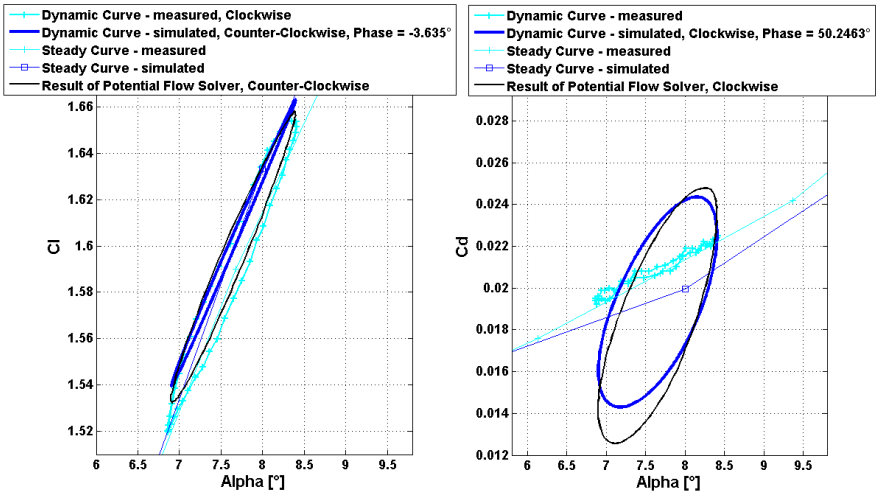

Figure 20. Pitching around $\alpha_m = 7.65\,^\circ$*, Pitching frequency* $f = 1.62Hz$ *(*$k = 0.084$*), Flap angle* $\beta = 0\,^\circ$

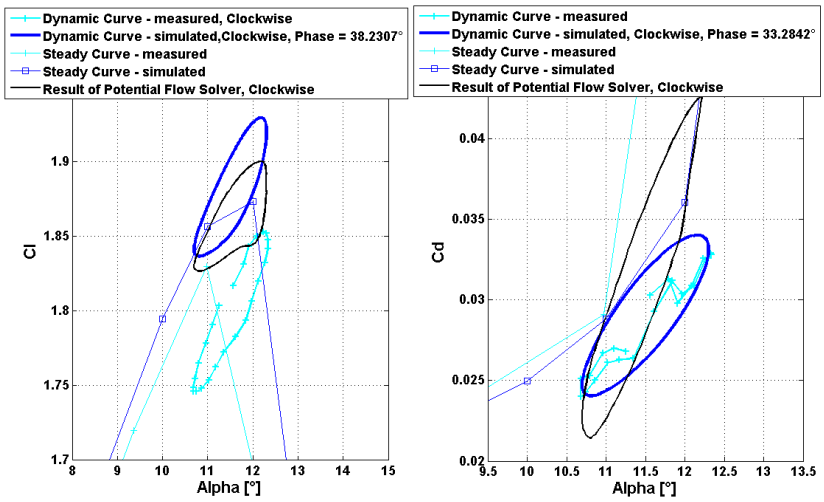

Figure 21. Pitching around $\alpha_m = 11.5\,^\circ$*, Pitching frequency* $f = 1.62Hz$ *(*$k = 0.084$*), Flap angle* $\beta = 0\,^\circ$

5.3 Fixed AOA / Harmonic motion of flap angle

In the following a harmonic flapping motion is investigated, while the AOA is held constant. The measurements and the simulations are compared for the two reduced oscillation frequencies $k = 0.081$ and $k = 0.518$. For the test setup this corresponds to the dimensionalized frequencies $f = 1.56$ Hz and $f = 10$ Hz. Due to the power limits of the amplifier the flapping angles could not reach the maximum deflection angles of the steady case. With the strain gauges on the piezoelectric flap the flap angles were monitored. The measured flap angles showed a clear dependency on the flapping frequency but no dependency on the AOA and the related change in aerodynamic loading. The following flap deflection angles were measured during the test cases.

- $f = 1.56\,\text{Hz}$ ($k = 0.081$): $\beta_{min} = -3\,^\circ$, $\beta_{max} = 2\,^\circ$
- $f = 10\,\text{Hz}$ ($k = 0.518$): $\beta_{min} = -2\,^\circ$, $\beta_{max} = 0.7\,^\circ$

In Figures 22 to 29 the results for the two frequencies at $\alpha = -1.3\,^\circ$, $\alpha = 4.6\,^\circ$, $\alpha = 7.8\,^\circ$ and $\alpha = 11.1\,^\circ$ are shown.
Again, the shapes of the lift loops fit very well. For the higher AOA of $\alpha = 7.8\,^\circ$ and $\alpha = 11.1\,^\circ$ the lift loops are located at a slightly higher lift force level. This was already seen in the results of the preceding section and can be explained with the differences in the steady curves.
For all tested AOA the simulated lift loops turn counter-clockwise and the loop shapes do not change significantly. This indicates that even for $\alpha = 11.1\,^\circ$ - and thus close to stall - no separation and dynamic stall effects occur. The wind tunnel measurements agree very well with these observations. All measured lift loops also turn counter-clockwise.

However, it can also be observed that the simulated lift loops reach higher extreme values than their measured equivalents and hence have a steeper slope. Comparing the results with the static values which are also shown in the respective figures demonstrate that the deviations in the extreme values were already present there. It is a consequence of the "bellied" lift curve for low flap deflection angles discussed in Section 5.1 and shown in Figure 17.
The slope $\mathrm{d}C_l/\mathrm{d}\beta$ is a measure of the lift change potential and thus the efficiency of the flap. Using the extreme values of the lift loops, the following slopes can be determined at the four observed AOA (Tables 1 and 2).

$\alpha =$	-1.3 $^\circ$	measured: $1.43\,\text{rad}^{-1}$	simulated: $2.35\,\text{rad}^{-1}$
$\alpha =$	4.6 $^\circ$	measured: $1.34\,\text{rad}^{-1}$	simulated: $2.18\,\text{rad}^{-1}$
$\alpha =$	7.8 $^\circ$	measured: $1.20\,\text{rad}^{-1}$	simulated: $2.00\,\text{rad}^{-1}$
$\alpha =$	11.1 $^\circ$	measured: $1.04\,\text{rad}^{-1}$	simulated: $1.72\,\text{rad}^{-1}$

Table 1. Flap efficiencies $\mathrm{d}C_l/\mathrm{d}\beta$ *for* $f = 1.56\,Hz$ *(*$k = 0.081$*)*

$\alpha =$	-1.3 $^\circ$	measured: $0.95\,\text{rad}^{-1}$	simulated: $1.59\,\text{rad}^{-1}$
$\alpha =$	4.6 $^\circ$	measured: $0.87\,\text{rad}^{-1}$	simulated: $1.49\,\text{rad}^{-1}$
$\alpha =$	7.8 $^\circ$	measured: $0.74\,\text{rad}^{-1}$	simulated: $1.27\,\text{rad}^{-1}$
$\alpha =$	11.1 $^\circ$	measured: $0.64\,\text{rad}^{-1}$	simulated: $1.06\,\text{rad}^{-1}$

Table 2. Flap efficiencies $\mathrm{d}C_l/\mathrm{d}\beta$ *for* $f = 10\,Hz$ *(*$k = 0.518$*)*

Both the measured and the simulated flap efficiencies $\mathrm{d}C_l/\mathrm{d}\beta$ decrease with an increasing AOA and an increasing flapping frequency. Generally, it can be seen that for an increase in flapping frequency from $f = 1.56\,\mathrm{Hz}$ to $f = 10\,\mathrm{Hz}$ the efficiency of the flap decreases with roughly $40\,\%$.
However, for both a flapping frequency of $f = 1.56\,\mathrm{Hz}$ and a flapping frequency of $f = 10\,\mathrm{Hz}$ the efficiency out of the simulations are about $60\,\%$ higher than the measurements. This is a quite pronounced devation between simulations and measurements.
The possible reasons for the deviations were already discussed in Section 5.1 and the observations of the present section demonstrate that the deviations should be investigated in future work.

The computed drag coefficient loops are again more opened and reach higher extreme values than their measured counterparts, whereas the mean values of the loops are similar. These observations correspond to those of the preceding section.

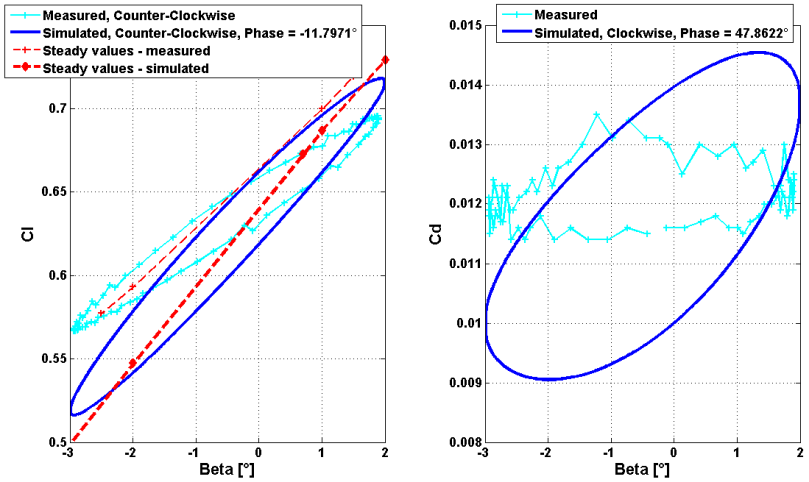

Figure 22. Flapping at $\alpha = -1.3\,^\circ$ with $f = 1.56\,Hz$ ($k = 0.081$)

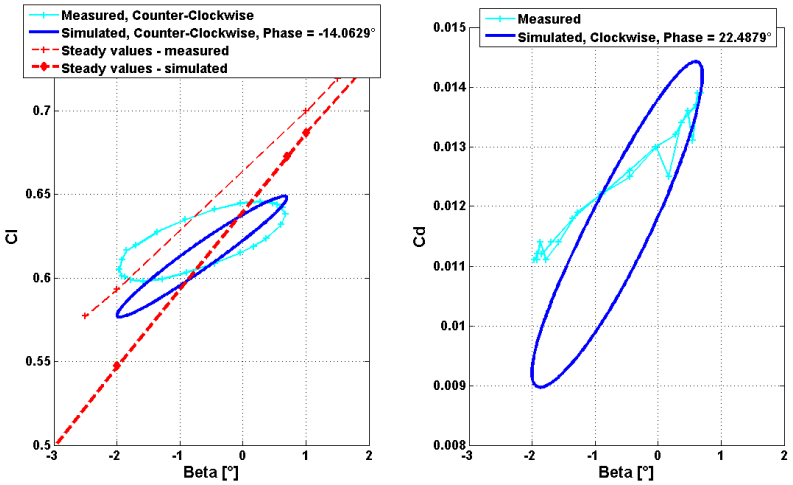

Figure 23. Flapping at $\alpha = -1.3\,^\circ$ with $f = 10\,Hz$ ($k = 0.518$)

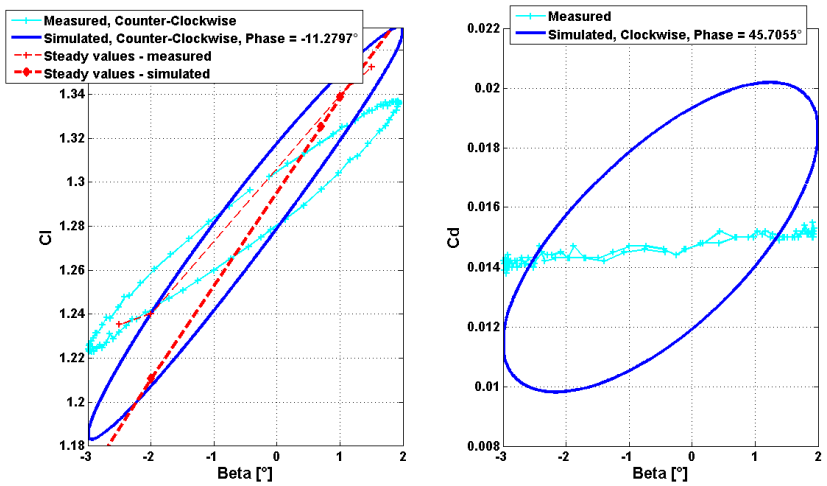

Figure 24. Flapping at $\alpha = 4.6\,^{\circ}$ *with* $f = 1.56\,Hz$ *(*$k = 0.081$*)*

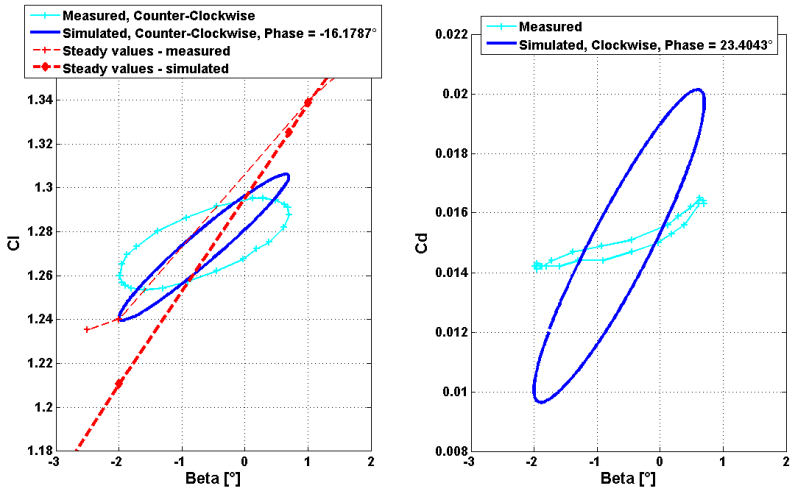

Figure 25. Flapping at $\alpha = 4.6\,^{\circ}$ *with* $f = 10\,Hz$ *(*$k = 0.518$*)*

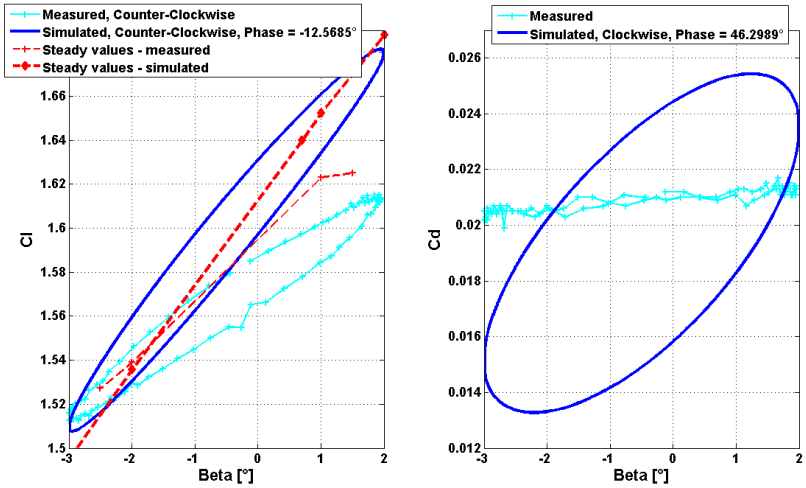

Figure 26. Flapping at $\alpha = 7.8\,^{\circ}$ *with* $f = 1.56\,Hz$ *(*$k = 0.081$*)*

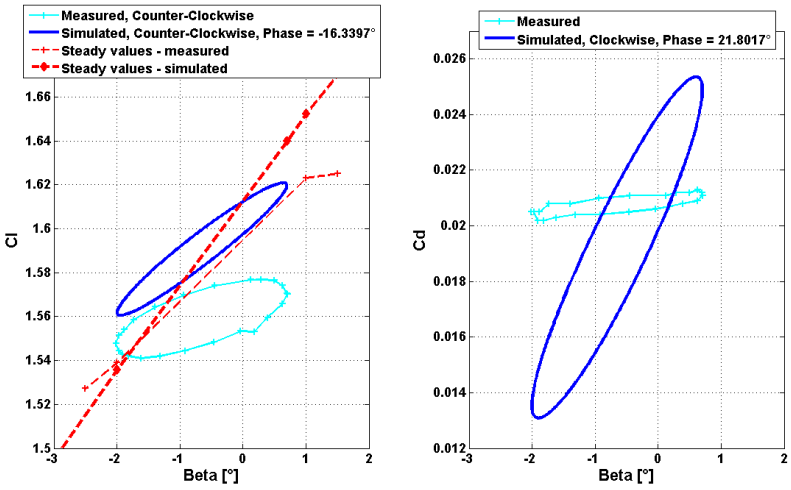

Figure 27. Flapping at $\alpha = 7.8\,^{\circ}$ *with* $f = 10\,Hz$ *(*$k = 0.518$*)*

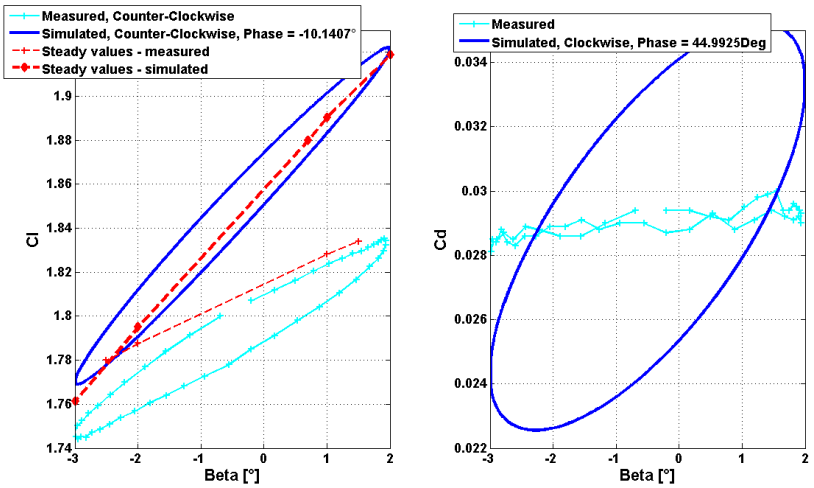

Figure 28. Flapping at $\alpha = 11.1\,^{\circ}$ *with* $f = 1.56\,Hz$ *(*$k = 0.081$*)*

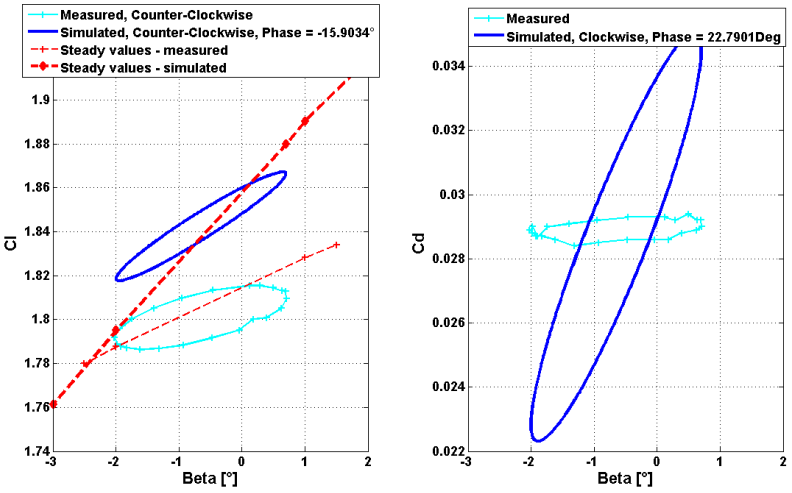

Figure 29. Flapping at $\alpha = 11.1\,^{\circ}$ *with* $f = 10\,Hz$ *(*$k = 0.518$*)*

5.4 Harmonic motion of AOA / Harmonic motion of flap angle

Finally the combination of pitching and flapping will be examined. Both the pitching and the flapping motion have a reduced frequency of $k = 0.084$ ($f = 1.62\,\text{Hz}$). In the wind tunnel tests the two oscillatory movements were shifted with a phase shift κ until the variations in the lift force were minimized. For a phase shift of $\kappa = 0\,^\circ$ the flap reaches its maximum upwrds position at the same time the airfoil reaches its maximum AOA. A positive phase shift means that the flap motion precedes the pitch motion.
Here the results for a mean angle of attack of $\alpha_m = -1.6\,^\circ$ are discussed. The flap deflection angle for the chosen frequency varies between $\beta = 2\,^\circ$ and $\beta = -3\,^\circ$.

The wind tunnel tests show the best results for a phase shift of $\kappa \approx 30\,^\circ$. In the simulations it was not intented to find the optimal phase shift, but several runs with different phase shifts have been accomplished in order to get a better picture of how the airfoil behaves for a combined pitching and flapping motion. The results are shown in Figure 30 and Figure 31. The measured data and a comparable potential flow simulation are included in Figure 30. The results of the measurements could not be confirmed in the simulation. While in the wind tunnel tests the biggest reductions in lift variation were achieved for a phase shift of around $\kappa = 30\,^\circ$, the simulations show best results for a phase angle of about $\kappa = 10\,^\circ$.

In the simulations, phase shifts between $\kappa = -50\,^\circ$ and $\kappa = 0\,^\circ$ result in clockwise lift loops, phase shifts between $\kappa = 10\,^\circ$ and $\kappa = 50\,^\circ$ result in counter-clockwise lift loops. However, the measured lift loop at $\kappa = 30\,^\circ$ turns clockwise.

The variation of the computed drag force can be minimized for about the same phase shift angle of $\kappa = 10\,^\circ$. For phase shift from $\kappa = -50\,^\circ$ to $\kappa = -20\,^\circ$ the drag loop direction is clockwise. From $\kappa = -10\,^\circ$ to $\kappa = 50\,^\circ$ the loops turn counter-clockwise. However, the measured drag loop at $\kappa = 30\,^\circ$ turns clockwise and thus differently than the computed loop.

In order to asses the deviations between measurements and CFD results, potential flow computations are used to get a clearer picture of the lift and drag force behaviour during a combined motion in AOA and β. As done in Section 5.2 the potential flow computations are not discussed in detail here, they are rather used to get an additional indication about the loop directions and loop shapes. The input for the dynamic stall model of Andersen [9] is derived from static lift and drag values of the wind tunnel measurements for several pitch and flap angles. In Figure 30 the result for a phase shift of $\kappa = 30\,^\circ$ is shown. The lift and the drag loop of the potential model turn into the same direction as the loops of the CFD computations. Additionally, the shapes of the lift and drag loop are also quite similar to the CFD computations, although the lift loop of the potential flow computations is slightly more narrow and the drag loop is slightly more broad. Hence, the potential flow computations confirm the results of the CFD simulations. The deviations between simulation and measurement might be consequences of the deviations already stated in the previous sections.

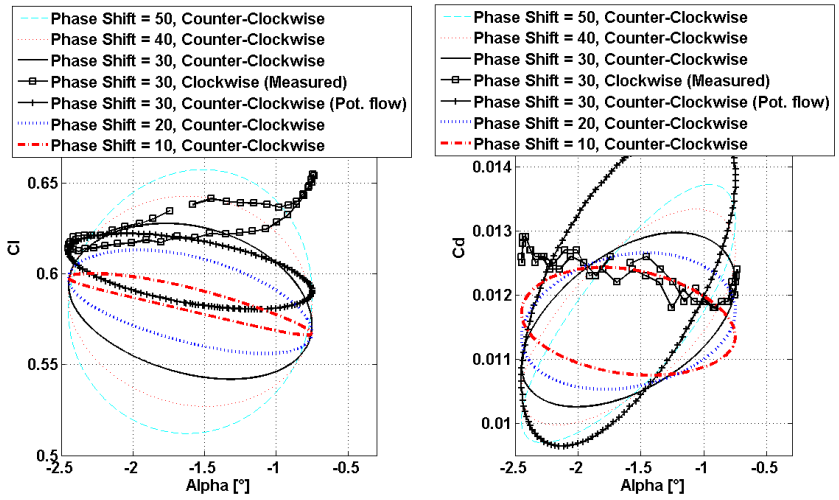

Figure 30. Pitching around $\alpha_m = -1.6\,°$ *Flapping from* $\beta = 2\,°$ *to* $\beta = -3\,°$, $f = 1.62Hz$ *(k = 0.084), Positive Phase Shifts* $(10\,° \leq \kappa \leq 50\,°)$

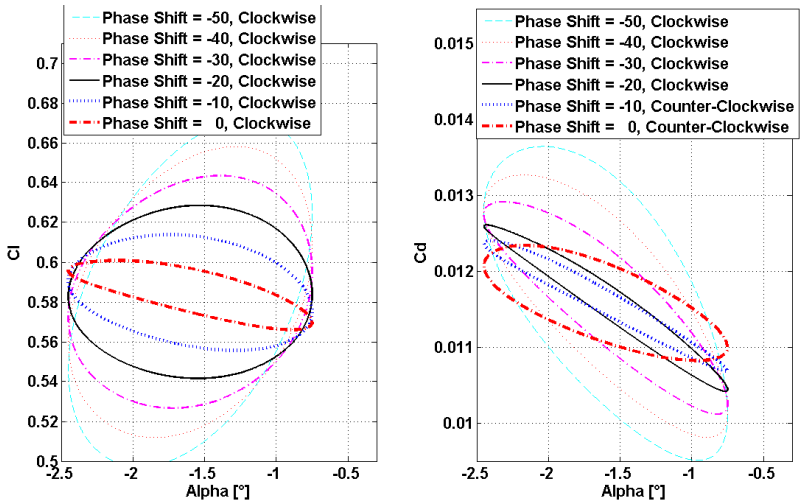

Figure 31. Pitching around $\alpha_m = -1.6\,°$ *Flapping from* $\beta = 2\,°$ *to* $\beta = -3\,°$, $f = 1.62Hz$ *(k = 0.084), Negative Phase Shifts* $(-50\,° \leq \kappa \leq 0\,°)$

6 Further Properties of the Airfoil

The new airfoil model is now used for further steady flow computations. This gives broad information about some key properties and the potentials of the prototype airfoil.

First of all the variations of the lift coefficients for several (fixed) AOA and (fixed) flap angles are calculated. This gives information about the general load reduction potential of the airfoil. The results are also valuable as input for the dynamic stall model of Andersen [9]. The calculations were carried out for both the corrected flap and the exactly mounted flap.

In Figure 32 the results for the airfoil with the corrected flap position are shown. The

values are related to the lift coefficient $C_{l(\beta=0)}$ of a non-deformed trailing edge flap (0 V applied). It can be seen that the movement of the flap evokes a nearly linear change in lift (holding the AOA constant). The slope $\mathrm{d}C_l/\mathrm{d}\beta$ measures the efficiency of the flap, it is the same quantity that was used in Table 1 and Table 2 for the wind tunnel test comparisons.
It can be seen in the Figure 32, that the efficiency of the flap in the attached flow region slightly decreases with increasing angles of attack. The maximum flap efficiency occurs for $\alpha = -4\,^\circ$ where a slope of $\mathrm{d}C_l/\mathrm{d}\beta = 2.75\,\mathrm{rad}^{-1}$ is reached. For a flap range of $\beta = 2.2\,^\circ$ to $\beta = -5.3\,^\circ$ a ΔC_l of 0.26 is calculated in the steady computations. From $\alpha = -4\,^\circ$ the efficiency decreases gradually until a $\mathrm{d}C_l/\mathrm{d}\beta = 1.8\,\mathrm{rad}^{-1}$ at an AOA of $\alpha = 11\,^\circ$.
When the flow separates the efficiency of the flap decreases very much. The slope at $\alpha = 14\,^\circ$ is only $\mathrm{d}C_l/\mathrm{d}\beta = 0.65\,\mathrm{rad}^{-1}$. When separation occurs at the aft of the airfoil the moving flap is not able to bend the flow in the same extend than before. The change in circulation and thus the change in lift decreases.
To complete the picture the polars for several flap positions are shown in Figure 34.

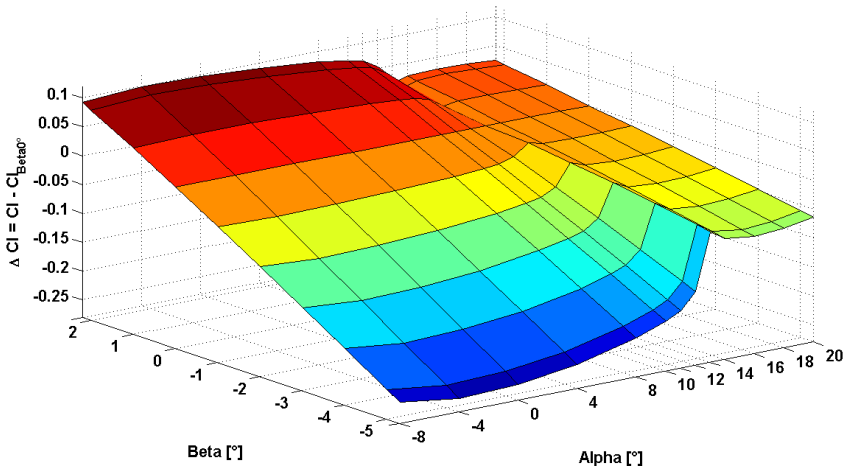

Figure 32. Potential of load reduction for the corrected flap

The same investigations are done for the exactly mounted flap which includes the assumption that the flap does not change its shape due to aerodynamic forces. In Figure 33 it can be seen that the potential for changing the lift is lower than for the corrected flap. The maximum slope at $\alpha = -4\,^\circ$ is $\mathrm{d}C_l/\mathrm{d}\beta = 2.2\,\mathrm{rad}^{-1}$. At $\alpha = 11\,^\circ$ it is $\mathrm{d}C_l/\mathrm{d}\beta = 1.53\,\mathrm{rad}^{-1}$ and at $\alpha = 14\,^\circ$ it is $\mathrm{d}C_l/\mathrm{d}\beta = 0.61\,\mathrm{rad}^{-1}$. The reason for this decrease in slope might be the fact that the exact mounted flap is pointing further down. As a consequence the vertical movement of the very tip of the TE is reduced. The camber of the airfoil changes less than for the corrected flap, which reduces the changes in lift. However, the absolute values of the lift coefficients are higher (see Figure 35).

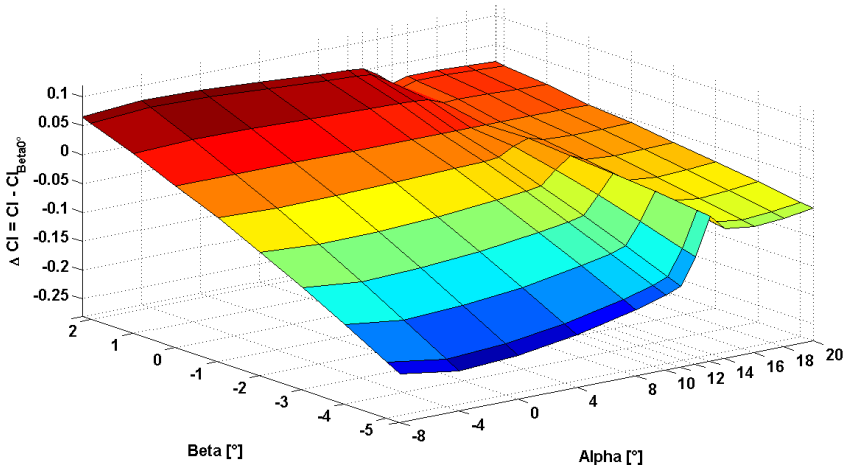

Figure 33. Potential of load reduction for the exactly mounted flap

For a better assessment of the two different airfoil shapes the lift to drag ratios are shown in Figure 36 and Figure 37. Below AOA of $\alpha = 5\,^\circ$ the gliding numbers of the exact mounted flap are generally higher for all flapping angles. For angles of attack above $\alpha = 5\,^\circ$ the gliding numbers for the exactly mounted flap are slightly lower, especially for positive flapping angles. In this case the exactly mounted flap is pointing strongly downwards and the flow cannot follow the curvature and thus separates. The increasing drag forces lead to worse lift to drag ratios. However, the exactly mounted flap with a smooth transition between baseline airfoil and flap seems to be the better choice in terms of lift to drag ratios.
It is also checked, if a flap with a smoothened surface could generally increase the gliding numbers. It was believed that the sharp contours at the upper surface of the prototype flap could evoke flow separations and thus an increase in the drag forces. Therefore the gliding numbers for a smoothened flap with a flap angle of $\beta = 0\,^\circ$ are included in Figure 36 and Figure 37. However, the curves of the non-smoothened and smoothened flap nearly coincide and no significant changes can be obtained by using a smoothened flap surface.

Finally the pressure distribution for four different angles of attack and three different flap angles are shown for the exactly mounted flap in Figure 38. The area enclosed by the pressure distribution line represents the produced lift of the airfoil. For low angles of attack such as $\alpha = 0\,^\circ$ and $\alpha = 4\,^\circ$ the flap can exert a big influence on the produced lift. It can be seen that the loading increases over the whole profile and not only at the flap itself. For higher angles of attack the flapping does not change the area in the same extend anymore which means that the flap is less effective at high AOA. This corresponds to the observations done at the beginning of this chapter.
The pressure distribution for $\alpha = 0\,^\circ$ reveals a steep adverse pressure gradient at the sharp contours of the trailing edge flap which might cause separation and high pressure drag values. As illustrated in the figure a smoothened flap shape reduces this pressure gradient and thus the risk of separation. The skin friction drag for the respective case (see Figure 39) shows that the skin friction for the non-smoothened flap reaches indeed negative values, which means that some areas of separated or reverse flow exist. In Figure 39 it can be also seen that the smoothened flap surface raises the skin friction back to positive values and thus prevents the airflow from separation. However, these small areas of detached flow do not influence the overall performance of the airfoil considerably (see the gliding numbers in Figure 37).

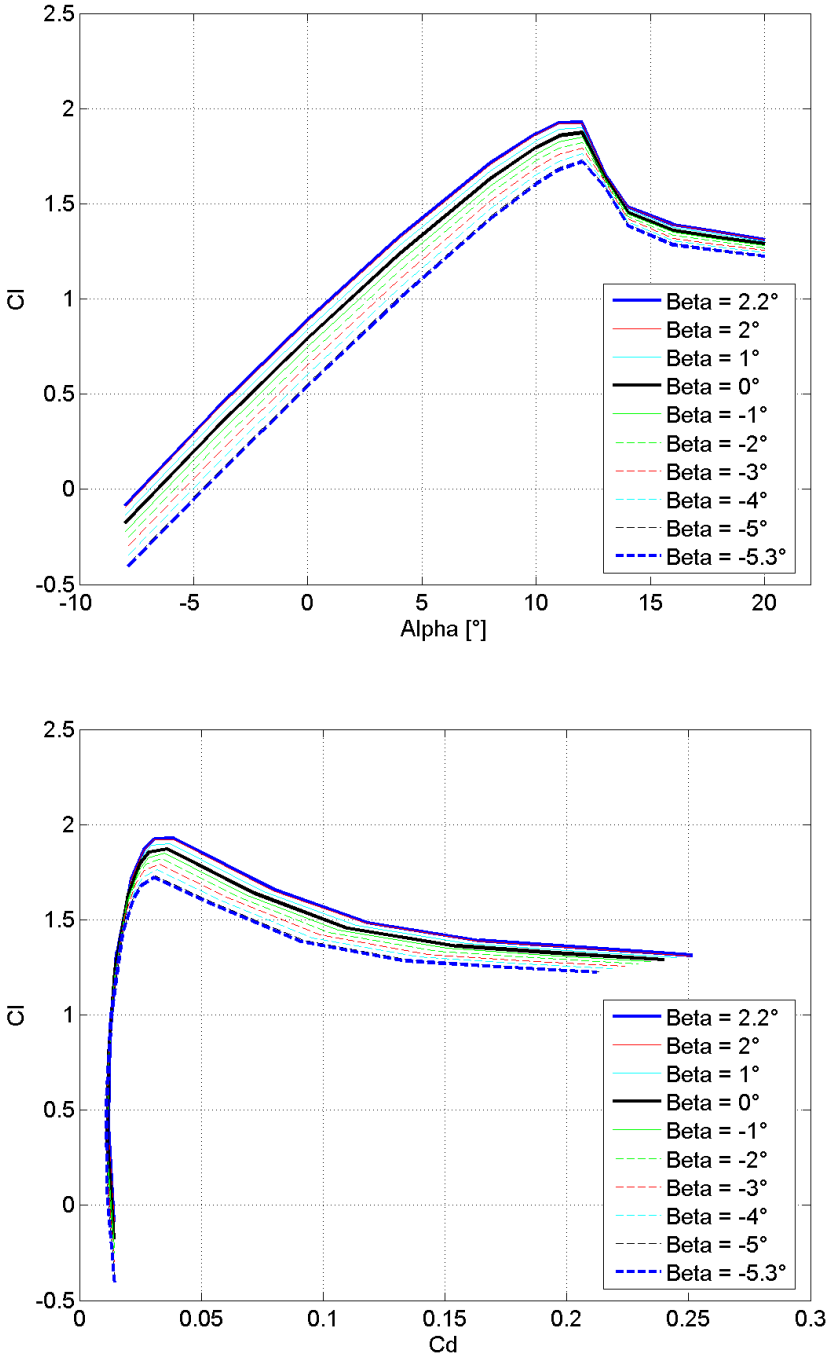

Figure 34. Polars for for several flapping angles (corrected flap)

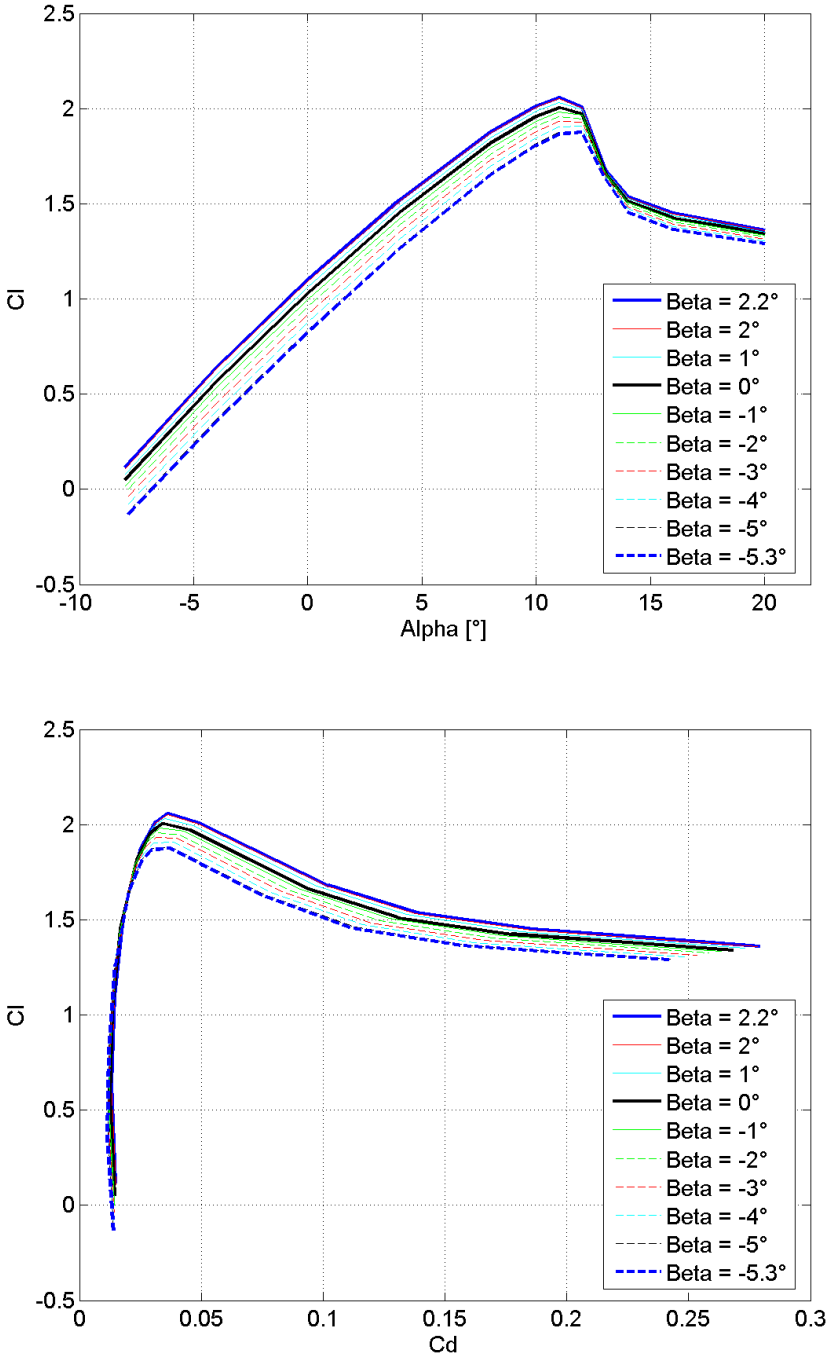

Figure 35. Polars for for several flapping angles (exactly mounted flap)

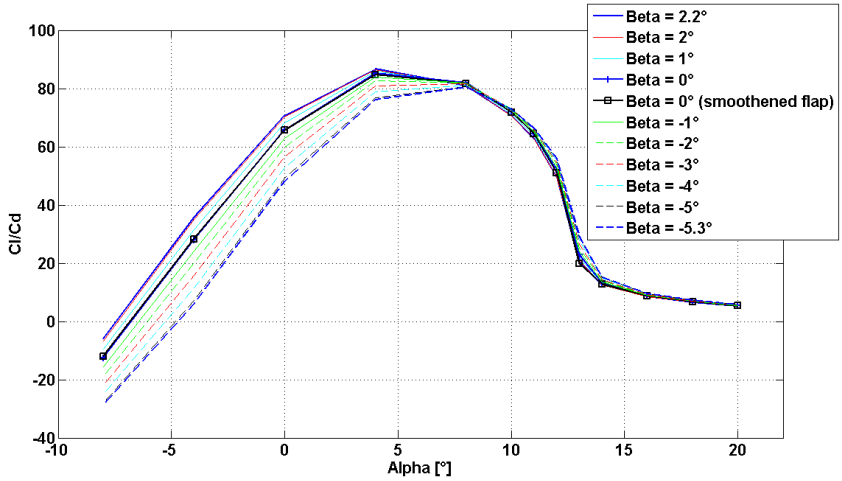

Figure 36. Gliding numbers for the corrected flap

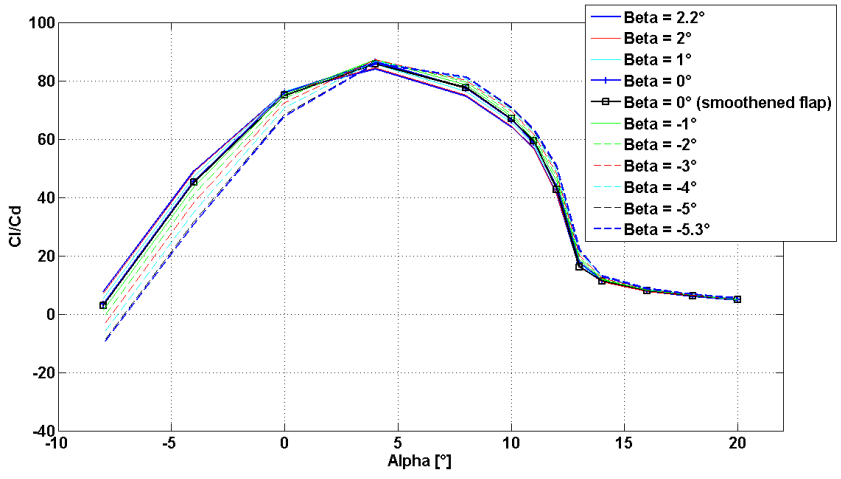

Figure 37. Gliding numbers for the exactly mounted flap

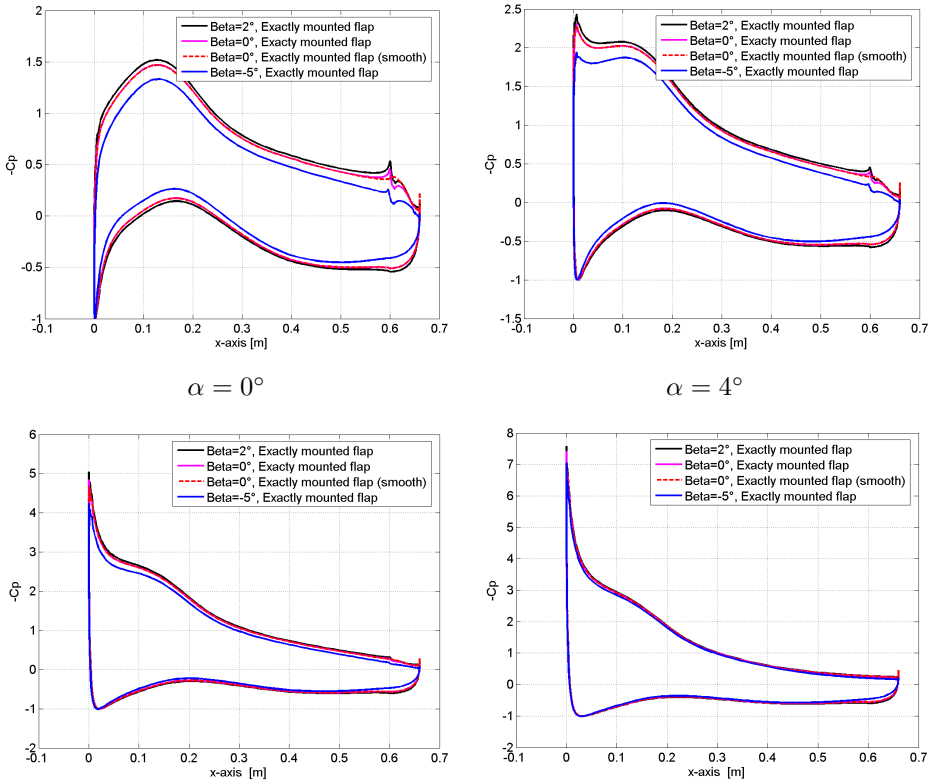

Figure 38. Pressure distributions for several AOA and flap angles

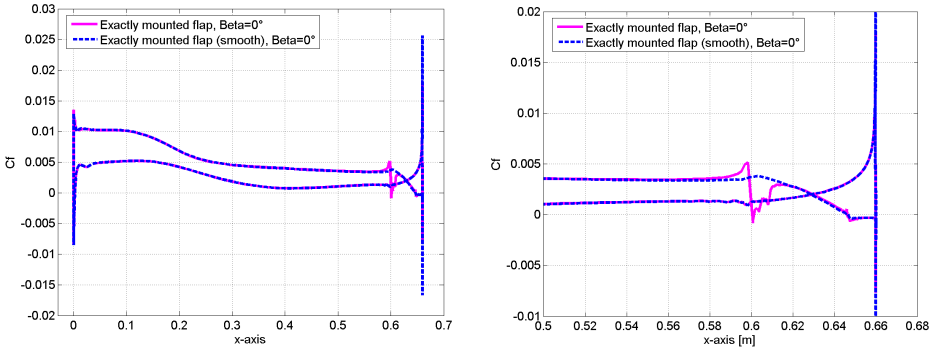

Figure 39. Skin friction coefficient at $\alpha = 0\,°$ for the smoothened and normal flap surface

7 Aeroelastic Model

This section describes how the 2 D CFD code EllipSys2D is coupled with a 3 DOF structural model of a rigid 2D airfoil section and how a fluctuating inflow can be implemented. With the new model it is then possible to investigate aeroelastic effects on a 2 D airfoil section subjected to a fluctuating inflow.
The structural model and its equations of motion are presented in Section 7.1. In Section 7.2 it is shown, how EllipSys2D is used to calculate the aerodynamic forces inside the aeroelastic model. It is explained how a fluctuating inflow and the structural motion influence the flow situation in front of the investigated airfoil and thus influence the AOA and the aerodynamic forces. Then, two different methods are discussed of how this flow situation can be described in EllipSys2D.
In Section 7.3 a flowchart of the aeroelastic model is shown. Afterwards, some comments on the non-dimensionalized calculations in EllipSys2D are done. In Section 7.4, the implemented aeroelastic model is validated with results of another aeroelastic model, using the potential flow solver of Gaunaa [7] to calculate the aerodynamic forces.

7.1 Structural Model

Figure 40 shows the 2 D airfoil section which is assumed to be situated at a certain radial position r of a rotating turbine blade. The rigid airfoil section is suspended with linear springs and dampers in order to allow structural motion in the directions of x_{struct}, y_{struct} and θ_{struct}. The springs and dampers are attached at the rotational center RC of the airfoil. The x-axis of the structural coordinate system is aligned with the rotorplane, the y-axis is perpendicular to the rotor plane. The aerodynamic forces have to be known in the same directions. F_x then corresponds to the tangential force and F_y corresponds to the thrust force. The moment F_θ around RC is defined positive in counter-clockwise direction.

The airfoil is modeled as a rigid body with a point mass m, situated at the center of gravity CG. The CG is located at a distance l from the rotational center RC. θ_{geom} is the prescribed pitch angle of the blade. It acts like an offset angle which moves the equilibrium state ($\theta_{struct} = 0$) from the rotorplane to the chordline of the airfoil. The equations of motion for this 3 DOF model are given with

$$\begin{aligned} m\ddot{x}_{struct} + c_x\dot{x}_{struct} + k_x x_{struct} = F_x &+ ml\dot{\theta}^2_{struct}\cos(\theta_{struct}+\theta_{geom}) \\ &+ ml\ddot{\theta}_{struct}\sin(\theta_{struct}+\theta_{geom}) \quad (7.1) \\ m\ddot{y}_{struct} + c_y\dot{y}_{struct} + k_y y_{struct} = F_y &+ ml\dot{\theta}^2_{struct}\sin(\theta_{struct}+\theta_{geom}) \\ &- ml\ddot{\theta}_{struct}\cos(\theta_{struct}+\theta_{geom}) \quad (7.2) \\ (I_{CG}+ml^2)\ddot{\theta}_{struct} + c_\theta\dot{\theta}_{struct} + k_\theta\theta_{struct} = F_\theta &+ ml\ddot{x}_{struct}\sin(\theta_{struct}+\theta_{geom}) \\ &- ml\ddot{y}_{struct}\cos(\theta_{struct}+\theta_{geom}) \quad (7.3) \end{aligned}$$

where I_{CG} is the moment of inertia around CG. According to Steiner's theorem, the moment of inertia for a rotation which is not around the CG is given by $I_{CG} + ml^2$.
The additional terms on the right side of the equation might need some explanation:

- Terms including $\dot{\theta}^2_{struct}$: Centrifugal force, split into its x and y components.
- Terms including $\ddot{\theta}_{struct}$: For an angular acceleration $\ddot{\theta}_{struct}$ around RC, the point mass m at a distance l accelerates with $l \cdot \ddot{\theta}_{struct}$. The resulting inertia force has to be split into its x and y components.
- Terms including $\ddot{x}_{struct}$ and $\ddot{y}_{struct}$: Additional inertia moments, due to the fact that the inertia forces $\ddot{x}_{struct} \cdot m$ and $\ddot{y}_{struct} \cdot m$ are not pointing through the rotational

center.

The same structural model was used in the work of Buhl et al. [5] and the work of Andersen [6], the only difference is that the signs of the rotational angles θ_{geom} and θ_{struct} have been changed to conform to the right hand rule and the sign conventions of EllipSys2D.

The aerodynamic forces F_x, F_y and F_θ are taken out of the CFD calculations (see Section 7.2). Knowing the aerodynamic forces and the respective structural deflections x_{struct}, y_{struct} and θ_{struct} and velocities at a certain time step n, the equations (7.1) - (7.3) are used to calculate the structural deformations at the next time step $n + 1$. This is done by using the Runge-Kutta-Nyström integration scheme.

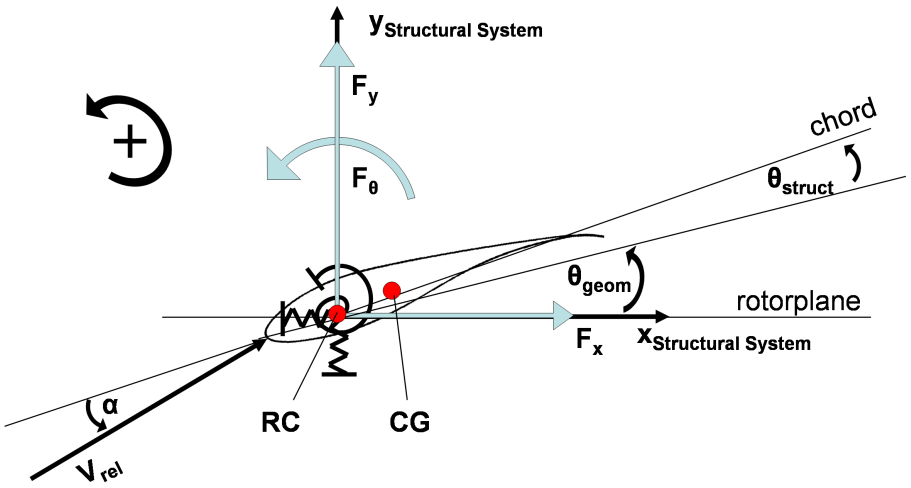

Figure 40. Notations and directions of the Structural model

7.2 Aerodynamic Model

EllipSys2D is used to calculate the aerodynamic forces generated by the investigated airfoil. During the aeroelastic simulation, the airfoil is subjected to a fluctuating inflow and to a certain movement due to structural deflections. Both the fluctuating inflow and the structural motion change the AOA for the investigated airfoil section and thus change the aerodynamic forces. In this section it is discussed how these influences can be described in EllipSys2D. Two different possibilities of realizing the fluctuating inflow are presented and their advantages and disadvantages are mentioned.
Before discussing these two possibilities in Section 7.2.2, some general definitions and terms are introduced in Section 7.2.1 which describe the simulated flow situation in front of the considered 2D airfoil section.

7.2.1 Flow situation in front of the airfoil

Flow situation excluding structural motion:

Corresponding to Figure 40, we observe a 2D airfoil section which is situated at a certain radial position r of a rotating turbine blade. If no structural deformations are taken into account, the angles and wind velocity components in front of the airfoil can be defined as illustrated in Figure 41.
Assuming that the wind direction is perpendicular to the rotor plane, the wind can be

described by the axial velocity V_a. Due to the rotational velocity of the blade at the considered radius r, an additional rotational velocity component V_{rot} has to be considered. These two velocity components add up to the relative velocity V_{rel} and the angle between V_{rot} and V_{rel} is then defined as the flow angle ϕ_{presc}. In case of a wind gust or a fluctuating inflow, this flow angle ϕ_{presc} changes over time, because the wind velocity V_a changes over time.
The pitch angle θ_{geom} is the angle from the rotorplane to the chordline. Pitching the blade is reducing (or increasing) the AOA and thus regulating the aerodynamic forces produced by the airfoil.
The resulting AOA α_{presc} is:

$$\alpha_{presc} = \phi_{presc} - \theta_{geom} \qquad \text{with } \phi_{presc} = \tan^(-1)\frac{V_{rot}}{V_a} \tag{7.4}$$

In Equation (7.4) the flow angle and the AOA have the subscript $_{presc}$. This is because the axial wind velocity V_a, the rotational speed of the blade V_{rot} as well as the pitch angle θ_{geom} will be known in advance in the upcoming EllipSys simulations. This means that the resulting flow angle ϕ_{presc} and the AOA α_{presc} are *prescribed* by that input. As soon as the computed and thus *non-prescribable* structural motion is added, the flow angle and AOA will change respectively and the subscript $_{presc}$ will be dismissed.

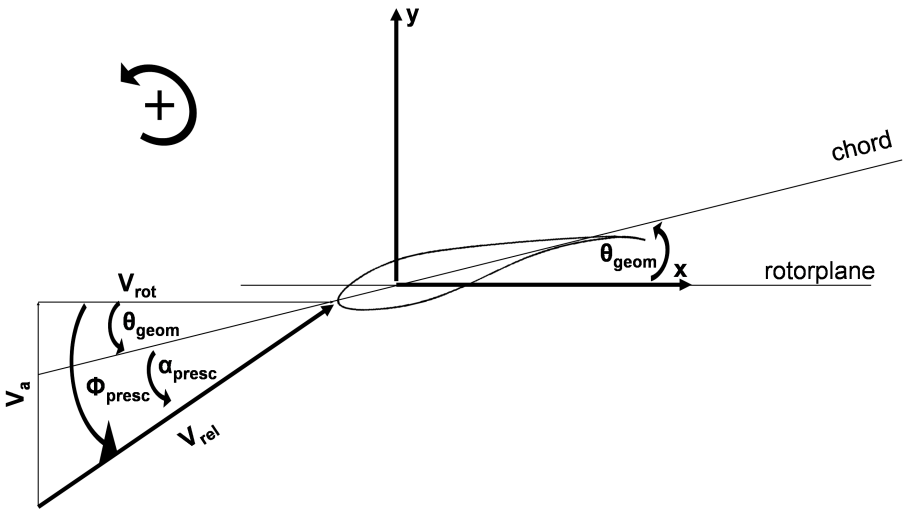

Figure 41. Definition of the angles and wind velocity components for a 2D airfoil section (structural motion excluded)

Flow situation including structural motion

In Figure 42 it is now shown, how an additional structural motion of the airfoil affects the AOA. As mentioned in Section 7.1 the structural motion in x is aligned with the rotorplane, the structural motion in y is perpendicular to the rotor plane. It is illustrated, how the velocity components $\dot{x}_{struct}$ and $\dot{y}_{struct}$ add up to the axial and rotational velocity and thus form the new flow angle ϕ. The structural motion θ_{struct} around the rotational center RC adds up to the pitch angle θ_{geom} and the new AOA α can be described with the formula:

$$\alpha = \phi - (\theta_{geom} + \theta_{struct}) \qquad \text{with } \phi = \tan^(-1)\frac{V_{rot} - \dot{x}_{struct}}{V_a - \dot{y}_{struct}} \tag{7.5}$$

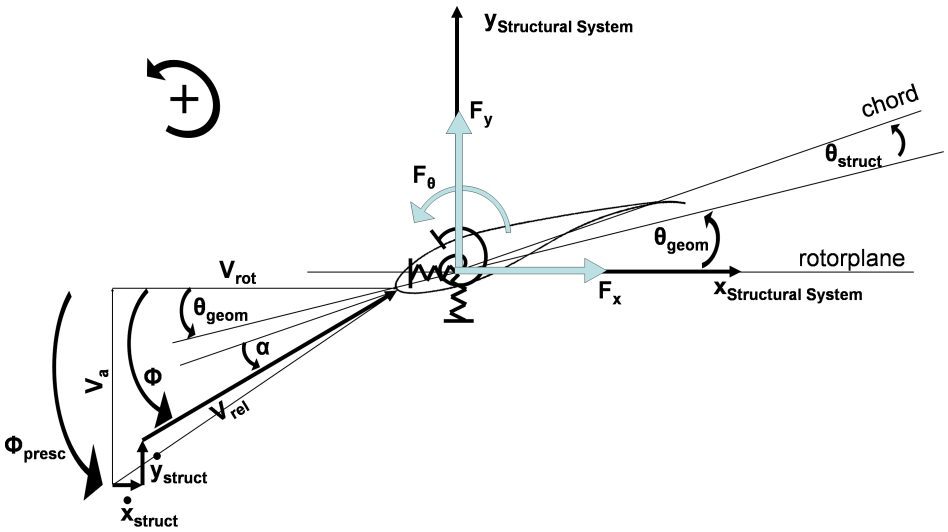

Figure 42. Definition of angles and wind velocity components for a 2D airfoil section (structural motion included)

7.2.2 Describing the Flow Situation in EllipSys2D

As mentioned in Section 2.1, EllipSys2D provides five different variables, r_x, r_y, φ, u_{inlet} and v_{inlet}, in order to adjust the AOA of the airfoil. This gives several possibilities to describe the flow situation of Figure 42.

In this section two different methods of describing the fluctuating inflow (and thus the prescribed flow angle ϕ_{presc}) are discussed. The first method uses the variable u_{inlet} and v_{inlet}, the second method uses the variable φ to describe ϕ_{presc}. The advantages and disadvantages of the two methods will be pointed out and finally one method will be chosen for the upcoming simulations.

Method 1: Using u_{inlet} and v_{inlet} to describe ϕ_{presc}:

This method is quite intuitive and seems to be easy. As illustrated in Figure 43 the change in the prescribed flow angle ϕ_{presc} is accomplished by changing the inlet velocity components u_{inlet} and v_{inlet} according to V_{rot} and V_a.
Changes in θ_{geom} and θ_{struct} can be realized by rotating the grid with $\varphi = \theta_{geom} + \theta_{struct}$.
Remember from Figure 1 that a rotation in φ does not change the orientation of the CFD coordinate system. This means that during the whole simulation the coordinate system of EllipSys2D (in which the aerodynamic forces are calculated) is aligned with the coordinate system of the structural motion (in which the structural deflection is calculated) which is the big advantage of this method.
Due to the aligned coordinate systems the structural motions x_{struct} and y_{struct} out of the structural model do not have to be rotated and can simply be used for r_x and r_y inside ElipSys2D. The same can be said about the forces $F^*_{x,CFD}$ and $F^*_{y,CFD}$ out of the CFD calculations. They can be used inside the structural model without any rotational transformation.

The input to EllipSys2D would be:

$$u_{inlet} = V^*_{rot}; \qquad v_{inlet} = V^*_a; \qquad r_x = x^*_{struct}; \qquad r_y = y^*_{struct}$$
$$\varphi = \theta_{geom} + \theta_{struct}$$

The input to the structural model would be:

$$F_x = F^*_{x,CFD} \cdot f_{dim,f}; \qquad F_y = F^*_{y,CFD} \cdot f_{dim,f}; \qquad F_\theta = F^*_{\theta,CFD} \cdot f_{dim,m}$$

where the * stands for a non-dimensionalized quantity. $f_{dim,f}$ and $f_{dim,m}$ are dimensionalization factors. (See Appendix A for more information on the non-dimensionalized quantities used in EllipSys2D)

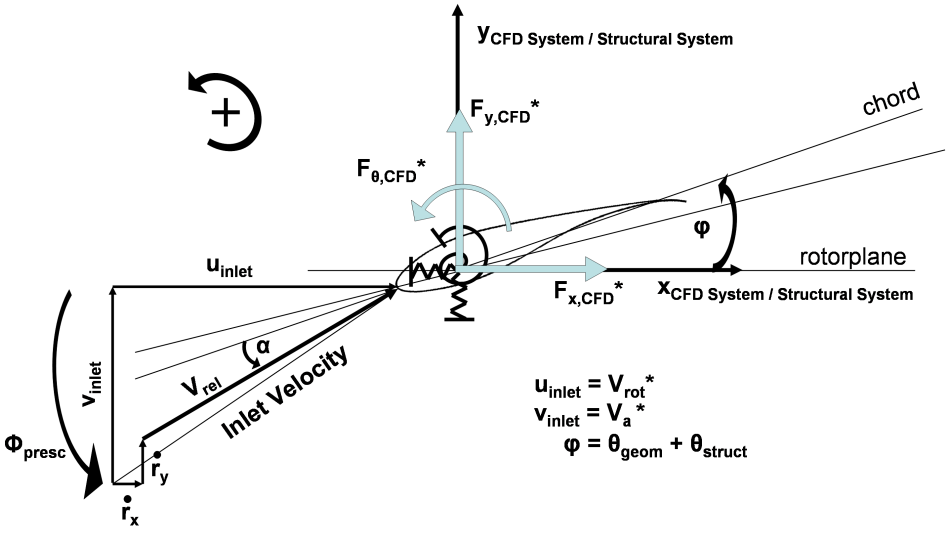

Figure 43. Flow angle ϕ_{presc} defined via u_{inlet} and v_{inlet}

But there are several drawbacks of this method. EllipSys2D is an incompressible flow solver. Thus, at every time step, the mass flux into the computational domain has to be equal to the mass flux out of the domain in order to fulfil the global mass conservation. Changing the inlet velocities u_{inlet} and v_{inlet} due to a fluctuating inflow means that the mass flux into the domain is changing continuously. In reality a change in the inflow velocity needs some time to travel downstream and influence the flowfield around and behind the airfoil. However, in incompressible CFD computations the mass flux at the outlet has to be immediately adapted to the change in inflow in order to maintain global mass conservation. This means that an increase in the inflow velocity results in an immediate and thus unphysical increase of the outlet velocity. As a consequence the whole flow field inside the computational domain is jumping to a higher velocity level which is not physical either. A possibility to overcome this problem is to continuously scale the changing inflow velocities in order to keep the total mass flux constant.
A second drawback is the problem of timing. Using an O-mesh around the airfoil the inlet boundaries are located in an oval arc around the airfoil (see Figure 1) and thus each inlet cell varies in its x and y coordinates. In order to describe a uniform fluctuation in the velocity components of x and y (i.e. u and v) the inlet velocities have to be altered in a certain time sequence.
Due to these rather laborious changes it was decided to look for an easier possibility to implement the fluctuating inflow.

Method 2: Using φ to describe ϕ_{presc}:

This method is illustrated in Figure 44. The change in the flow angle ϕ_{presc} is now accomplished by rotating the movable mesh of EllipSys2D with $\varphi_\phi = -\phi_{presc}$ while the inlet direction defined via u_{inlet} is kept constant ($v_{inlet} = 0$). This means that the inlet

velocity remains perpendicular throughout the whole computation (see Figure 1). In order to obtain the same flow situation as in Figure 42 the CFD coordinate system has to be rotated with ϕ_{presc}.
Changes in θ_{geom} and θ_{struct} are realized by rotating the mesh with $\varphi_\theta = \theta_{geom} + \theta_{struct}$ and the overall rotation of the movable mesh is then given with $\varphi = \varphi_\phi + \varphi_\theta = -\phi_{presc} + \theta_{geom} + \theta_{struct}$.

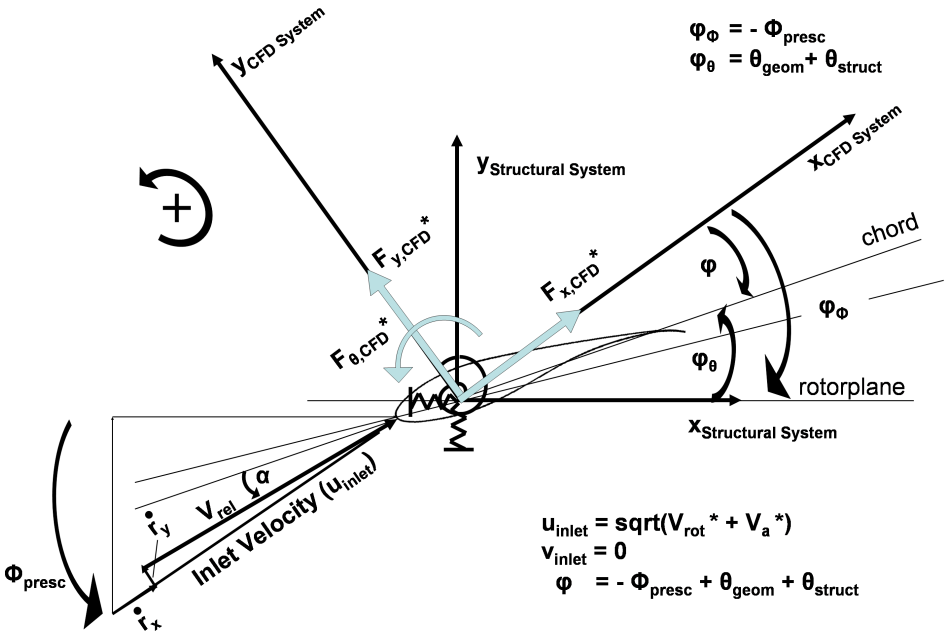

Figure 44. Flow angle ϕ_{presc} defined via φ

The rotation of the CFD coordinate system complicates the problem, since the structural motions x_{struct} and y_{struct} have to be rotated by the angle ϕ_{presc} before they can be used inside EllipSys. The same holds for the aerodynamic forces $F_{x,CFD}*$ and $F_{y,CFD}*$ out of EllipSys2D. They have to be rotated by the angle $-\phi_{presc}$ before they can be used inside the structural model.

The input to EllipSys2D is then:

$$\begin{aligned} u_{inlet} &= \sqrt{{V_{rot}^*}^2 + {V_a^*}^2} \stackrel{!}{=} 1 \\ v_{inlet} &= 0 \\ r_x &= x^*_{struct}\cos\phi_{presc} + y^*_{struct}\sin\phi_{presc} \\ r_y &= y^*_{struct}\cos\phi_{presc} - x^*_{struct}\sin\phi_{presc} \\ \varphi &= -\phi_{presc} + \theta_{geom} + \theta_{struct} \end{aligned} \tag{7.6}$$

The input to the structural model is then:

$$\begin{aligned} F_x &= (F^*_{x,CFD}\cos\phi_{presc} - F^*_{y,CFD}\sin\phi_{presc}) \cdot f_{dim,f} \\ F_y &= (F^*_{x,CFD}\sin\phi_{presc} + F^*_{y,CFD}\cos\phi_{presc}) \cdot f_{dim,f} \\ F_\theta &= F^*_{\theta,CFD} \cdot f_{dim,m} \end{aligned} \tag{7.7}$$

where the * stands for a non-dimensionalized quantity. $f_{dim,f}$ and $f_{dim,m}$ are dimensionalization factors. (See Appendix A for more information on the non-dimensionalized

quantities used in EllipSys2D)

Changing the inflow by rotating the airfoil does not fully correspond to the real case. In reality a change in the wind field in front of the airfoil needs some time to travel down the airfoil. In the simulation, due to the rotation of the airfoil, the change in the wind velocity is felt imediately at all positions of the blade. However, this withdraw of method 2 is assumed to have minor effects on the computed forces. A respective investigation of this is mentioned in [5] using potential flow theory. On the other hand, by using method 2 the difficulties of implementing method 1 can be circumvented and it is therefore decided to use method 2 for the aeroelastic modeling in this work.

7.3 Flowchart of the aeroelastic model

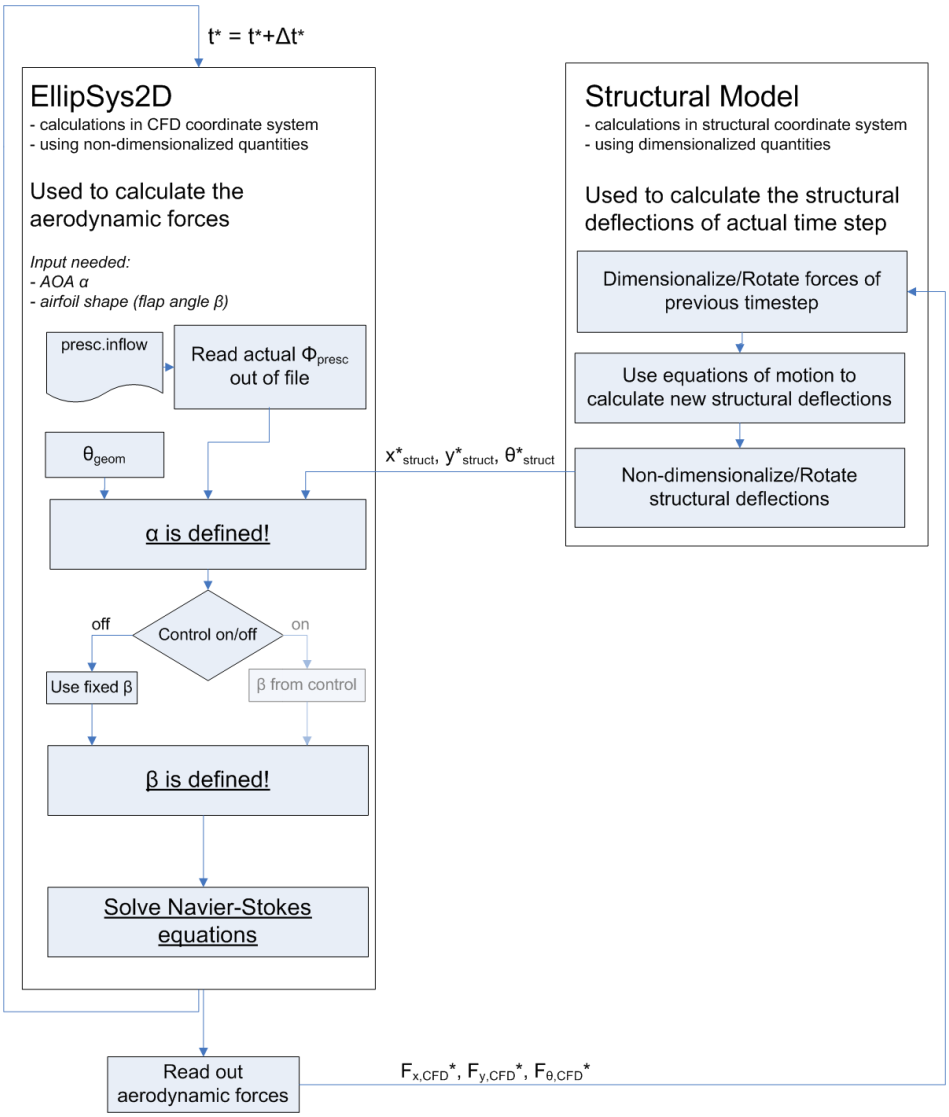

Figure 45. Coupling between EllipSys2D and structural model

In Figure 45 it is shown, how EllipSys2D is coupled with the structural model. At each time step of the CFD computations, the AOA α as well as the flap angle β have to be determined in order to calculate the correct aerodynamic forces. The AOA α is adjusted by

using the equations of (7.6). The prescribed flow angle ϕ_{presc} is read out of a file called *presc.inflow*. The file contains a time series of the flow angle ϕ_{presc} which corresponds to the desired inflow situation (wind gust or turbulent wind field). The pitch angle θ_{geom} is a fixed given value. x^*_{struct}, y^*_{struct} and θ^*_{struct} are given by the structural model. As long as no control is implemented, a fixed flap angle β is used.
After the resulting flowfield is computed, the forces $F^*_{x,CFD}$, $F^*_{y,CFD}$ as well as the moment $F^*_{\theta,CFD}$ around RC are determined and given to the structural model.
In the structural model, the aerodynamic forces are dimensionalized and rotated into the structural coordinate system (see equation (7.7)). The forces are then used inside the equations (7.1) - (7.3) in order to calculate the structural displacements at the next time step with the Runge-Kutta-Nyström scheme. The structural deflections are non-dimensionalized before they are given back to EllipSys.

7.4 Validation of the Model

Validation of the time integration scheme:

First, the correct implementation of the Runge-Kutta-Nyström time integration scheme is checked. This is done by solving the 2nd order ordinary differential equation

$$m\ddot{x} + kx = F_0 \cos(\omega t) \tag{7.8}$$

which describes the response x of a 1 DOF system, suspended on a spring k and subjected to a harmonic external load F_0. No damping is included.
For equation (7.8) an exact, analytical solution exists which can be compared with the solution of the Runge-Kutta scheme. The analytical solution is given by

$$x(t) = \frac{F_0}{m(\omega_0^2 - \omega^2)} \cos(\omega t) + (x_0 - \frac{F_0}{m(\omega_0^2 - \omega^2)}) \cos(\omega_0 t) + \frac{\dot{x}_0}{\omega_0} \sin(\omega_0 t)$$

where $\omega_0 = \sqrt{k/m}$ is the natural frequency of the system and x_0, $\dot{x_0}$ are the initial conditions of the system.
In Figure 46 the two solutions for $F_0 = 10\,\text{N}$, $m = 1\,\text{kg}$, $k = 100\,\text{N/m}$, $\omega = 5\,\text{s}^{-1}$ and the initial conditions $x_0 = 0\,\text{m}, \dot{x_0} = 0\,\text{m/s}$ are compared to each other. The computed positions, velocities and accelerations coincide very well.

Time step in the structural model

The input parameters of the validation case are chosen such that the magnitudes of position, velocity and acceleration are comparable to what can be expected in later aeroelastic computations. Normally, it has to be investigated which time step is suitable to capture the fluctuations in x accurately. But here the time step of the Runge-Kutta scheme is not considered to be critical as it is coupled with the time step of EllipSys2D. Using the non-dimensional time step of $\Delta t^* = 0.01$ in EllipSys2D (see Chapter 4), the corresponding time step in the Runge-Kutta scheme is $\Delta t = 0.00017\,\text{s}$ (see equation (A.11) for $c = 1\,\text{m}$ and $U_\infty = 60\,\text{m/s}$) which is small enough to resolve any kind of physical motion of the airfoil section. In Figure 46 a time step of $\Delta t = 0.00017\,\text{s}$ is used.

Validation of the aeroelastic model:

The 3 DOF aeroelastic model is now compared to another aeroelastic model, which uses the potential flow solver of Gaunaa [7] and the dynamic stall model of Andersen [9] to calculate the aerodynamic forces. For the comparison the Risø B1-18 baseline airfoil is used where no flap is attached. At $t = 1\,\text{s}$ the airfoil is exposed to a wind gust which

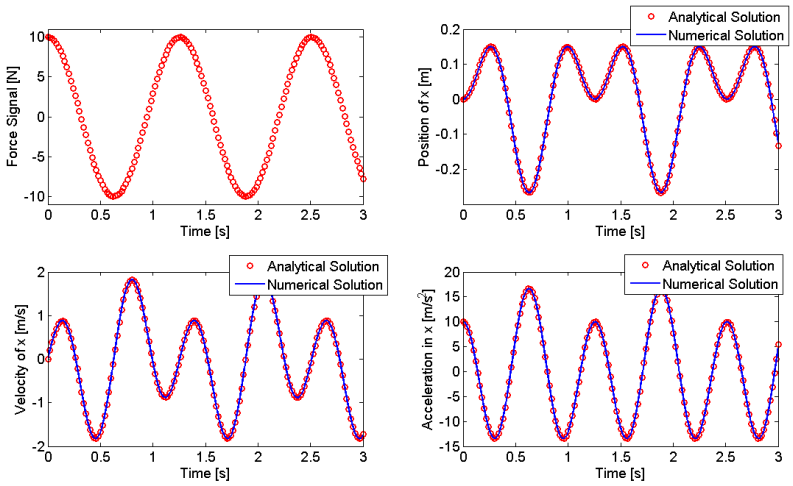

Figure 46. Comparison between the analytical and numerical solution ($F_0 = 10\,N$, $m = 1\,kg$, $k = 100\,N/m$, $\omega = 5\,1/s$, $\Delta t = 0.00017\,s$

corresponds to a step change in the axial wind velocity V_a from 10 m/s to 12 m/s. The rotational velocity remains at 60 m/s. The air density is $\rho = 1.225\,\text{kg/m}^3$. The rotational center RC and the center of gravity CG are both assumed to be situated on the chordline of the airfoil. All quantities used in the structural model are listed in Table 3. Structural damping is neglected. The time step is $\Delta t^* = 0.01$ or $\Delta t = 0.00017\,\text{s}$

Table 3. Structural quantities used in this work

RC (distance from LE)	0.30 m
CG (distance from LE)	0.35 m
m (per unit depth)	40 kg
k_x	6316 N/m
k_y	1579 N/m
k_θ	8290 N/rad
c_x, c_y, c_θ	0 Ns/m
θ_{geom}	5 °

The two calculations are compared in Figures 47 and 48. The time line in these figures starts at $t = 0\,\text{s}$ but the simulations were already started at $t = -3\,\text{s}$ in order to reach a structural equilibrium position before the step change in wind takes place. However, the oscillations in the (nearly) edgewise direction x_{struct} damp out very slowly and are still present at $t = 0\,\text{s}$.

In Figure 47 it can be seen that the calculated structural deflections x_{struct}, y_{struct} and θ_{struct} of the two models fit excellently together. Both the absolute values and the dynamic behaviour are nearly identical. In the results for y_{struct} it can be seen that the curve out of the CFD computation shows a somewhat softer or delayed reaction to the simulated step change. This slight delay can also be seen in the results for θ_{struct}. The reason for that is that the wind step in EllipSys2D can not be simulated with an immediate change and the maximum change in the wind velocity V_a has to be limited in order to omit unrealistic transient forces which evoked very high and unrealistic oscillations in θ_{struct} and y_{struct}. (see Appendix B for more information).

The comparison of the normal and tangential force coefficients C_n and C_t in Figure 48 shows a very good correlation as well. However, some differences can be pointed out

in the dynamic behaviour of the curves as the force signals of the potential flow solver appear more vivid and oscillating while the results of the CFD computations seem more damped. The damping in the CFD calculations might stem from viscous effects in the flowfield which are not taken into account in the potential flow model. It should be mentioned that the oscillations are mainly due to the structural oscillation in x_{struct}. Blocking that DOF leads in both models to non-oscillating force signals.

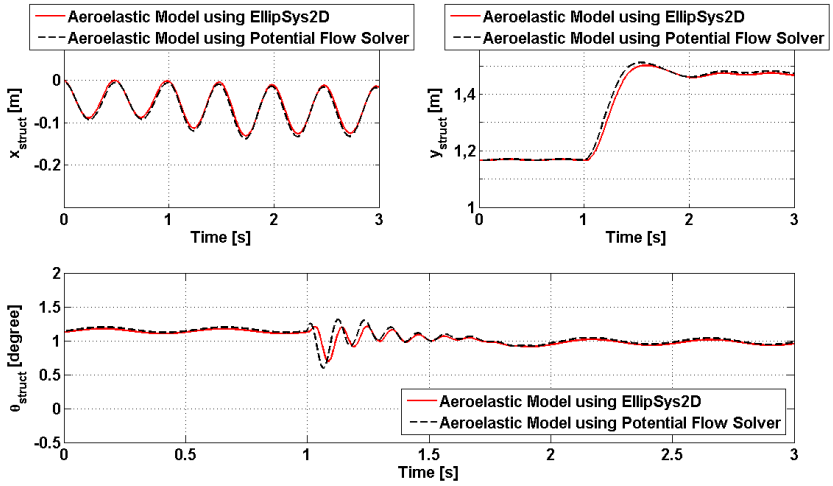

Figure 47. Comparison between potential flow and EllipSys results for a step change in V_a, baseline airfoil (no flap), structural quantities as given in Table 3

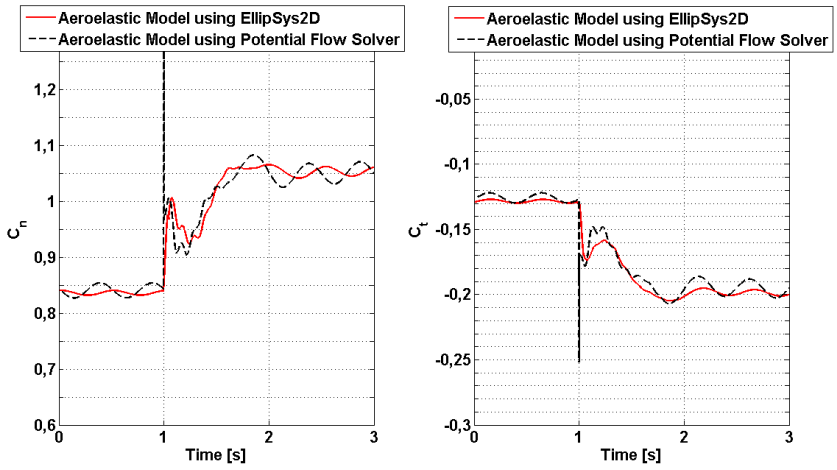

Figure 48. Comparison between potential flow and EllipSys results for a step change in V_a, baseline airfoil (no flap), structural quantities as given in Table 3

8 Aero-Servo-Elastic Model

The aeroelastic model is now extended with a control algorithm for the flap movement. The flap movement should reduce the fluctuations in the aerodynamic loads which are due to the unsteady wind field seen by the blade. Reducing the fluctuations of the aerodynamic loads leads to a reduction in the structural oscillations and the fatigue loads of the blade.

In this work two different control strategies are implemented. Control 1 is using the AOA α_{meas} measured in front of the airfoil as input. Control 2 is using the pressure difference Δp_{meas} between the pressure and suction side at a certain chord position as input. The two controls were implemented in this model as they promise a high reduction potential of the fatigue loads (see Reference [5] and [19]).

8.1 Control 1

This control uses the AOA in front of the airfoil as input. The inflow angle can for instance be measured with a 5-hole pitot tube which measures the AOA in a certain distance d_1 in front of the LE (see Figure 49). A change in the measured AOA indicates that the lift force is changing and the control then tries to counteract the lift change by actuating the flap adequately. Previous simulations with a potential flow solver showed that the potential of load reduction with a control using the AOA as input was higher than with a control using the structural deflection y_{struct} and/or velocity $\dot{y}_{struct}$ as input ([5]).

The control algorithm is given by:

$$\beta = (\frac{2\pi}{H_{dydx}}(\alpha_{meas} - \alpha_{ref})) \cdot A_\alpha + \beta_m \tag{2}$$

where α_{meas} is the AOA measured with the pitot tube. A_α is the gain parameter of the control and α_{ref} denotes the integral term

$$\alpha_{ref} = \frac{1}{\tau}\int_{t-\tau}^{t} \alpha_{meas}(t)\, dt \tag{3}$$

which is the average value of α_{meas} during a reference time window τ.

This control algorithm is based on the algorithm found in [5]. It aims at keeping the actual AOA α_{meas} close to the reference value α_{ref} and deviations between those two values lead to a change in β (see equation (2)). The parameter H_{dydx} represents the potential of the airfoil to change the lift via flapping. It corresponds to the slope $dC_l/d\beta$ which in Chapter 6 was described as the effectiveness of the flap. H_{dydx} is used to relate the deviation between α_{meas} and α_{ref} to a reasonable change in the flap deflection angle β which counteracts the change in lift. The parameter depends on α and β, but in the following computations this dependency is neglected and an average value of $H_{dydx} = -2rad^{-1}$ is used. However, the gain parameter A_α is used to fine tune the efficiency of the control. The computed change in β is then added to the middle position β_m of the flap. Thus the control always orients at the middle position and ensures that the flap can react to both sides into the same extent.
The calculations in Chapter 9 are carried out assuming a pitot tube length of $d_1 = 0.3 \cdot c$.

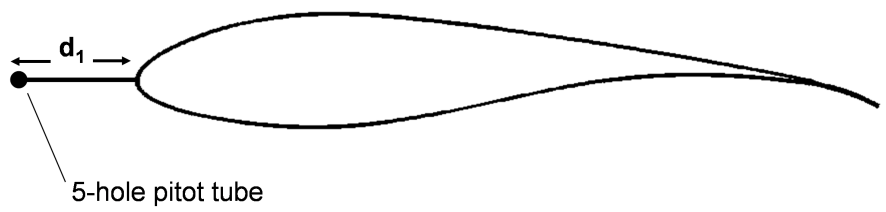

Figure 49. Control 1: Pitot tube attached at d_1 in front of the LE

Getting α_{meas} out of EllipSys2D:

In EllipSys2D the pitot tube in front of the LE is not modeled as a solid body, instead it was decided to simply extract the velocity components u and v at a certain point/cell in front of the airfoil. The model is thus neglecting the influence of the pitot tube on the flow field in front of the airfoil, however, this influence is considered to be very modest. In order to ensure that the velocity extraction point stays at a fixed distance to the airfoil, it has to be located inside the rigid part of the moving mesh.
The extracted velocity components u_{extr} and v_{extr} are given in the directions of the CFD coordinate system. In Figure 50 it is shown that the corresponding angle α_{extr} is the angle between the x axis of the CFD coordinate system and V_{rel}. But the desired AOA α_{meas} is defined as the angle between the chordline of the airfoil and V_{rel}. As soon as the airfoil and thus the moving mesh is rotated by a certain angle φ (refer to Figure 1), the chordline deviates from the x axis of the CFD coordinate system and the additional rotation has to be considered. This leads to the expression of

$$\alpha_{meas} = \alpha_{extr} - \varphi = atan(v_{extr}/u_{extr}) - \varphi \tag{4}$$

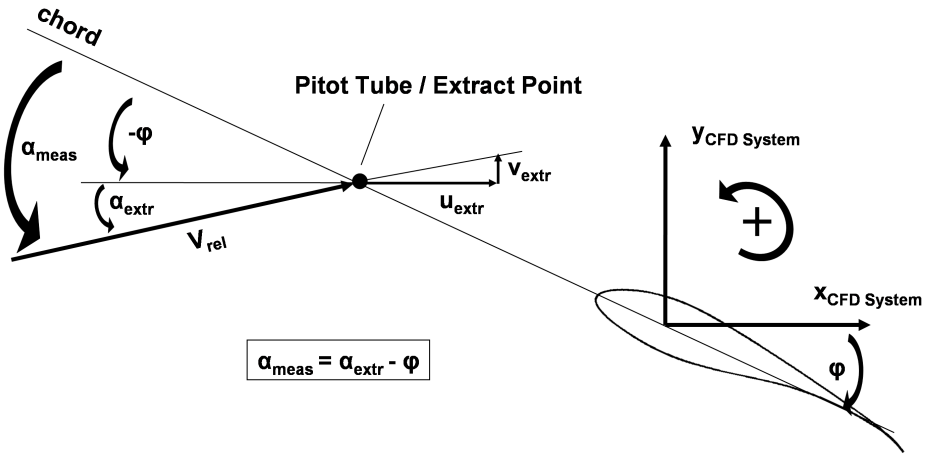

Figure 50. Getting α_{meas} out of EllipSys2D

8.2 Control 2

This control uses the pressure difference Δp_{ref} at a certain point between pressure and suction side as input. As seen in Figure 51, pressure taps were mounted at a distance d_2 from the LE in order to determine the pressure difference. A change in the measured pressure difference indicates a change in the aerodynamic loading and the control then tries to counteract by actuating the flap in order to keep the pressure difference close to a certain reference value. Previous aero-servo-elastic simulations using a potential flow solver for the aerodynamic modeling promised a big potential in load alleviation for this control ([19]).

The control algorithm is given with:

$$\beta = (\Delta p_{meas} - \Delta p_{ref}) \cdot A_p + \beta_m \tag{5}$$

where Δp_{meas} is the measured pressure difference between the upper and lower pressure tap. A_p is the gain parameter of the control and Δp_{ref} denotes the integral term

$$\Delta p_{ref} = \frac{1}{\tau} \int_{t-\tau}^{t} \Delta p_{meas}(t)\, dt \tag{6}$$

which is the average value of Δp_{meas} during a reference time window τ.

In equation (5) it can be seen that deviations between the two values will lead to a change in β. It is the task of the gain parameter A_p to translate this change in pressure into a reasonable change of the flap deflection angle. In difference to (4) the gain of control 2 is a dimensionalized quantity as a corresponding prefactor to $2\pi/H_{dydx}$ has not been determined yet in previous work.
The resulting change in β is added to the flap deflection angle β_m which should be the middle position between β_{max} and β_{min}. The control returns to that middle position if no change in β is needed (Δp_{meas} is equal to Δp_{ref}) and maintains the possibility that the flap can react to both sides in the same extend.
The calculations in Chapter 9 are carried out with pressure taps located at $d_2 = 0.12 \cdot c$ as computations using a potential flow solver showed good results at this measurement position of the Risø B1-18 airfoil. A favoured position for the pressure taps is supposed to be located where a change in lift evokes distinct changes in Δp_{meas} and the optimum point might thus change if another airfoil than the Risø B1-18 is chosen.

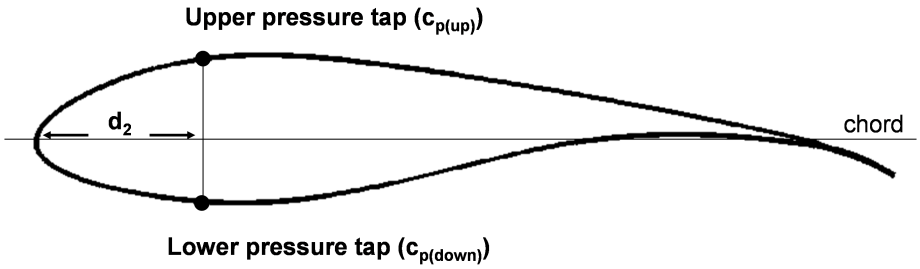

Figure 51. Control 2: Pressure taps at d_2 to measure the pressure difference

Getting Δp_{meas} out of EllipSys2D:

The pressure taps are measuring the pressure on the airfoil surface at a given distance d_2 from the leading edge. A little routine inside the EllipSys code is identifying the two surface cells of the pressure and suction side which are located closest to the given distance d_2. The read out c_p values are then translated to the dimensionalized pressure difference

$$\Delta p_{meas} = (c_{p(up)} - c_{p(down)}) \cdot \frac{1}{2} \rho U_\infty^2 \tag{7}$$

using the freestream dynamic pressure to dimensionalize.

8.3 Reference Time Window

The values Δp_{ref} and α_{ref} are used as reference values inside the control algorithms. These values are a kind of optimum value and the control reacts as soon as the state variables α_{meas} or Δp_{meas} deviate from these references. The optimum values are defined by averaging previous values over a certain time window τ (see equation (6) and (3)). To get an effective control, it is important to choose an adequate reference time τ.

- Choosing a very long time window τ will lead to slow changes in the optimal values and the control will try to even cancel out very slow variations in Δp (Control 1) or AOA (Control 2). An example for slow variations could be the change in Δp or AOA due to a change in wind speed from 5 m/s 25 m/s. A long time window would keep the reference values close to the values measured at 5 m/s, and the flap would try to alleviate these big changes in the aerodynamic loading. But it makes no sense and is just impossible to alleviate these variations with the flap.
- Choosing a very short time window τ will lead to quick changes in the optimal values. Small fluctuations in the aerodynamic loading, due to turbulences in the wind, might not be filtered out as much as desired.

According to previous work the time window reference is chosen to be $\tau = 6\,\mathrm{s}$. This corresponds to 1 full blade rotation of a 10MW turbine. Variations which are slower than this 1P period are expected to be regulated by the pitch control. All quicker fluctuations in the wind field and thus in the aerodynamic forces should then be alleviated by the flap.

8.4 Maximum Actuation Velocity, Maximum Flap Angles, Time Delay

Maximum Actuation Velocity

The piezoelectric flaps have some limitations on their actuation velocity. Out of experiments the flap needs approximately $1/100\,\mathrm{s}$ to get from $\beta = 2,2\,^\circ$ to $\beta = -3\,^\circ$ (flapping up) while it needs approximately $4/100\,\mathrm{s}$ to get from $\beta = -3\,^\circ$ to $\beta = 2,2\,^\circ$ (flapping down). Neglecting acceleration and deceleration effects this gives a maximum actuation velocity of $-520\,^\circ/s$ and $+130\,^\circ/s$ respectively. The maximum deflection angles per time step Δt of the aero-servo-elastic computations are thus

$$\Delta\beta_{max,down} = -520\,^\circ/s \cdot \Delta t\,; \quad \Delta\beta_{max,up} = 130\,^\circ/s \cdot \Delta t \tag{8}$$

In case the desired $\Delta\beta$ of the control algorithm is bigger then the one given in equation (8), the desired value is overwritten and the maximum value is used instead.

Maximum Flap Angles

The maximum flap deflection range is set to $2.2\,^\circ \leq \beta \leq -5.3\,^\circ$. This corresponds to the maximum static deflection which could be reached with the prototype. Further restrictions on the maximum flapping range which occurred during the wind tunnel tests are not considered here, as they were due to the limitations of the used amplifier (see Chapter 5).

Time Delay

In order to make the computations more realistic a certain time delay t_{delay} can be introduced to the computations. This time delay accounts for the time needed to receive the signal from the measurement device, process it in the control and to finally put the response signal to the flap actuator. Former investigation in [5] and [6] showed that the load reduction potential of the flap control is very much influenced by time delays. Thus it was considered to be important to include a time delay investigations to the present work. The time delay is realized by a simple time shift inside the code. This means that the control algorithm uses measured state variables which stem from the time $t = t_{now} - t_{delay}$.

8.5 Flowchart of the Aero-Servo-Elastic Model

The implementation of the control into the existing aero-elastic model of Chapter 7 is shown in Figure 52. The flap deflection angle β is taken out of the control algorithm which uses the extracted values $c_{p(up)}$ and $c_{p(down)}$ or α_{extr} of the previous time step as input. The corresponding Δp_{meas} and α_{meas} are then calculated with equation (7) or (4). After determine the respective reference values (equation (6) or (3)) and introducing a possible time delay, the respective control algorithm is solved in order to determine the desired new flap angle β. Finally it is checked if the desired flap movement has to be limited due to the restrictions of the maximum flapping velocity.
The grid of the new airfoil shape is then generated with a linear interpolation between the

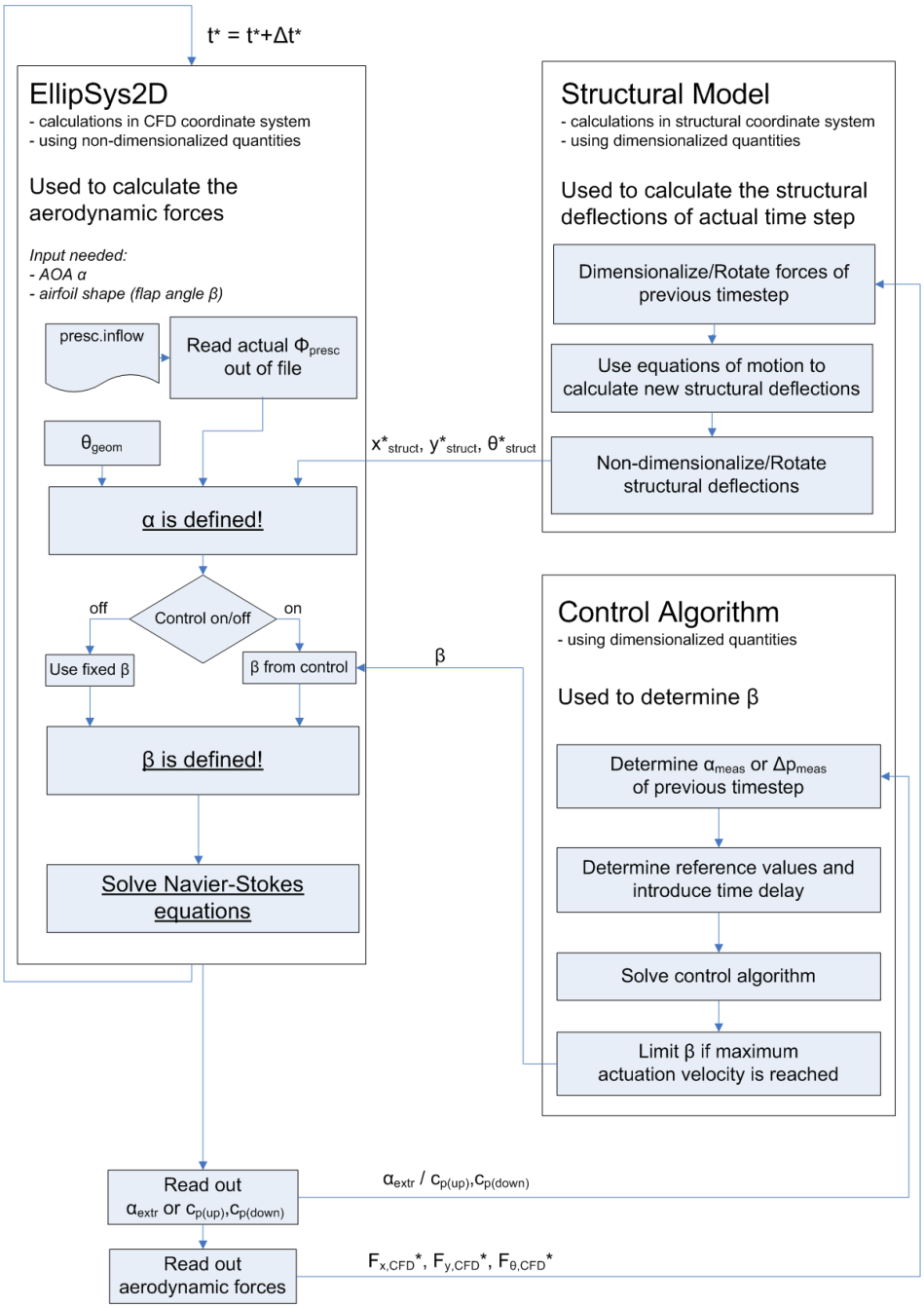

Figure 52. Flowchart of the aero-servo-elastic Model

maximum grids for $\beta_{min} = -5.3\,^\circ$ and $\beta_{max} = 2.2\,^\circ$ (as explained in Chapter 2.2).

9 Results of Test Cases

The 2D airfoil section equipped with the piezoelectric flap is now exposed to different wind situations and its ability to reduce the fatigue loads is investigated. The reduction of the fatigue loads is measured by comparing the respective standard deviations $Std(y)$ of the structural deflections in y_{struct} (see Section 9.1).
For both controls several gain parameters are tested in order to obtain information about the optimal gain values and the respective reduction potential in $Std(y)$. These investigations are first carried out for a step change in wind from $V_a = 10$ m/s to $V_a = 10.5$ m/s (Section 9.2), then the same investigations are done for a 4 seconds turbulent wind field signal with $TI = 2.2\%$ (Section 9.3). Additionally, the same turbulent inflow is used to examine the control's dependency on possible time delays inside the control loop.
In the last two sections results of longer simulation runs are shown. Using the optimal gain values determined in the previous section and assuming no time delay in the control loop, the two controls are used to alleviate the structural deflections in y_{struct} evoked by a 12 seconds turbulent windfield signal. Both a turbulent wind field with $TI = 2.4\%$ (Section 9.4) and a turbulent wind field with $TI = 7.7\%$ (Section 9.5) is simulated. To alleviate the fluctuations of the wind field with $TI = 7.7\%$ the controls seek for higher flap deflection angles than the actual maximas of $\beta_{min} = -5.3\,^\circ$ and $\beta_{max} = 2.2\,^\circ$. Therefore the last simulation is carried out with extended flap deflection limits of $\beta_{min} = -6\,^\circ$ and $\beta_{max} = 6\,^\circ$ in order to demonstrate the load reduction potential using future piezoelectric actuators as deformable TE flaps.

In the simulations of this chapter the DOF in x_{struct} is blocked as for the relatively short simulation runs the oscillations in x_{struct} are mainly related to the chosen initial conditions and not to any aerodynamic effects. Thus the oscillations in x_{struct} do not effect the conclusions about the load reduction potential of the flap. Additionally the reduction potential is determined via the standard deviation $Std(y)$ in y_{struct} which is likewise not affected significantly by blocking the structural motion in x_{struct}.

To achieve comparable starting conditions for the several test cases the computations were started a certain time before $t = 0$ s. Thereby the equilibrium state of y_{struct} and θ_{struct} is reached and the computations start from a settled flow field around the airfoil. In C a typical input file of EllipSys is shown which inter alia gives detailed information about the chosen time sequence of a typical simulation. Additionally, information about the required computational time is given there.

9.1 Definition of $Std(y)$ and reduction potential $R_{Std(y)}$

The implemented control algorithms aim to reduce the fluctuations in the aerodynamic loads and thus reduce the associated fatigue loads on a wind turbine blade subjected to a fluctuating wind field. Compared to the fluctuations in drag the changes in the lift force are much more pronounced. Additionally, the lift force acts mainly into the flapwise blade direction where the blade stiffness is lowest. The highest variations in the structural deformations are thus expected in the flapwise blade direction which is in turn close to the y-direction of the structural coordinates (see Figure 40).
It is therefore decided to compare the implemented control algorithms by comparing the respective standard deviations $Std(y)$ of the structural deformation y_{struct}. The lower the $Std(y)$ the less the airfoil is oscillating in the flapwise direction and the less the blade is exposed to fatigue damage. $Std(y)$ is calculated by

$$Std(y) = \sqrt{\sum_{i=1}^{N} \frac{1}{N}(y_{struct(i)} - \bar{y}_{struct})^2} \tag{9}$$

where N is the total number of time steps and $\bar{y}_{struct}$ is the mean deflection of the observed time period.
During the simulation of a wind step $\bar{y}_{struct}$ is set to the deflection which is found before the wind step occurs. The optimum result of $Std(y) = 0$ m is thus achieved when y_{struct} can be held on the same level as before the wind step.

The reduction potential $R_{Std(y)}$ of a given control algorithm is computed by setting the $Std(y)$ of the non-controlled case to 100%. Thus the reduction potential of the controlled case is given in [%] and calculated by

$$R_{Std(y)} = \left(\frac{Std(y)_{uncontrolled}}{Std(y)_{controlled}} - 1 \right) \cdot 100 \tag{10}$$

9.2 Airfoil exposed to wind step

First, the airfoil is exposed to a wind step in which the axial wind velocity V_a (see Figure 42) changes from 10 m/s to 10.5 m/s at $t = 0.5$ s. A wind step can be considered as the elementary case of any wind signal and gives easy interpretable results. The gain parameters which relate the change in the measured state variable to a suitable movement of the flap can be conveniently determined.
The maximum rate of change in ϕ_{presc} was limited to $40\,^\circ/s$ in order to omit unrealistic transient forces in the EllipSys computations (see Appendix B for more information).

Control 1

As mentioned in Section 8.1 the pitot tube is assumed to measure α_{meas} at a distance $d_1 = 0.3 \cdot c$ in front of the airfoil. In Figure 53 the resulting deflection y_{struct} is shown for different gain parameter A_α. The time delay is set to $t_{delay} = 0.0s$.
Gain parameters in the range of $0.50 \leq A_\alpha \leq 0.80$ and with an interval of $\Delta A_\alpha = 0.05$

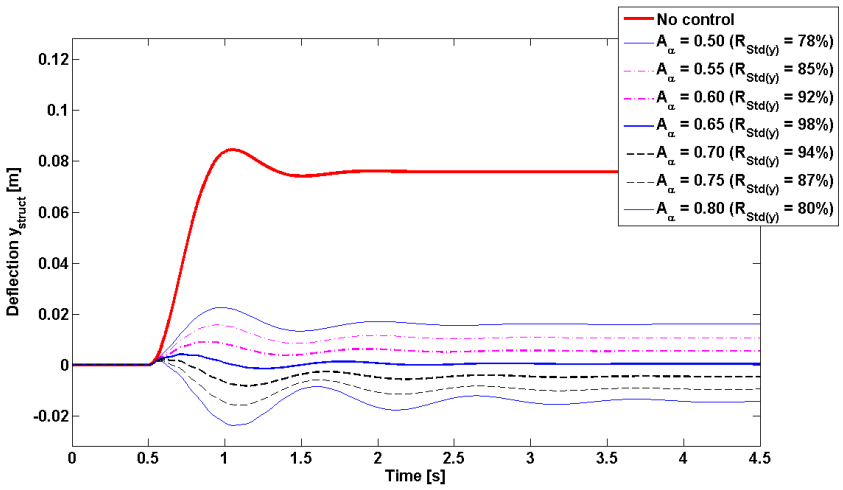

Figure 53. Structural deflection in y_{struct} during a wind step from $V_a = 10$ m/s to $V_a = 10.5$ m/s, Control 1.

are investigated. The respective reduction in the standard deviation $Std(y)$ are given in

the graph and the best reduction can be achieved with a gain of $A_\alpha = 0.65$ where the $Std(y)$ can be reduced with $R_{Std(y)} = 98\,\%$.
The simulation for $A_\alpha = 0.65$ is now observed in more detail. The corresponding flap angles β and the normal force F_y are shown in Figure 54. It can be seen how β, after some small oscillations, reaches its new equilibrium value of approximately $-3.5\,^\circ$ in order to hold F_y unchanged at a value slightly above $2800\,\mathrm{N}$.
In Figure 55 the AOA at two different distances to the LE are shown. Both graphs show

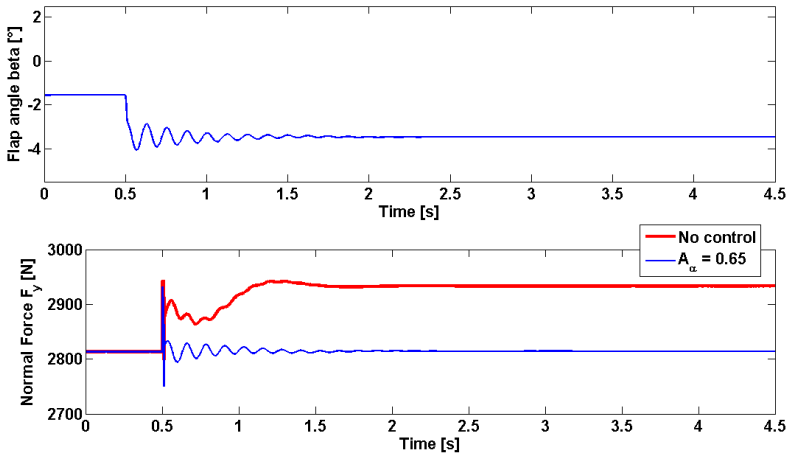

Figure 54. Flap angle β and normal force F_y during a wind step from $V_a = 10$ m/s to $V_a = 10.5$ m/s, Control 1, $A_\alpha = 0.65$

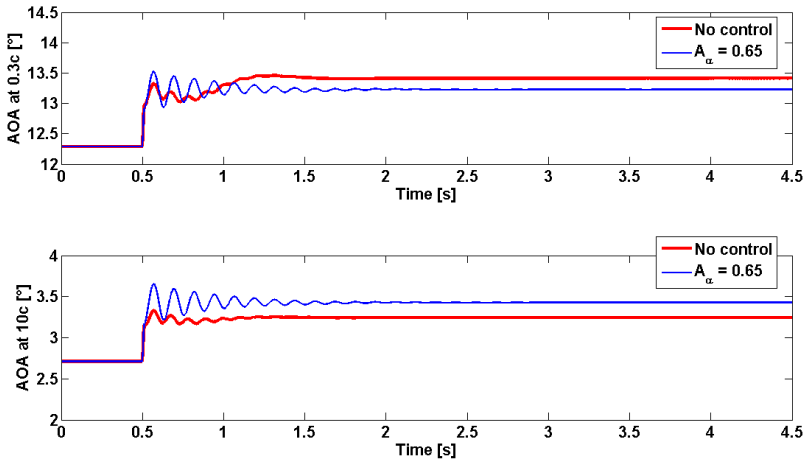

Figure 55. α_{meas} at $d_1 = 0.3 \cdot c$ (up) and α at $10 \cdot c$ (down) for the uncontrolled and controlled case, Control 1, $A_\alpha = 0.65$,

the uncontrolled and the controlled response for $A_\alpha = 0.65$ and $d_1 = 0.3 \cdot c$. In the upper graph the AOA at a distance of $0.3 \cdot c$ in front of the LE is illustrated. Below, the AOA at $10 \cdot c$ for the same simulation run is shown. It can be seen that the AOA at $0.3 \cdot c$ are quite high as the airstream in front of the airfoil is bended upwards due to self-induction. At a distance of $10 \cdot c$ the effect of self-induction is insignificant and the measured AOA corresponds to the α defined in Section 7.2.1. It is interesting to see that the AOA at $10 \cdot c$ for the controlled case is even bigger than for the uncontrolled case, although the control

aims to reduce the forces and deflections. The reason for that can be found in the location of the center of pressure which is situated *behind* the rotational center RC. After the wind velocity has increased by $\Delta V_a = 0.5$ m/s the control moves the flap upwards in order to keep the lift force constant. But the increase in AOA moves the center of pressure closer to RC which decreases the rotational moment F_θ. As a result the structural deformation θ_{struct} (see Figure 42) reduces and α increases .
However, at a distance of $0.3 \cdot c$, the AOA of the controlled case is lower than for the uncontrolled case. When the control moves the flap upwards the effect of self-induction changes, the airstream is less bended and the AOA gets smaller.
Thus, it can be seen that not only the absolute values but also the changes in AOA depend highly on the distance from the measurement position to the LE of the airfoil. This means that also the gain parameter of the control is depending on the measurement point. While for $d_1 = 0.3 \cdot c$ an optimal gain of $A_\alpha = 0.65$ is determined, the optimum gain for other measurement points will be different. A rough test showed that for $d_1 = 10 \cdot c$ the optimum gain is close to $A_\alpha = 1$.

Control 2

Control 2 is now used to alleviate the loads during the step change in wind. The gain parameter is varied between 0.006 ř/Pa $\leq A_p \leq 0.014$ ř/Pa with an interval of $\Delta A_p = 0.002$ ř/Pa. The deflection in y_{struct} is shown in Figure 56.

The best reduction in $Std(y)$ is achieved with a gain of $A_p = 0.010$ ř/Pa which brings

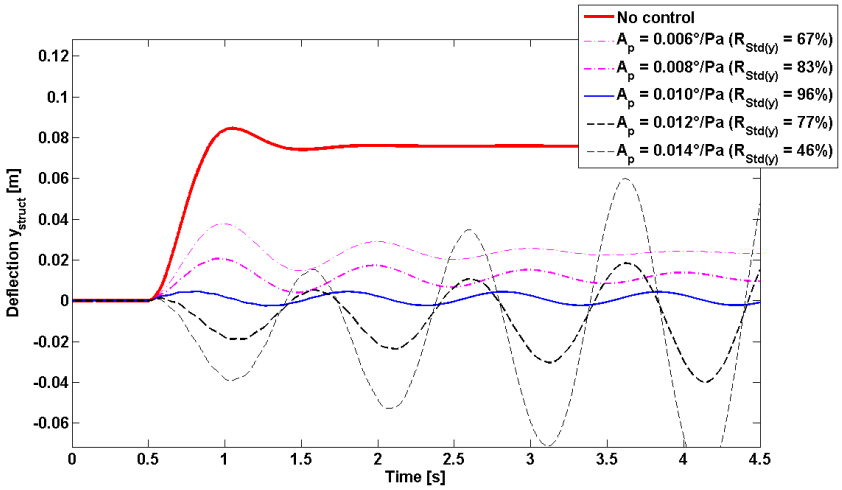

Figure 56. Structural deflection in y_{struct} during a wind step from $V_a = 10$ m/s to $V_a = 10.5$ m/s, Control 2.

the deflection y_{struct} at $V_a = 10.5$ m/s closest to the deflection at $V_a = 10$ m/s. However, the control seems to be quite sensitive and even for the optimal gain the deflection y_{struct} is not held constant. Instead a slight oscillation around the mean value is still observed. Although the best reduction of $R_{Std(y)} = 96\,\%$ is found at $A_p = 0.010$ ř/Pa the control gets already instable for $A_p = 0.012$ ř/Pa. The results for control 1 did not show these kind of sensitivities and even for gain parameters which led to lower values of $R_{Std(y)}$ the response of y_{struct} was not oscillating.
The flapping motion and the normal force for a gain of $A_p = 0.010$ ř/Pa is shown in Figure 57. The measured pressure differences Δp_{meas} for both the controlled and uncontrolled case are shown in Figure 58.

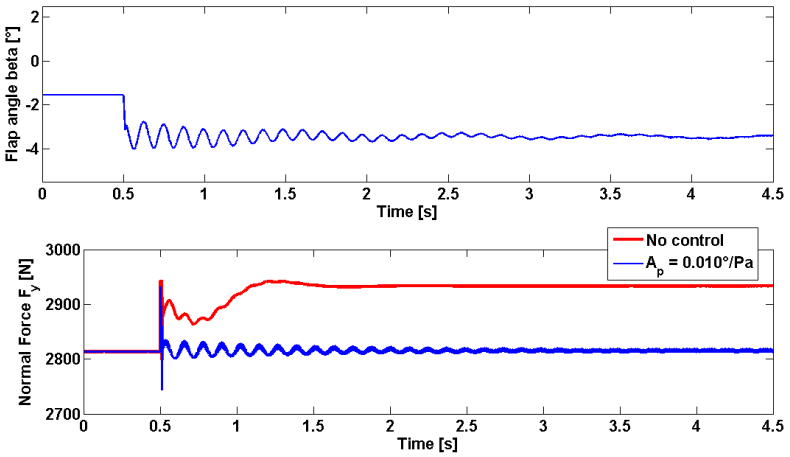

Figure 57. Flap angle β and normal force F_y during a wind step from $V_a = 10$ m/s to $V_a = 10.5$ m/s, Control 2, $A_p = 0.010$ ř/Pa

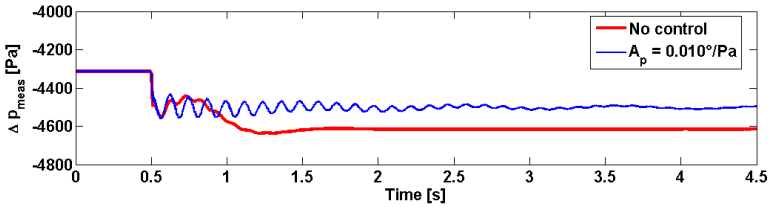

Figure 58. Δp_{meas} at $d = 0.12 \cdot c$ for the uncontrolled and controlled case, Control 2, $A_p = 0.010$ ř/Pa

9.3 Airfoil exposed to 4 s turbulent wind with $TI = 2.2$ %

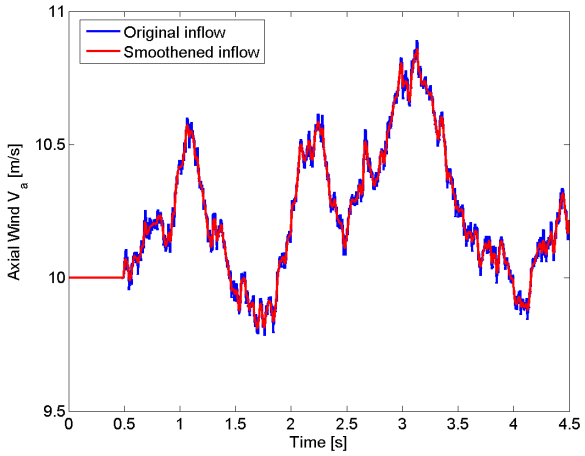

Figure 59. 4 s turbulence inflow signal with $TI = 2.2$ %

As mentioned in Appendix B the original turbulent inflow signal has to be smoothened with a Laplace smoother, using a relaxation factor of $R = 0.8$ and $m = 10\,000$ itera-

tion steps. In order to illustrate the respective smoothing effect, both the original and the smoothened signal are shown in Figure 59.

Control 1

In these computations the same gains that were used in Section 9.2 are applied. In Figure 60 the respective deflections in y_{struct} are shown, the achieved reduction in $Std(y)$ is given in the figure as well.
Again, the best result can be achieved with a gain of $A_\alpha = 0.65$ where a reduction in $Std(y)$ of 81 % is determined. The other tested gains give good results as well. Gains between $0.60 \leq A_\alpha \leq 0.70$ result all in reductions higher than 78 %. For the optimum gain of $A_\alpha = 0.65$ the flap angle β and the normal force F_y are shown in Figure 61.
It is finally observed how an introduced time delay is influencing the reduction potential of control 1. The results are shown in Figure 62 where for the optimum gain of $A_\alpha = 0.65$ time delays between $0\,\text{s} \leq t_{delay} \leq 0.1\,\text{s}$ are tested. It can be seen that until a time delay of $t_{delay} = 0.02\,\text{s}$ the reduction potential only decreases with 4%. Severe changes in the reduction potential are observed for $t_{delay} = 0.07\,\text{s}$ or more which shows that an efficient control depends strongly on the timelag inside the system.
Additional investigations were carried out checking if different gains could improve the load reductions for certain time delays. However, using $A_\alpha = 0.6$ or $A_\alpha = 0.7$ for several time delays could not further improve the performance of the control.

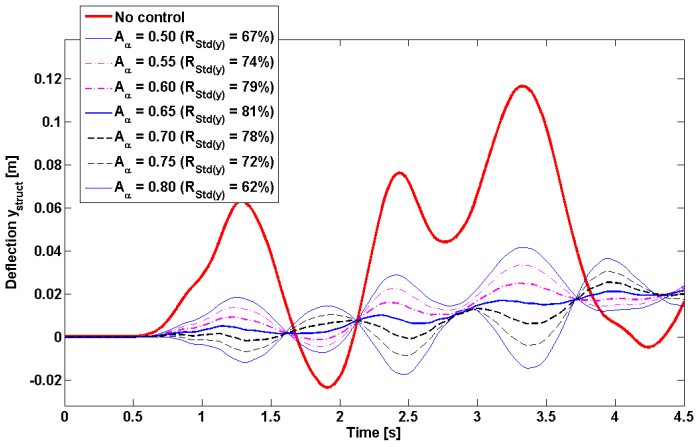

Figure 60. Structural deflection in y_{struct} during a 4 s turbulent inflow with $TI = 2.2\,\%$, Control 1.

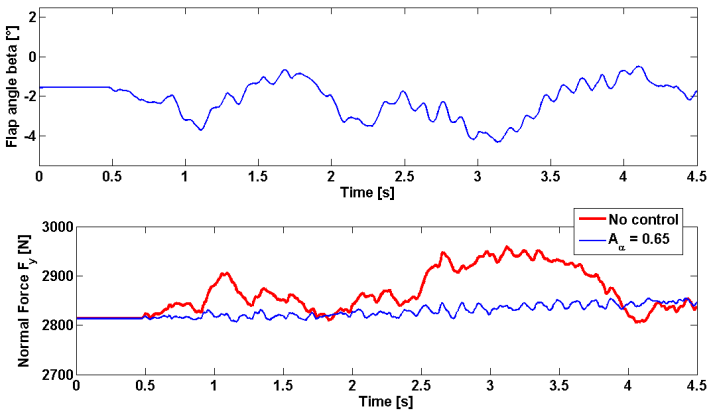

Figure 61. Flap angle β and normal force F_y during a a 4 s turbulent inflow with $TI = 2.2\,\%$, Control 1, $A_\alpha = 0.65$

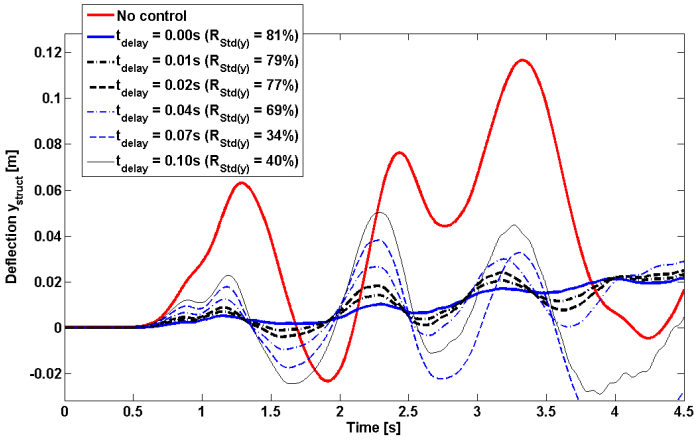

Figure 62. Structural deflection in y_{struct} for different time delays during a 4 s turbulent inflow with $TI = 2.2\,\%$, Control 1, $A_\alpha = 0.65$

Control 2

As done in Chapter 9.2 the computations are carried out for several gains between 0.006 ř/Pa $\leq A_p \leq 0.014$ ř/Pa using an interval of $\Delta A_p = 0.002$ ř/Pa. Figure 63 shows the deflections in y_{struct} where the best reduction in $Std(y)$ can be again obtained for a gain of $A_p = 0.010$ ř/Pa. The reduction potential of $R_{Std(y)} = 82\,\%$ is comparable to the one achieved with control 1. As in the simulation of the step change the system tends to become unstable for a gain of $A_p = 0.012$ ř/Pa. The flapping angle and the normal force for the simulation using $A_p = 0.010$ ř/Pa are shown in Figure 64.
The influence of a time delay inside the control loop is investigated by running simulations with the constant gain of $A_p = 0.010$ ř/Pa and varying the assumed time delay between $0.00\,\text{s} \leq t_{delay} \leq 0.10\,\text{s}$. As seen in Figure 65 the results show a big dependency on the chosen time delay. Compared to control 1 (see Figure 62) the dependency is even more severe. Already for a time delay of $t_{delay} = 0.04\,\text{s}$ the system starts to get unstable.
Additional investigations were carried out checking if different gains could improve the load reductions for certain time delays. However, using $A_p = 0.008$ ř/Pa or $A_p = 0.012$ ř/Pa for several time delays could not improve the performance of the control.

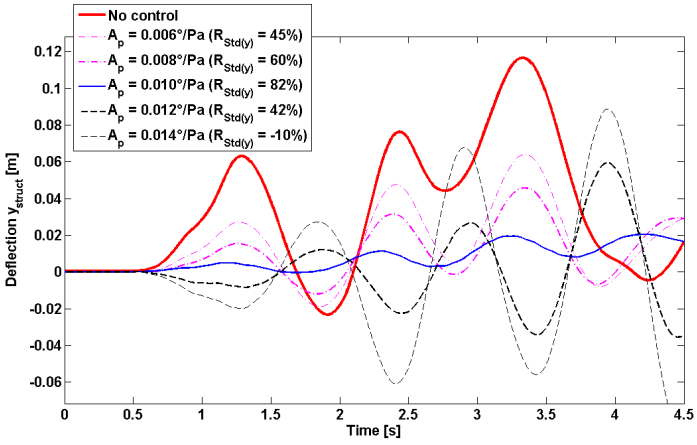

Figure 63. Structural deflection in y_{struct} during a 4 s turbulent inflow with $TI = 2.2\,\%$, Control 2.

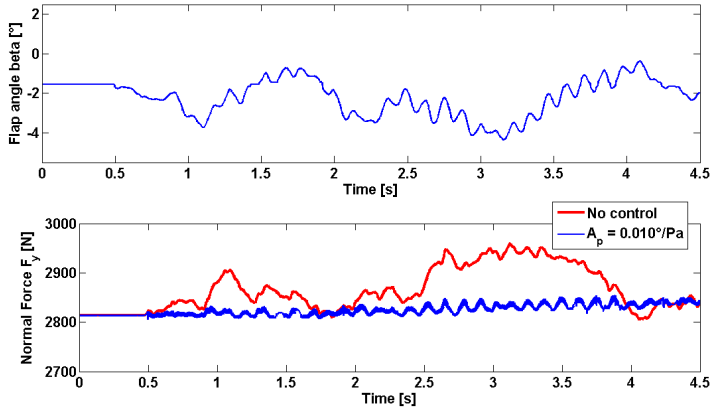

Figure 64. Flap angle β and normal force F_y during a 4 s turbulent inflow with $TI = 2.2\,\%$, Control 2, $A_p = 0.010$ ř/Pa

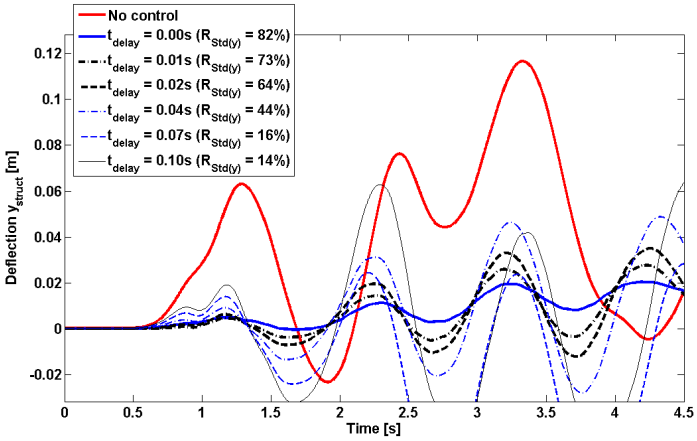

Figure 65. Structural deflection in y_{struct} for different time delays during a 4 s turbulent inflow with $TI = 2.2\,\%$, Control 2, $A_p = 0.010$ ř/Pa

9.4 Airfoil exposed to 12 s turbulent wind field with $TI = 2.4\,\%$

As it is interesting to see how the reduction potential is affected by a longer time series, the two controls and its optimum gains found in the previous section are now used to simulate a longer time series with a turbulent inflow signal of 12 seconds length. In the computations no time delay is considered.
The turbulent inflow signal is shown in Figure 66. In Figure 67 the structural deflections in y_{struct} for the two controlled cases and for the uncontrolled case are shown. Both controls promise nearly the same potential in load reduction. While the reduction by using control 1 is calculated to 68 %, the reduction by using control 2 is determined to 67 %.

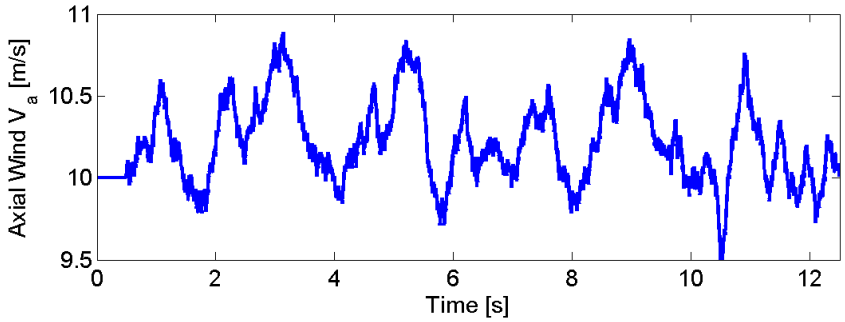

Figure 66. 12 s turbulence inflow signal with $TI = 2.4\,\%$

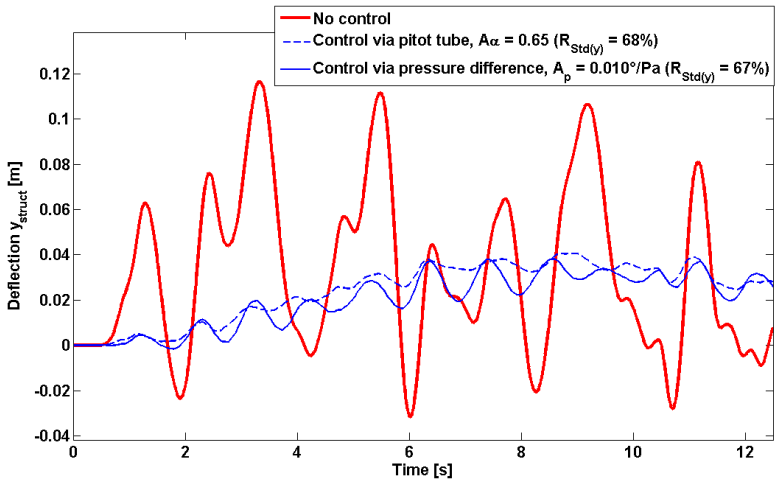

Figure 67. Structural deflection in y_{struct} during a 12 s turbulent inflow with $TI = 2.4\,\%$ using control 1 and control 2

9.5 Airfoil exposed to 12 s turbulent wind field with $TI = 7.7\,\%$

For the simulated wind fields of Sections 9.2 to 9.4 the limited flap range of $\beta_{min} = -5.3\,^\circ$ and $\beta_{max} = 2.2\,^\circ$ related to the prototype airfoil equipped with THUNDER TH-6R piezoelectric actuators was sufficient to counteract the respective lift changes entirely . Now a turbulent wind field of $TI = 7.7\%$ is used for the simulations (see Figure 68). To alleviate the big changes in the aerodynamic loads and the structural deflections, the

control algorithms demand for higher flap angles than provided by the prototype airfoil. Therefore two separate simulations are carried out.

- In the first simulation the flap deflection limits of the prototype airfoil are retained unchanged and the reduction potential in $Std(y)$ for the present prototype is calculated.
- In the second simulation the flap deflection limits are extended to $\beta_{min} = -6\,^\circ$ and $\beta_{max} = 6\,^\circ$ so the flap can reach all the flapping angles desired by the control. This simulation gives an idea of the potential of future flaps using piezoelectric actuators with a higher deflection ranges.

Figure 69 and Figure 70 show the structural deflections in y_{struct} for the two simulation runs. In Figure 69 it can be seen that the existing prototype is able to reduce the $Std(y)$ with around $54\,\%$. Although the turbulence intensity is tripled the reduction potential is still close to the results of Section 9.4. In this simulation the reduction potentials of the two controls deviate quite distinctively. Using Control 2 the reduction potential is calculated to $39\,\%$.
In Figure 70 it can be seen that an extended range of the flap deflection angle raises the reduction potential. Using control 1 the reduction potential can be brought back to the level of Section 9.4 although the turbulence intensity is now tripled and changes in the axial wind speed of up to $\Delta V_a = 4\,$m/s occur. As in the previous simulation the result for control 2 is lagging behind. The reduction potential is calculated to $57\,\%$.

9.6 Comment on the results

In the course of this work not all parameters affecting the reduction potential could be investigated in detail and several choices had to be made in advance.
All illustrated investigations were carried out by keeping the measurement positions constant at $d_1 = 0.3 \cdot c$ and $d_2 = 0.12 \cdot c$ and it might be interesting to see if other positions could suit even better as input to the control algorithms. Predestinated measurement points are those where a change in lift is related to a pronounced change in the measured value. Additionally the present control algorithms should work best if the change of the measured quantity is linearly correlated to the respective change in lift.
The optimum gain parameter were determined by testing different gains with a certain interval of ΔA_{alpha} or ΔA_p. Therefore it can not be insisted that the absolute optimal load reduction values of the several test cases could be found and a thorough investigation of the gain parameters should use finer gain tuning intervalls. Especially the somewhat lower performance of control 2 during the time delay investigations and during the highly turbulent inflow with $TI = 7.7\,\%$ should not be interpreted as a general demerit of this control. A more detailed investigation of the gain parameters could lead to load reductions which comparable to those of control 1, just like in the other tested cases.
The chosen time window of $\tau = 6\,$s is also influencing the computed load reduction potential and thorough investigations should also check how variations in τ affect the efficiency of the controls.

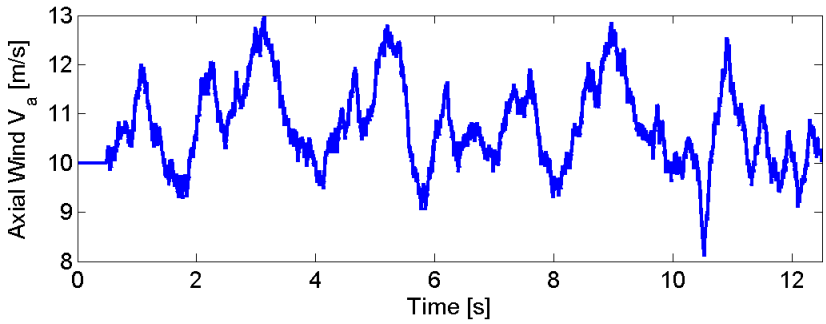

Figure 68. 12 s turbulence inflow signal with $TI = 7.7\,\%$

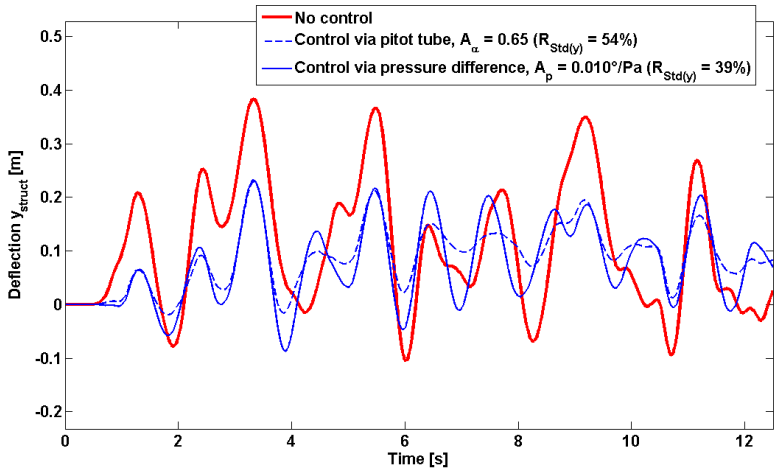

Figure 69. Structural deflection in y_{struct} during a 12 s turbulent inflow with $TI = 7.7\,\%$ using the flap deflection limits of the prototype airfoil

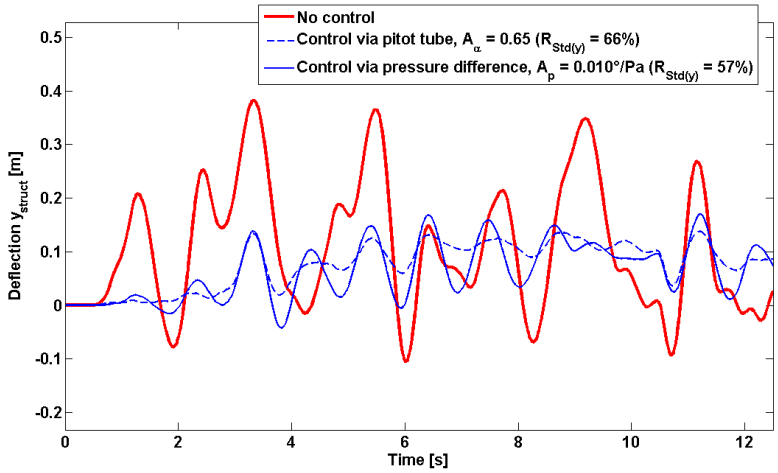

Figure 70. Structural deflection in y_{struct} during a 12 s turbulent inflow with $TI = 7.7\,\%$ using extended flap deflection limits of $\beta_{min} = -6\,^\circ$ and $\beta_{max} = 6\,^\circ$

10 Conclusion and Future Work

10.1 Conclusion

In this work a 3 DOF structural model and two different control algorithms have been implemented in the EllipSys2D Navier-Stokes solver in order to investigate the load reduction potential of the Risø B1-18 airfoil using THUNDER TH-6R piezoelectric actuators as trailing edge flaps. This airfoil was already used in a previous wind tunnel test in order to investigate the load alleviation potential of trailing edge flaps.

A detailed model of a 2 D airfoil section, similar to the prototype airfoil, was generated. The deflection shape of the piezoelectric flaps was derived out of voltage depending geometrical measures given in the data sheet of the actuator.

The generated airfoil section was used to compare simulation results with wind tunnel measurements.
Comparisons for a fixed AOA and a fixed flap angle indicated that the modeled flap had to be rotated with $-8\,^\circ$ around its root point to fit with the measured polars. This rotation was assumed to be caused by mounting inaccuracies at the prototype and by a flap deformation due to the aerodynamic forces during the wind tunnel test. However, for a fixed flap deflection angle of $\beta = -2\,^\circ$ the measured lift curve showed a bellied characteristic between $\alpha = -4\,^\circ$ and $\alpha = 6\,^\circ$ and thus somewhat higher lift values than computed.
The model with the corrected flap position was then used to understand and check the wind tunnel measurements during harmonic pitch and/or flap motions.
For a harmonic pitch motion of $f = 1.62\,Hz$ and a fixed flap angle of $\beta = 0\,^\circ$ the lift and drag loops for four different mean angles of attack were compared. While the absolute values and the general shape of the lift loops corresponded very well, some deviations in the loop direction occurred. The measured lift loops all turned clockwise. The simulated lift loops for $\alpha_m = -1.55\,^\circ$, $\alpha_m = 4.3\,^\circ$ and $\alpha_m = 7.65\,^\circ$ turned counter-clockwise. Only the computed lift loop for $\alpha_m = 11.5\,^\circ$ turned clockwise which is due to dynamic stall effects. The mean values of the computed and measured drag loops were quite similar, however, the computed drag loop shapes were more open. Additional potential flow simulations confirmed the CFD computations in both the absolute values and the loop directions of lift and drag.
Then, comparisons for a fixed AOA and a harmonically moving flap with $f = 1.56\,\mathrm{Hz}$ and $f = 10\,\mathrm{Hz}$ were carried out. The computations could confirm the measured lift loop directions. All lift loops turned counter-clockwise. The simulated drag loops were more open. In both simulations and measurements the increase of the flapping frequency from $f = 1.56\,\mathrm{Hz}$ to $f = 10\,\mathrm{Hz}$ decreased the flap efficiency $\mathrm{d}C_l/\mathrm{d}\beta$ with approximately 40 %. However, the computed flap efficiencies were generally 60 % higher than in the respective measurements. The deviations could be assigned to the belly shaped lift curves found e.g. in the static lift curve for $\beta = -2\,^\circ$.
Finally, the measurements for a phase shifted pitching and flapping motion of $f = 1.62\,\mathrm{Hz}$ were compared with simulations. The optimum phase shift of $\kappa = 30\,^\circ$ determined in the measurements could not be confirmed as the simulations showed an optimum value of approximately $\kappa = 10\,^\circ$. The simulated lift and drag loops for $\kappa = 10\,^\circ$ and for $\kappa = 30\,^\circ$ turned counter-clockwise while the respective measured loops turned clockwise. Additional potential flow simulations confirmed the loop direction of the CFD computations.
In the comparison between simulation and measurements several deviations in the results were detected. The deviations in the static lift curves for a fixed AOA and a fixed flap angle could partly stem from transition effects. The deviations in the dynamic measurements could additionally stem from the difficulty to apply wind tunnel corrections on the

measurements of a dynamic test set-up.

Comprehensive steady state calculations have been carried out to get broad information about some key properties of the prototype airfoil. This was done for both the airfoil with the *corrected* flap position and the airfoil with the unchanged *exactly mounted* flap. Lift coefficients for several (fixed) AOA and (fixed) flap angles were computed in order to investigate the static lift change potential of the airfoils. The maximum flap efficiencies were found at $\alpha = -4\,^\circ$. While the exactly mounted flap reached a maximum of $\mathrm{d}C_l/\mathrm{d}\beta = 2.2\,\mathrm{rad}^{-1}$ the corrected flap reached a maximum of $\mathrm{d}C_l/\mathrm{d}\beta = 2.75\,\mathrm{rad}^{-1}$. The flap efficiencies decrease gradually with an increasing AOA. For high AOA with separated flow regions the flap efficiencies drop distinctively.
It was also found that a flap with a smoothened surface did not reduce the drag and thus improve the obtained gliding numbers significantly.

It was explained how the incompressible Reynolds averaged solver EllipSys2D was coupled with a 3 DOF structural model. The simulation of a fluctuating inflow was accomplished by rotating the mesh which thus changes the AOA in correspondence to the change of the incoming wind. The new aero-elastic model was successfully compared to a corresponding model which calculates the aeodynamic forces with a potential flow solver developed by Gaunaa [7]. The model was extended to an aero-servo-elastic model by implementing two different control algorithms to actuate the flap. Control 1 was using the measured AOA at a distance of $d_1 = 0.3 \cdot c$ in front of the LE as input, Control 2 was using the pressure difference between the pressure and suction side at a chord position of $d_2 = 0.12 \cdot c$ as input. In order to keep the aero-servo-elastic simulations close to reality, limits on the flap actuation speed and on the maximum flap deflection angle were implemented corresponding to the properties of the THUNDER TH-6R actuators. A certain time delay for the signal transmission inside the control loop can be set.

Several simulations with different fluctuating inflows were carried out in order to investigate the load reduction potential of the piezoelectric flap and the respective control. The standard deviation $Std(y)$ of the structural deflection normal to the rotor plane was used to compare the results. The achieved reduction in $Std(y)$ (compared to the uncontrolled case) was denoted with $R_{Std(y)}$ and thus represented a measure for the load reduction potential.
The system was first exposed to a wind step from 10 m/s to 10.5 m/s. Control 1 could achieve a reduction of $R_{Std(y)} = 98\,\%$ using a gain of $A_\alpha = 0.65$ while control 2 could achieve a reduction of $R_{Std(y)} = 96\,\%$ using a gain of $A_p = 0.010$ ř/Pa. No time delay was considered.
For a turbulent inflow of 4 s and a turbulence intensity of $TI = 2.2\,\%$ the same optimum gains as for the wind step could be determined. Control 1 could alleviate the oscillations in the normal direction with $R_{Std(y)} = 81\,\%$, control 2 could even reach $R_{Std(y)} = 82\,\%$. Both controls seem to be adequately capable for load reduction.
For the same turbulent wind field it was investigated how several time delays t_{delay} influence the results. It was found that for control 1 a time delay of up to $t_{delay} = 0.04\,\mathrm{s}$ still provided acceptable results with a $R_{Std(y)} \geq 69\,\%$. Control 2 seemed to be more sensitive due to time delays. For $t_{delay} = 0.04\,\mathrm{s}$ control 2 was already starting to be unstable, for $t_{delay} = 0.02\,\mathrm{s}$ the reduction was calculated with $R_{Std(y)} = 64\,\%$. However, it should not be concluded that control 2 gives generally worse results. The increased sensitivity could also indicate that the optimum gain parameter should be adjusted with more caution. In the present work the optimum gain was found by using an interval of $\Delta A_p = 0.002\,^\circ/Pa$.
The structural response for a longer turbulent wind field of 12 s and a $TI = 2.4\,\%$ was also investigated, using the optimum gain parameters of the previous section. No time delays were considered. The two controls achieve again corresponding results. Control 1

achieved $R_{Std(y)} = 68\,\%$, control 2 achieved $R_{Std(y)} = 67\,\%$.
For a 12 s turbulent wind field with $TI = 7.7\,\%$ and using again the optimum gain parameters of the previous sections, control 1 could reach a reduction in $Std(y)$ of 54 % and control 2 could reach a reduction of 39 %. As this highly turbulent wind signal demanded for higher flap angles than available with the present prototype airfoil, a last simulation was carried out where the flap angle limits were altered to $-6\,^\circ \leq \beta \leq 6\,^\circ$. With the extented flap range control 1 achieved $R_{Std(y)} = 66\,\%$ which is again very close to the results of the previous simulation using the reduced turbulence of $TI = 2.4\,\%$. Control 2 achieved $R_{Std(y)} = 57\,\%$. For the wind field with $TI = 7.7\,\%$ control 1 could reach better results. A reason could be that the sensitive control 2 requires a finer gain tuning than used in this work.
However, the results presented in the last chapter show that both controls can achieve substantial load reductions using a piezoelectric actuator as a deformable trailing edge flap.

10.2 Future Work

As mentioned in Section 9.6 not all dependencies on the load reduction potential could be investigated thoroughly in the scope of this work. Therefore it might be interesting to investigate in more detail how changes in the measurement positions d_1 and d_2 would influence the performance of the control. The gain parameters could be tuned and investigated more carefully. Especially for control 2 it is believed that a finer gain tuning can improve some of the achieved results and thus reach in all tested cases the same level of load redution as control 1. Additionally, the influence of the chosen time window τ could be investigated.
The developed aero-servo-elastic could be used to investigate airfoils with other DTEG and the performances can be compared to those of the piezoelectric flaps.
As the present work confirmed the big load reduction potential of piezoelectric trailing edge flaps future work should aim to implement a respective aero-servo-elastic model in more sophisticated 2 D and 3 D CFD simulations.

Acknowledgements

I would like to thank my supervisors Frederik Zahle, Jeppe Johansen and Niels N. Sørensen for their very good guidance. I very much appreciate their devoted and immediate help whenever I needed it.
Special thanks to Peter Bjørn Andersen for his remarkable support in so many issues. I would also like to thank Christian Bak for his help concerning the wind tunnel measurements. Thanks a lot to Mac Gaunaa and Thomas Buhl for their continuous support throughout the work.
Generally, I am very pleased that I could meet so many nice, friendly and helpful people in the Wind Energy Department of Risø. Thank you all!

I would like to thank my brother Alexander and my parents Richard and Eveline for their important support, although they live some distance away. Special thanks to my fellow students and friends Leonardo and Kostas for their support during the past two student years. Finally, I would like to thank all my friends for those many nice and unforgettable moments we had during my studies here in Denmark.

References

[1] T. Larsen, H. Madsen, and K. Thomsen. Active Load Reduction using Individual Pitch, Based on Local Blade Flow Measurements. *Proc. The Science of Making Torque from Wind*, 2004.

[2] T. K. Barlas and G. A. M. van Kuik. State of the Art and Prospectives of Smart Rotor Control for Wind Turbines. *Proc. The Science of Making Torque from Wind*, 2007.

[3] D. T. Y. Nakafuji, C. van Dam, R. Smith, and S. Collins. Active Load Control for Airfoils using Microtabs. *Journal of Solar Energy Engineering, Vol. 123*, 2001.

[4] R. Chow and C. P. van Dam. Computational investigations of deploying load control microtabs on a wind turbine airfoil. *45th AIAA/ASME*, 2007.

[5] T. Buhl, M. Gaunaa, and C. Bak. Potential Load Reduction Using Airfoils with Variable Trailing Edge Geometry. *Journal of Solar Energy Engineering, Vol. 127*, 2005.

[6] Peter B. Andersen. Load Allevation on Wind Turbine Blades using Variable Airfoil Geometry (2D and 3D study). *Technical University of Denmark*, 2005.

[7] M. Gaunaa. Unsteady 2D Potential-Flow Forces on a Thin Variable Geometry Airfoil undergoing Arbitrary Motion. *Risø-R-1478,Denmark*, 2004.

[8] N. Troldborg. Computational Study of the Risø-B1-18 Airfoil Equipped with Actively Controlled Trailing Edge Flap. *Technical University of Danmark*, 2004.

[9] P. B. Andersen. A Dynamic Stall Model for Airfoils with Deformable Trailing Edges. *Proc. The Science of Making Torque from Wind*, 2007.

[10] J. A Michelsen. Basis3D - a Platform for Development of Multiblock PDE Solvers. *Tech. Report AFM 92-05, Technical University of Denmark*, 1992.

[11] J. A Michelsen. Block Structured Multigrid Solution of 2D and 3D Elliptic PDEs. *Tech. Report AFM 94-06, Technical University of Denmark*, 1994.

[12] N. N. Sørensen. General Purpose Flow Solver Applied to Flow over Hills. *Risø National Laboratory*, 1995.

[13] J. H. Ferziger and M. Peric. Numerische Strömungsmechanik. *Springer Verlag Berlin Heidelberg*, 2008.

[14] F. R. Menter. Two-Equation Eddy-Viscosity Turbulence Model for Engineering Applications. *AIAA Journal, Vol. 32, No. 8*, 1994.

[15] F. R. Menter. Performance of Popular Turbulence Models for Attached and Separated Adverse Pressure Gradient Flows. *AIAA Journal; 30: 2066-2072*, 1992.

[16] N. N. Sørensen. HypGrid2D a 2-D Mesh Generator. *Risø-R-1035(EN), Risø National Laboratory*, 1998.

[17] C. Bak, M. Gaunaa, P. B. Andersen, T. Buhl, P. Hansen, K. Clemmensen, and R Moeller. Wind Tunnel Test on Wind Turbine Airfoil with Adaptive Trailing Edge Geometry. *AIAA Aerospace Sciences Meeting and Exhibition*, 2007.

[18] M. Gaunaa, P Fuglsang, C. Bak, and I Antoniou. Open-Jet Wind Tunnel Validation Using A NACA 0012 Airfoil. *Risø National Laboratory*, 2005.

[19] P. B. Andersen and M. Gaunaa. Load Reduction using Pressure Difference on Airfoil for Control of Trailing Edge Flaps. *Risø National Laboratory*, (to come).

A Non-dimensionalized calculation in EllipSys2D

Throughout this work the calculations in EllipSys2D were accomplished by using non-dimensionalized quantities, while the structural model was using dimensionalized quantities. This means that several transformations had to be carried out at the interface of the two models. Non-dimensionalized quantities are assigned with *.

In EllipSys2D the velocity is non-dimensionalized with the free stream velocity U_∞ which means that $U^*_\infty = 1$. The density is constant and set to $\rho^* = 1$. The lengthscale is non-dimensionalized with the chord length and results in a non-dimensionalized chord length of $c^* = 1$. The time is non-dimensionalized with $t^* = t \cdot U_\infty / c$, which means that a flow with velocity U_∞ needs $t^* = 1$ to travel one chordlength.

This leads to the following transformations carried out in the program:

- Non-dimensionalization of the structural motion:

$$\begin{aligned} x^*_{struct} &= x_{struct}/c \\ y^*_{struct} &= y_{struct}/c \end{aligned}$$

- Dimensionalization of the aerodynamic loads:

$$\begin{aligned} F_x &= F^*_x \cdot f_{dim,m} = F^*_x \cdot \rho U^2_\infty c \\ F_y &= F^*_y \cdot f_{dim,m} = F^*_x \cdot \rho U^2_\infty c \\ F_\theta &= F^*_\theta \cdot f_{dim,m} = F^*_\theta \cdot \rho U^2_\infty c^2 \end{aligned}$$

- As illustrated in Figure 45 the time step size of the computations is defined in EllipSys2D. The structural model is adopting this time stepping but uses dimensionalized quantities. To correlate the time stepping of the two models, the time step size in the structural model has to be:

$$\Delta t = \Delta t^* \cdot c / U_\infty \tag{A.11}$$

- To keep the non-dimensionalized free stream velocity at $U^*_\infty = 1$, V_{rot} and V_a have to be transformed in the following way:

$$\begin{aligned} V^*_{rot} &= \cos\left(\arctan\left(V_a/V_{rot}\right)\right) \\ V^*_a &= \sin\left(\arctan\left(V_a/V_{rot}\right)\right) \end{aligned}$$

  which leads to:

$$U^*_\infty = \sqrt{{V^*_{rot}}^2 + {V^*_a}^2} \stackrel{!}{=} 1$$

B Omitting transient forces during a fluctuating inflow

It turned out that quick changes in the incoming wind field evoke high transient forces in the CFD computations which lead to unrealistic aerodynamic force characteristics. Thus quick changes in the wind velocities V_a have to be smoothened. While the smoothening should omit the transient forces the general characteristics of the incoming wind should not be altered. Adequate results can be obtained with the following methods:

- To simulate an immediate step change in the velocity V_a the maximum rate of change in ϕ_{presc} should be limited to 40 ř/s.

- For a turbulent inflow signal the best results can be obtained by using the Laplace smoother

  $for\ i = 1 : m$
  $V_a(n) = V_a(n) \cdot R + (1 - R) \cdot (0.25 \cdot V_a(n-1) + 0.5 \cdot V_a(n) + 0.25 \cdot V_a(n+1))$
  end

  where R is the relaxation factor and n is the time step number. The formula has to be applied for several iteration steps m. For a non-dimensionalized time step size of $t^* = 0.01$ the turbulent inflow signals used in Chapter 9 can be adequately smoothened by using a relaxation factor of $R = 0.8$ and an iteration number of $m = 10\,000$.

C Input file and Computational Time

An input file for a typical simulation run of chapter 9 is shown below. The whole simulation covers $N = 45\,000$ non-dimensional time steps with a non-dimensional time step of $\Delta t^* = 0.01$. For a free stream velocity of $U_\infty = 60$ m/s this corresponds to a total time of $t = 7.5$ s with $\Delta t = 0.00017$ s. The structural model starts at $t = 0.5$ s in order to allow the flowfield to settle before the model starts. To get comparable starting conditions the control is started at $t = 3.0$ s giving the structural model 2.5 seconds to reach its equilibrium. The time series of the axial wind speed V_a is defined via ϕ_{presc} and stored in the *presc.inflow* file. The data is stored in a way that the wind step or the turbulent wind signal starts at $t = 3.5$ s. In the results of chapter 9 the first three seconds of the simulations are cut out in order to focus on the part relevant to determine the load reduction.

The simulations were carried out on the Risø Central Computer Facility, "Mary", which consists of 240 computation nodes, each of them equipped with a 3.2 GHz central processing unit, 1 MB cache and 2 GB random access memory. The nodes are connected by a Gigabit Ethernet. The multiblock feature of EllipSys was used for parallel computations. The computations were distributed to eight separate nodes by dividing the original mesh of $256(\xi) \cdot 128(\eta)$ cells into eight blocks of $64(\xi) \cdot 64(\eta)$ cells. For a non-dimensionalized time step of $\Delta t^* = 0.01$, six inner interation steps, six subiteration steps and a pressure correction convergence criterium of $\Delta p^* = 0.1$, the computations for a typical simulation run with 45 000 time steps (see input file below) took approximately three hours time.

```
# gridlevel to start on
    grid_level 1
# number of outer iterations
    mstep 45000 0 0
#    mstep 3000 310 100
# number of inner iterations
    mstepp 6
# number of subiterations
    subiterations 6 6
# convergens criterium
    reslim 1.d-8 1.d-4 1.d-4
# convergens criterium for pressure correction
    reslimp 1.d-1
# difference scheme
    diff_scheme quick suds uds
# pressure correction method
    pres_corr piso
#    pres_corr simple
# start from scratch
#    restart    true
# steady state calculation
    transient  true 1.d-2
# ----------------------------------------------------------------------
#        output parameters
# ----------------------------------------------------------------------
# number of iterations between writing out graph file (.force)
    output    true
    nrgraphout 10
# number of iterations between writing out restart file
    nrrestart  5000
    nrflush 50
    average 50000000
# ----------------------------------------------------------------------
#        relaxation parameters
# ----------------------------------------------------------------------
    relaxu .8d0
    relaxp .2d0  0.8d0
# ----------------------------------------------------------------------
#        fluid parameters
# ----------------------------------------------------------------------
    density   1.d0
#  for Reynolds 1.66d6 (velo=40m/s, chord=0.66)
#    viscosity 6.25d-7
#  for Reynolds 4.2d6 (velo=60m/s, chord=1)
    viscosity 2.38d-7
# ----------------------------------------------------------------------
#        inlet values
# ----------------------------------------------------------------------
    uinlet   1.0
    vinlet   0.0
# ----------------------------------------------------------------------
#        farfield values
# ----------------------------------------------------------------------
    ufarfield   1.0
    vfarfield   0.0
# ----------------------------------------------------------------------
#       k-omega model
# ----------------------------------------------------------------------
# turbulent calculation
    turbulence   komega
    ko_version sst
#    transition  drela
# relaxation for turbulence equations
    relaxturb  7.0d-1
```

```
# inlet parameters
    te_inlet        1.d-2
    omega_inlet     1.d7
# farfield parameters
    te_farfield    1.d-2
    omega_farfield 1.d7
# ------------------------------------------------------------------
#     moving mesh
# ------------------------------------------------------------------
    moving_coord mesh
    rot_center       0.3d0 0.d0
# ------------------------------------------------------------------
#     fluctuating inflow
# ------------------------------------------------------------------
    read_in_presc.inflow_file   .true.
# ------------------------------------------------------------------
#   structural model
# ------------------------------------------------------------------
    struct_start_time  0.5d0
# x, y, phi
    init_cond    0.d0 1.8d0 0.041d0
    dof_in_x_y_phi .false. .true. .true.
# rotational speed if wind_tunnel=.false.
    velocity     60d0
# geometrical pitch
    phi_geom  5.d0
# ------------------------------------------------------------------
#   control algorithm
# ------------------------------------------------------------------
# general control input
    use_control .true.
    contr_start_time 3.0d0
    beta_org     2.2d0
    beta_ext    -5.3d0
    beta_m      -1.55d0
    time_window  6.d0
    time_lag     0.d0
# input for control 1
    alpha_gain 0.65d0
    extract-point -0.3d0 0.d0
# input for control 2
    use_pressure_difference .false.
    pressure_difference_gain 0.010d0
    tap_pos 0.12d0
    tap_tolerance 0.001d0
# ------------------------------------------------------------------
```

Risø DTU is the National Laboratory for Sustainable Energy. Our research focuses on development of energy technologies and systems with minimal effect on climate, and contributes to innovation, education and policy. Risø DTU has large experimental facilities and interdisciplinary research environments, and includes the national centre for nuclear technologies.

Risø DTU
National Laboratory for Sustainable Energy
Technical University of Denmark

Frederiksborgvej 399
PO Box 49
DK-4000 Roskilde
Denmark
Phone +45 4677 4677
Fax +45 4677 5688

www.risoe.dtu.dk